POWERING PROGRESS THROUGH
SCIENCE AND TECHNOLOGY

EPRI

BWRVIP BWR Vessel & Internals Project 2000-215

July 26, 2000

Proj - 704

Document Control Desk
U. S. Nuclear Regulatory Commission
11555 Rockville Pike
Rockville, MD 20852

Attention: C. E. Carpenter

Subject: Project 704 - Transmittal of "BWR Vessel and Internals Project, Evaluation of Crack Growth in BWR Stainless Steel RPV Internals (BWRVIP-14NP)," EPRI Report TR-105873NP, July 2000.

Reference: Letter from C. Terry to C. E. Carpenter, June 26, 1998: Transmittal of "BWR Vessel and Internals Project, Evaluation of Crack Growth in BWR Stainless Steel RPV Internals (BWRVIP-14)," EPRI Report TR-105873, March 1996.

Enclosed are two (2) copies of the subject report "BWR Vessel and Internals Project, Shroud Support and Vessel Bracket Repair Design Criteria (BWRVIP-52NP)," EPRI Report TR-108720NP, May 2000. This is the non-proprietary version of the document submitted to the NRC by the letter referenced above.

If you have any questions on this subject please call Steve Lewis of Entergy, BWRVIP Assessment Committee Chairman, at (601) 368-5444.

Sincerely,

Carl Terry
Niagara Mohawk Power Company
Chairman, BWR Vessel and Internals Project

Enclosure

D058

EPRI

BWR Vessel and Internals Project Evaluation of Crack Growth in BWR Stainless Steel RPV Internals (BWRVIP-14NP)

NON-PROPRIETARY INFORMATION

NOTICE: This report contains the non-proprietary information that is included in the proprietary version of this report. The proprietary version of this report contains proprietary information that is the intellectual property of BWRVIP utility members and EPRI. Accordingly, the proprietary report is available only under license from EPRI and may not be reproduced or disclosed, wholly or in part, by any Licensee to any other person or organization.

REPORT SUMMARY

BWRVIP Vessel and Internals Project

Evaluation of Crack Growth in BWR Stainless Steel RPV Internals (BWRVIP-14NP)

The Boiling Water Reactor Vessel and Internals Project (BWRVIP), formed in June 1994, is an association of utilities focused exclusively on BWR vessel and internals issues. This report, fourteenth in a series of several, provides a methodology for assessment of crack growth in BWR stainless steel shrouds and other stainless steel internals components.

INTEREST CATEGORIES

Piping, reactor, vessel & internals
Licensing and safety assessment

KEYWORDS

Boiling water reactor
Core shroud
Crack growth rate
Residual stresses
Stress corrosion cracking
Vessel and internals

BACKGROUND Events in 1993 and 1994 confirmed that intergranular stress corrosion cracking (IGSCC) is a significant issue for BWR internals. US BWR executives formed the BWRVIP in June, 1994, to address integrity issues arising from service-related degradation of these key components, beginning with core shroud cracking.

One major issue facing the nuclear industry is the issue of core shroud reinspection and premature repair which can impose an unnecessary economic hardship on utilities. The reinspection interval is dependent upon the extent of cracking observed during the baseline examination and prediction of the crack growth as a function of future operating time. The current methodology for determining reinspection interval is based on characterizing all observed cracks as through-wall cracks and propagating these cracks around the circumference of the shroud assuming a conservative crack growth rate of 5 x 10-5 in/hr. It is believed that a more realistic reinspection interval can be established if a crack growth model is developed which can account for both the through-thickness and the circumferential growth of the cracks.

OBJECTIVE To formalize the methodology for determination of through-thickness stainless steel crack growth rates based on empirical data that account for parameters that are known to affect crack propagation.

APPROACH The project team compiled an extensive database that included both experimental data points and in-plant crack arrest verification system (CAVS) data. The team used the database to derive an empirical, best-fit, stress intensity factor (K) dependent, crack growth correlation which also accounts for environmental conditions such as conductivity, electrochemical potential (ECP) and temperature. The team then developed a conservative 95th percentile model for through-thickness crack growth which was a factor of 10.3 greater than the best fit correlation. The model was then tested against field data and found to provide a realistic bound to the data.

RESULTS Based on extensive crack growth data collected from several sources, an empirical through-wall crack growth correlation has been developed for use in the evaluation of BWR stainless steel internals. The correlation is applicable for weld-sensitized components and is bounding for non-sensitized components. The

report provides analysis and measurements of residual stresses in core shroud welds and discusses fracture mechanics methods employed in determining stress intensity factors. The report provides three alternative methods for crack growth evaluation. Using conservative ECP and conductivity estimates, results confirm ASME Section XI safety margins are not compromised by extended operation of core shrouds with IGSCC indications.

EPRI PERSPECTIVE The empirical correlation developed in this study can be used to conservatively predict the through-thickness crack growth rate for austenitic stainless steels at various ECPs corresponding to different locations in the core shroud. The model is applicable over the specific ranges of stress intensity, water conductivity and ECP for which the correlation was developed. Application of this methodology provides assurance that BWRs with IGSCC indications can continue to operate safely while reducing utility costs by supporting reasonable intervals for reinspection and avoiding the costs of unnecessary repair.

PROJECT
RP301
EPRI Project Manager: R. Pathania
Nuclear Power Group
Contractor: Structural Integrity Associates

For ordering information about this report, call the EPRI Program Manager at (415) 855-2340.

For membership information, call (415) 855-2514.

BWR Vessel and Internals Project

Evaluation of Crack Growth in BWR Stainless Steel RPV Internals (BWRVIP-14NP)

TR-105873NP
Research Project B 301

Final Report, July 2000

Prepared by:

STRUCTURAL INTEGRITY ASSOCIATES
3315 Almaden Expressway, Suite 24
San Jose, CA 95118-1557

In Collaboration with

General Elelctric Nuclear Energy
Modeling and Computing Services
Entergy Operations, Inc.
EPRI Repair and Replacement Center
University of California, Berkley
Sandia National Laboratories
Dominion Engineering, Inc.

Prepared for

BOILING WATER REACTOR VESSEL & INTERNALS PROJECT and **EPRI**

3412 Hillview Ave.

Palo Alto, California 94304

DISCLAIMER OF WARRANTIES AND LIMITATION OF LIABILITIES

This report was prepared by the organization(s) named below as an account of work sponsored or cosponsored by the BWR Vessel and Internals Project (BWRVIP) and the Electric Power Research Institute, Inc. (EPRI). Neither BWRVIP, EPRI, any member of EPRI, any cosponsor, the organization(s) named below, nor any person acting on behalf of any of them:

(a) makes any warranty or representation whatsoever, express or implied, (i) with respect to the use of any information, apparatus, method, process or similar item disclosed in this report, including mechantability and fitness for a particular purpose, or (ii) that such use does not infringe on or interfere with privately owned rights, including any party's intellectual property, or (iii) that this report is suitable to any particular user's circumstance, or

(b) assumes any responsibility for any damages or other liability whatsoever (including any consequential damages, even if BWRVIP, EPRI or any EPRI representative has been advised of the possibility of such damages) resulting from your selection or use of this report or any information, apparatus, method, process or similar item disclosed in this report.

Organization(s) that prepared this report:

STRUCTURAL INTEGRITY ASSOCIATES

in Collaboration with

General Electric Nuclear Energy
Modeling and Computing Services
Entergy Operations, Inc.
EPRI Repair and Replacement Center
University of California, Berkeley
Sandia National Laboratories
Dominion Engineering, Inc.

ORDERING INFORMATION

Requests for copies of this report should be directed to the BWRVIP Program Manager, 3412 Hillview Ave., Palo Alto, Ca. 94304, (415) 855-2340.

ACKNOWLEDGMENTS

The members of the BWRVIP Crack Growth Working Group, listed below, are gratefully acknowledged for their efforts which led to the successful completion of this document.

Jai Brihmadesam (Chairman)	Entergy Operations
Robin Dyle	Southern Nuclear Company
George Inch	Niagara Mohawk Power Corp.
Tony Giannuzzi	Structural Integrity Associates
Ed Hartwig	Tennessee Valley Authority
Ron Horn	GE Nuclear Energy
Steve Leshnoff	GPU Nuclear
Dave Morgan	Pennsylvania Power & Light
Larry Nelson	Electric Power Research Institute
Raj Pathania (Project Manager)	Electric Power Research Institute
Kathleen Ramp	Electric Power Research Institute
John Wilson	Public Service Electric & Gas
Vaughn Wagoner	Carolina Power & Light
Joan Bozeman	Carolina Power & Light

Principal Investigators:

N. G. Cofie	Structural Integrity Associates, Inc.
A. J. Giannuzzi	Structural Integrity Associates, Inc.
M. L. Pytel	Structural Integrity Associates, Inc.
D. E. Delwiche	General Electric Nuclear Energy
B. M. Gordon	General Electric Nuclear Energy
R. M. Horn	General Electric Nuclear Energy
E. D. Eason	Modeling and Computing Services
A. A. Merton	Modeling and Computing Services
A. Peterson	EPRI Repair and Replacement Center
W. Cheng	University of California, Berkeley
I. Finnie	University of California, Berkeley
M. Shields	Sandia National Laboratories
S. Toledo	Sandia National Laboratories
T. Togami	Sandia National Laboratories
M. A. Kreider	Dominion Engineering, Inc
D. J. Gross	Dominion Engineering, Inc.
E. S. Hunt	Dominion Engineering, Inc.
J. Brihmadesam	Entergy Operations

EXECUTIVE SUMMARY

The purpose of this report is to provide a methodology for assessment of crack growth in BWR stainless steel shrouds and other stainless steel internals components. The assessment was limited to the circumferential welds of the shroud where most of the reported intergranular cracking has occurred to date. The methodology can however be easily extended to the vertical welds of the shroud and other BWR internals components with only minor modifications. This methodology has been developed specifically for crack growth in the radial (through-thickness direction). Residual and applied stresses and stress intensity factors have been developed for crack propagation in this orientation.

The methodology involves development of an empirical model which can account for the variability of important intergranular stress corrosion cracking (IGSCC) parameters in providing a conservative, yet realistic assessment of the crack growth rate (CGR) in BWR stainless steel components. The first step in the development of the evaluation methodology involved the determination of a crack growth model for stainless steel. Although a correlation has been previously provided by the U.S. Nuclear Regulatory Commission (USNRC), in their technical report NUREG-0313, Revision 2, it is believed by the BWR industry that this correlation does not adequately account for the varying degree of material and environmental conditions experienced by the entire fleet of operating BWRs. It is also believed that since the publication of this document in 1988, additional in-plant and laboratory crack growth data have become available and improved inspection and analytical tools are in hand which can be used to develop an alternative crack growth model; a model which can take into account variables which were not specifically addressed, but rather were bounded collectively, in the earlier NUREG correlation.

In Section 2 of this report, an extensive database consisting of stainless steel crack growth rates is described. This data came from several sources including General Electric Nuclear Energy (GE), ABB-Atom (ABB), and Argonne National Laboratories (ANL). The data included both experimental data points and in-plant crack arrest verification system (CAVS) data. Most of the data in the database have adequate definition of environmental conditions and other important crack growth parameters thus permitting a more realistic generic crack growth model to be developed.

The database was used in Section 3 of this report to derive an empirical, stress intensity factor (K) dependent crack growth law which also accounts for environmental conditions such as conductivity, electrochemical potential (ECP) and temperature. The development of the model was based on pattern recognition and multivariate modeling techniques which have been used quite successfully in previous similar projects. A best-fit model was derived based on the data and a crack growth curve based upon the 95th percentile on this best-fit model was recommended for crack growth evaluation of the shroud and other stainless steel internals. The 95th percentile is a factor of 10.3 higher than the best-fit correlation. It should be noted that this model is an empirical correlation based upon available data and engineering judgement. This empirical crack growth model, because of the limited nature of the data available, was based predominantly on test data for sensitized material tests, and a limited number of tests on non-sensitized material. Other crack growth correlation are available which address sensitization and radiation effects. The empirical correlation is applicable, therefore,

for weld-sensitized components and is bounding for non-sensitized components. The model is applicable over the specific ranges of variables examined and is recommended for use solely within these ranges. It should be noted that the range of variables addressed by this empirical correlation represents the water chemistry, material, and stress conditions expected in BWR service.

The second aspect of the evaluation methodology addressed operating and residual stresses experienced by the circumferential welds of the shroud and the associated stress intensity factor (K). The operating stresses of the shroud are relatively low and can be determined readily from the stress reports. A major portion of Section 4 of this report deals with weld residual stresses developed during fabrication of the shroud. Both experimental measurements and analytical techniques were used to determine surface and through-wall residual stress distributions for the circumferential welds of the shroud. Based on these results, a recommendation was made for a single through-wall residual stress distribution for the shell-to-shell and shell-to-ring welds. In general, this recommended residual stress distribution is similar to that recommended by the USNRC in NUREG-0313, Rev. 2 for application to large diameter stainless steel piping. The middle half of the curve is compressive while the outer ends are tensile. It should be noted that variability due to fit-up stresses, weld joint geometry, welding parameters such as heat input, weld sequence, welding starts and stops and repairs, can affect local residual stress distributions. Other stresses, such as oxide wedging, may also play a role in defining the total stress state. Although the magnitude of these stresses is difficult to define, the effect on field through-thickness crack growth appears to be reasonably bounded by the stresses defined within this report. However, in general, the residual stress distribution is as defined in this report.

In Section 5 of this report, fracture mechanics models were used to determine the through-wall stress intensity factor (K) distributions for the recommended residual stress profiles. A single distribution was determined for both inside and outside surface initiated flaws of the shroud. Because of the shape of the through-wall residual stress profile, higher K values were obtained near the wall surfaces indicating high crack growth rates at these locations. K diminishes as the crack propagates into the wall which leads to significantly lower crack growth rates or possible crack arrest at the shroud mid-wall.

The evaluation methodology for determination of crack growth rate for BWR shrouds is provided in Section 6. Three parallel alternate approaches are outlined in this section and are presented in the order of complexity. Any of these three approaches can be used for the evaluation.

Content Deleted -
EPRI Proprietary Information

Content Deleted -
EPRI Proprietary Information

It is proposed that the BWRVIP crack growth correlation and methodology presented in this report should be used to evaluate crack growth in core shroud welds and other stainless steel internals. It is believed that application of this methodology provides assurance that BWRs with cracks in the core shroud can continue to operate safely while reducing utility costs by supporting reasonable intervals for reinspection and avoiding the costs of unnecessary or premature repairs.

Table of Contents

Section		Page
1.0	INTRODUCTION	1-1
1.1	Background on Cracking of Stainless Steel Internals	1-1
1.2	Objective and Scope	1-6
2.0	COMPILATION OF CRACK GROWTH DATA	2-1
2.1	Structural Integrity Associates Database	2-1
2.2	GE Nuclear Energy Database	2-2
3.0	EMPIRICAL CRACK GROWTH CORRELATION STUDIES	3-1
3.1	Evaluation of the Database for Model Development	3-1
3.2	Development of Empirically-based Stainless Steel Crack Growth Rate Correlation	3-2
3.3	Correlation Models	3-5
3.4	Comparison of Model Predictions With Experimental Data	3-7
3.5	Comparison of Model Predictions With Field Data	3-8
4.0	OPERATING AND RESIDUAL STRESS EVALUATION	4-1
4.1	Operating Stresses Experienced by Core Shroud	4-1
4.2	Background on Weld Residual Stresses	4-1
4.3	Residual Stress Measurements of Core Shroud Welds	4-2
4.4	Analytical Determination of Residual Stresses in Core Shroud Welds	4-7
4.5	Comparison Between Experimental and Analytical Results	4-10
4.6	Recommendation of Residual Stress Distribution for Analysis of Core Shroud Welds	4-11
4.7	Stress Relaxation Effects	4-13
5.0	FRACTURE MECHANICS CONSIDERATIONS	5-1
5.1	Stress Intensity Factors Due to Applied Stresses	5-1
5.2	Stress Intensity Factors Due to Weld Residual Stresses	5-2
5.4	Allowable Flaw Size for BWR Shroud	5-4
6.0	EVALUATION METHODOLOGY FOR CORE SHROUD CRACK GROWTH	6-1
6.1	Evaluation Procedure	6-1
6.2	Example of Plant-Specific Analysis	6-2
7.0	SUMMARY AND CONCLUSIONS	7-1
8.0	REFERENCES	8-1

APPENDIX A Crack Growth Rate Data: ABB Atom and Argonne National Laboratories . . A-0

APPENDIX B Crack Growth Rate Data: GE Nuclear Energy B-0

APPENDIX C Crack Growth Rate Correlation C-0

APPENDIX D River Bend Shroud Material Properties D-0

APPENDIX E Near Surface Residual Stress Measurements at River Bend Nuclear Station . E-0

APPENDIX F Through-Thickness Residual Stress Measurement on River Bend Core Shroud F-0

APPENDIX G Near Surface Residual Stress Measurements atGrand Gulf Nuclear Station . G-0

APPENDIX H Analytical Residual Stress Determination (DEI) H-0

APPENDIX I In-Plant Crack Extension Determination from Successive UT Examinations . I-0

APPENDIX J Plant-Specific Crack Extension Calculations - Comparison with the Empirical Model J-0

List of Tables

Table		Page
3-1	Variables and Range of Calibration Data Considered in Crack Growth Correlation Studies	3-9
4-1	Operating Stress for Plant A	4-14
4-2	Operating Stress for Plant B	4-15
4-3	Summary of Near Surface Residual Stress Measurements at Grand Gulf Nuclear Station	4-16
4-4	Summary of Near Surface Residual Stress Measurements at River Bend Nuclear Station	4-17
4-5	Recommended Through-Wall Axial Residual Stress Distribution for BWR Shroud Welds	4-19
5-1	Normalized Through-Wall Stress Intensity Factor Distribution for BWR Shroud Welds	5-6
6-1	Results of Crack Growth Analysis for Example Problem	6-5

List of Figures

Figure		Page
1-1	Typical BWR Core Shroud	1-9
1-2	Location of BWR Core Shroud Circumferential Welds (BWR 3/4)	1-10
1-3	Location of BWR Core Shroud Circumferential Welds (BWR 6)	1-11
1-4	Typical Weld Details of Core Shroud Circumferential Welds	1-12
3-1	Effect of Conductivity	3-10
3-2	Effect of K on Crack Growth of Type 304 Stainless Steel	3-11
3-3	Effect of Temperature on Crack Growth of Type 304 Stainless Steel	3-12
3-4	Effect of ECP on Crack Growth of Type 304 Stainless	3-13
3-5	Model Prediction for Best-fit and 95th Percentile for Conductivity of 0.3 μS/cm	3-14
3-6	Comparison of Stainless Steel Crack Growth Model Predictions (95th Percentile) with Experimental Data (Conductivity of 0.1 μS/cm Temperature of 288°C and varying ECP)	3-15
3-7	Comparison of Stainless Steel Crack Growth Model Predictions (95th Percentile) with Experimental Data (Conductivity of 0.2 μS/cm Temperature of 288°C and varying ECP)	3-16
3-8	Comparison of Stainless Steel Crack Growth Model Predictions (95th Percentile) with Experimental Data (Conductivity of 0.3 μS/cm Temperature of 288°C and varying ECP)	3-17
3-9	Comparison of Model Prediction With Field Data	3-18
4-1	NRC Accepted Axial Weld Residual Stress Distribution for Large Diameter Piping	4-20
4-2	Test Specimens for Through-Wall Residual Stress Measurements at River Bend Nuclear Station	4-21
4-3	Weld Profiles and Planes for Through-Wall Weld Residual Stress Measurements at River Bend Nuclear Station	4-22
4-4	Comparison of Experimental and Analytical Through-Wall Residual Stress Distribution for Weld H5	4-23
4-5	Comparison of Experimental and Analytical Through-Wall Residual Stress Distribution for Weld H6a	4-24
4-6	Comparison of Experimental and Analytical Through-Wall Residual Stress Distribution for Weld H6b	4-25
4-7	Through-Wall Axial Residual Stress Distributions in HAZ for Shell-to-Shell Weld of Core Shroud (H4/H5) and Comparison with Recommended Curve	4-26
4-8	Through-Wall Axial Residual Stress Distributions in HAZ for Core Shroud Shell-to-Ring Welds (H2/H3) and Comparison With Recommended Curve	4-27
4-9	Through-Wall Axial Residual Stress Distribution in Weld for Core Shroud H6a Shell-to-Ring Welds and Comparison With Recommended Curve	4-28
4-10	Through-Wall Axial Residual Stress Distribution for Core Shroud H6b Shell-to-Ring Welds and Comparison With Recommended Curve	4-29
4-11	Comparison of Experimental Measurements (Surface and Through-Wall) With Recommended Curve	4-30

List of Figures
(concluded)

Figure		Page
4-12	Stress Relaxation Due to Neutron Irradiation	4-31
5-1	Parameter F_t to Describe Stress Intensity Factor K_I for the Part-Through-Wall, Part Circumference Flaws	5-7
5-2	Magnification Factors for Circumferential Crack in Cylinder (t/R = 0.1)	5-8
5-3	Recommended Normalized K_I Distribution for BWR Shroud Welds (ID and OD Initiated Flaws)	5-9
5-4	Flaw Reduction Factors for Determination of K_I for Weld Residual Stresses in BWR Shrouds With Part-Circumference Flaws	5-10
5-5	Effect of Localized Membrane Stress on K_I Distribution for BWR Shroud Welds (ID and OD Initiated Flaws)	5-11
6-1	Through-Wall Stress Intensity Factor Distribution for Example Problem	6-9
6-2	Results of Crack Growth Analysis for Example Problem	6-10

1.0 INTRODUCTION

1.1 Background on Cracking of Stainless Steel Internals

The problem of intergranular stress corrosion cracking (IGSCC) in austenitic stainless steels and in nickel-based austenitic materials has presented a serious concern to plant availability for boiling water reactor (BWR) owners during the past 20 years. Initial observations of IGSCC in BWRs were associated with severely sensitized wrought Type 304 stainless steel piping that resulted from post weld heat treatment or high heat input welding. Additional service history revealed that these severe thermal treatments of materials prior to service were not necessary to cause IGSCC; that cracking could occur in weld-sensitized components, welded with moderate heat input and with no subsequent thermal treatment. The utility industry through the Electric Power Research Institute (EPRI), the vendors, and contractors, led by GE Nuclear Energy (GE), research groups, and the Nuclear Regulatory Commission (NRC), expended significant time and financial resources to address the IGSCC issue and to provide remedial measures to the cracking. The NRC issued several documents including Inspection and Enforcement (I&E) notices, bulletins, regulatory guides, and generic letters on the issue.

EPRI sponsored research which resulted in technical reports, and guidelines and EPRI conducted workshops on the issue. GE performed research and prepared service information letters addressing the IGSCC issue and advising the utility industry on actions appropriate to address the problem. Although the cracking in austenitic materials was widespread, until recently it was generally confined to components outside of reactor pressure vessel.

During the past decade, IGSCC of austenitic stainless steels and nickel-based alloys has begun to be observed within the reactor pressure vessel. Components such as jet pump beams, riser braces, access hole covers, core spray piping, feedwater spargers, shroud hold-down bolts, reactor pressure vessel cladding and the core shroud are among the vessel internals components which have recently exhibited cracking.

Cracking of vessel internals has involved both austenitic stainless steels and nickel-based alloys. Until the recent core shroud cracking, the IGSCC observed was readily manageable with existing means and did not significantly impact design safety margins of the plant. The core shroud cracking has been sufficiently significant in some plants to warrant repairs to the cracked weld heat affected zones or to require more frequent core shroud inspections.

The following paragraphs in this section describe the factors which contribute to the IGSCC observed in the core shroud, as limited to austenitic stainless steels, the industry experience with shroud cracking and the real and potential impact on the BWR Owners.

Cause of Cracking

Based upon prior work sponsored by EPRI, industry research groups and the NRC, the generally accepted factors responsible for IGSCC in austenitic stainless steels and nickel-based austenitic materials in the normal BWR environment are sufficient tensile stress, thermal sensitization and a sufficiently oxidizing environment. An additional factor which may contribute to intergranular cracking after long operating times at high neutron fluences is the effect of irradiation on the stress corrosion cracking susceptibility of the material.

The total stress-state of a material includes applied and residual stresses. The applied stresses are the operating stresses to which the material is subjected in service and can be readily bounded by engineering stress analyses. The residual stresses include fabrication stresses such as machining, grinding and welding stresses and fit-up stresses associated with the component installation. It is generally accepted that these combined stresses must be near the material yield strength at temperature for IGSCC to occur.

Thermal sensitization of these alloys involves chromium depletion at the grain boundaries due to chromium carbide precipitation. The chromium depleted zone is no longer a "stainless" material but rather an alloy steel anode galvanically coupled to a large stainless steel cathode. If sufficient tensile

stress is present at a sufficient temperature and in an oxidizing environment, then IGSCC can occur if the environment can support the corrosion reaction.

The environment influences the IGSCC of austenitic materials in the BWR environment in two ways. The normal BWR water environment is an oxidizing environment which contains dissolved oxygen and hydrogen peroxide as a result of the breakdown of water by radiation in the core region. This environment has been demonstrated to be sufficiently aggressive to cause IGSCC in weld-sensitized austenitic stainless steels at BWR operating temperatures. The capacity of the environment to oxidize metals can be measured as the electrochemical corrosion potential (ECP). Under normal water chemistry conditions, the ECP will range from 0.0 volts (relative to the standard hydrogen electrode) to +0.2 volts. Hydrogen can be injected to reactor water to suppress radiolysis in the core and to consume oxidizing species and thus lower the ECP. IGSCC is essentially halted at values below -0.23 volts. This is the basis for hydrogen water chemistry.

The second environmental factor influencing IGSCC of austenitic materials is the concentration of strong acid anions such as chloride and sulfate. These accelerate IGSCC behavior in alloys in the BWR environment. Other ionic species such as chromates and nitrates, sodium and zinc are much less aggressive. In fact some species, such as zinc, may be beneficial to the IGSCC resistance of these materials. The concentration of ionic species is proportional to the electrical conductivity of reactor water. The relationship between conductivity and the concentration of aggressive anions will be plant specific. However, conductivity measurements provide a bounding indication of the concentration of these impurities.

The core shroud is also affected by neutron and gamma radiation which may impact austenitic stainless steel IGSCC resistance in two ways. The core shroud environment, is believed to be highly oxidizing due to the formation of hydrogen peroxide as a result of radiolytic decomposition of the water within the core. This leads to an elevated ECP which increases the IGSCC damage to materials in the BWR environment.

The second way the radiation exposure increases the IGSCC susceptibility of austenitic materials is due to the radiation damage to the material itself. High levels of neutron exposure cause vacancies and voids to form in these alloys enhancing the rates of segregation of impurities to grain boundaries and also enhancing chromium depletion at these grain boundaries. This "non-thermal" irradiation induced sensitization is generally observed in these austenitic materials in the range of fluences of ~5×10^{19} to 5×10^{20} n/cm^2 E > 1.0 MeV and above. A fluence of 5×10^{19} n/cm^2 E > 1.0 MeV can be achieved in as little as approximately one to two full power years in a high flux location of a typical BWR core shroud. The effect of neutron irradiation on the stress corrosion susceptibility of these austenitic materials is known as irradiation assisted stress corrosion cracking (IASCC).

Content Deleted -
EPRI Proprietary Information

Industry Core Shroud SCC Experience

During the past five years, cracking has begun to be observed within the core shroud of BWRs. First observed in 1990 in a European plant, cracking (or crack like indications) have been reported in several overseas plants and a large number of plants in the United States. The cracking has generally been confined to the weld heat affected zone (HAZ) in circumferential welds in the core shroud. Figures 1-1 through 1-3 illustrate the circumferential weld locations in a typical BWR 3/4 and BWR 6 core shroud. As can be seen from the weld details in Figure 1-4, all those welds are welded from both sides, with the exception of the dissimilar metal weld, H7. The cracking has generally occurred in Type 304 stainless steel weld HAZs although some cracking has also been observed in Type 304L stainless steel weld HAZs. Some limited cracking has also been reported in vertical welds in one or two plants, and the weld metal may have been involved in cracking of one U.S. plant.

The circumferential cracking in the austenitic stainless steel weld HAZs has been modest for some plants, severe in others, and non-existent in other plants. Some correlation with shroud fabrication or prior water chemistry history has been observed since it appears that the newer plants or those

operating with good water quality appear to have had less cracking than those operating with poorer initial water quality. Fabrication process may play an important role in crack initiation as plate-exposed "end grain" and severe machining or grinding appear to be contributors to early crack initiation. Total neutron fluence may be playing a role on crack initiation in some high fluence plants and the effect of irradiation on oxidizing potential may be assisting in crack growth in some of the beltline core shroud welds in high fluence plants.

Real and Potential Impact on Utilities

The intergranular stress corrosion cracking which has occurred within the core shroud of BWRs has produced a new, significant operational and financial burden to the BWR utility owners. The cracking in the circumferential welds of some plants have raised issues as to the length of continued operation of the plant prior to reinspection or repair of a flawed core shroud. Although, the design safety margins for the core shroud have not been impacted to date, as a result of inspections or analyses performed on operating plants, concerns exist that these extremely conservative analyses justifying continued operation may impose additional inspection hardship or require unnecessary repair to the core shroud. This concern and the concern that at some future time the design safety margins might be affected has prompted the formation of a high level BWR Vessel and Internals Project (BWRVIP) by the BWR industry, with EPRI acting as project manager and coordinator. The objective of this project has been to understand the cracking phenomena within the vessel internals, provide mitigating measures to limit any future cracking, develop advanced inspection and analytical tools to monitor and realistically bound the cracking and design and implement state-of-the-art repair measures to restore margin to the core shroud and other internals.

The utility industry has been burdened with the need to perform extensive inspections of their BWR core shrouds to assess the condition of the shroud. While the initial inspections were performed using enhanced visual techniques, access limitations have prompted most utilities to perform the most recent inspections using volumetric ultrasonic methods. These inspections have required development of new state-of-the-art equipment to inspect these welds and weld heat affected zones with precision and to accurately determine the IGSCC condition of these components. As the extent of cracking

has become more widespread, inspections have been required at lower elevations in the core shroud involving welds H6, H7, and H8, where very limited access is available for positioning tracking equipment and transducers.

One of the major issues facing the utility industry with regard to the core shroud inspection is the issue of core shroud reinspection and premature repair which can impose an unnecessary economic hardship on the utility. The reinspection interval is dependent upon the extent of cracking observed during the baseline examination and prediction of the crack growth as a function of future operating time. The current methodology for determining reinspection interval is based on characterizing all observed cracks as through-wall cracks and propagating these cracks around the circumference of the shroud assuming a conservative crack growth rate of 5×10^{-5} in/hr. It is believed that a more realistic reinspection interval can be established if a crack growth model is developed which can account for both the through-thickness and the circumferential growth of the cracks. This crack growth model should include estimates of weld residual stresses in these circumferential welds as a function of crack depth and circumferential extent, degree of sensitization of the material, and the environments to which the core shroud is exposed. These environments vary within the shroud from very oxidizing at and above the core midplane, to moderately oxidizing below the core plate. In fact, under moderate hydrogen water chemistry (HWC) environment (1.0 to 1.6 ppm H_2), the ECP below core plate locations can be reduced to less than -230 mV(SHE) potential required for IGSCC protection of weld HAZs.

1.2 Objective and Scope

The objective of this report is to formalize the methodology for determination of stainless steel crack growth rates, based on empirical data that account for parameters that are known to effect crack propagation. These crack growth rates (CGR) will then be available for use in the evaluation, inspection and repair criteria for BWR RPV internal components. The scope of CGR influencing factors will be tied to typical material susceptibility, water environment, and stress-state parameters associated with core shroud weld and weld HAZ. An empirical model will be developed that incorporates the effects of the important factors into a conservative, yet realistic, crack growth

correlation for stainless steel in the BWR internals. The model developed in this report is an empirical correlation for through-thickness crack growth based upon available test data and engineering judgement. The correlation is developed using material, environment, and stress data which result from laboratory and in-plant test programs. It is then tested against field data and found to provide a realistic bound to the growth rates oberved over the BWR operating regime.

The following sections of this report describe the work undertaken within this project to understand the state of stress, and material variability on the crack growth rates of austenitic stainless steels at ECPs and conductivities corresponding to those observed within the BWR core shroud under normal water chemistry (NWC) conditions as well as under hydrogen water chemistry (HWC) conditions. Section 2 presents a compilation and assessment of crack growth data produced by laboratories and in field testing. This collection of data provides a compiled database for use in determining crack growth rates as a function of environment and stress intensity in sensitized austenitic stainless steel. Section 3 provides an empirical crack growth rate correlation developed using material, environment and stress information provided in Section 2. This correlation is based upon sensitized material tests. The correlation is applicable, therefore, for weld-sensitized components and is bounding for non-sensitized components. The model is applicable over the specific ranges of stress intensity, water conductivity and ECP for which the correlation was developed. Section 4 provides the operating and residual stress data for the core shroud materials. Fracture mechanics methods employed in determining the stress intensity factors associated with the applied and residual stresses are presented in Section 5. Section 6 presents the evaluation methodology for estimation of crack growth rates in the through-thickness direction for BWR shrouds. Three alternate approaches are presented; a K-independent approach, a conservative 95th percentile K-dependent approach using the empirical correlation developed in this report along with conservative ECP and water chemistry; and a plant-specific approach using actual plant ECP and water chemistries with the empirical correlation. An example problem on crack growth evaluation of the shroud using the methodologies outlined in Sections 1 through 5 for a plant-specific analysis is also presented in Section 6. Section 7 presents the Summary and Conclusions from this study and provides the empirical correlation which can be used to conservatively predict the crack growth rate for austenitic stainless steels at various ECPs corresponding to different locations in the core shroud. Section 8 provides references used in the

report. Detailed studies performed by several individual organizations to support the work presented in the main body of the report are presented in Appendices A through J.

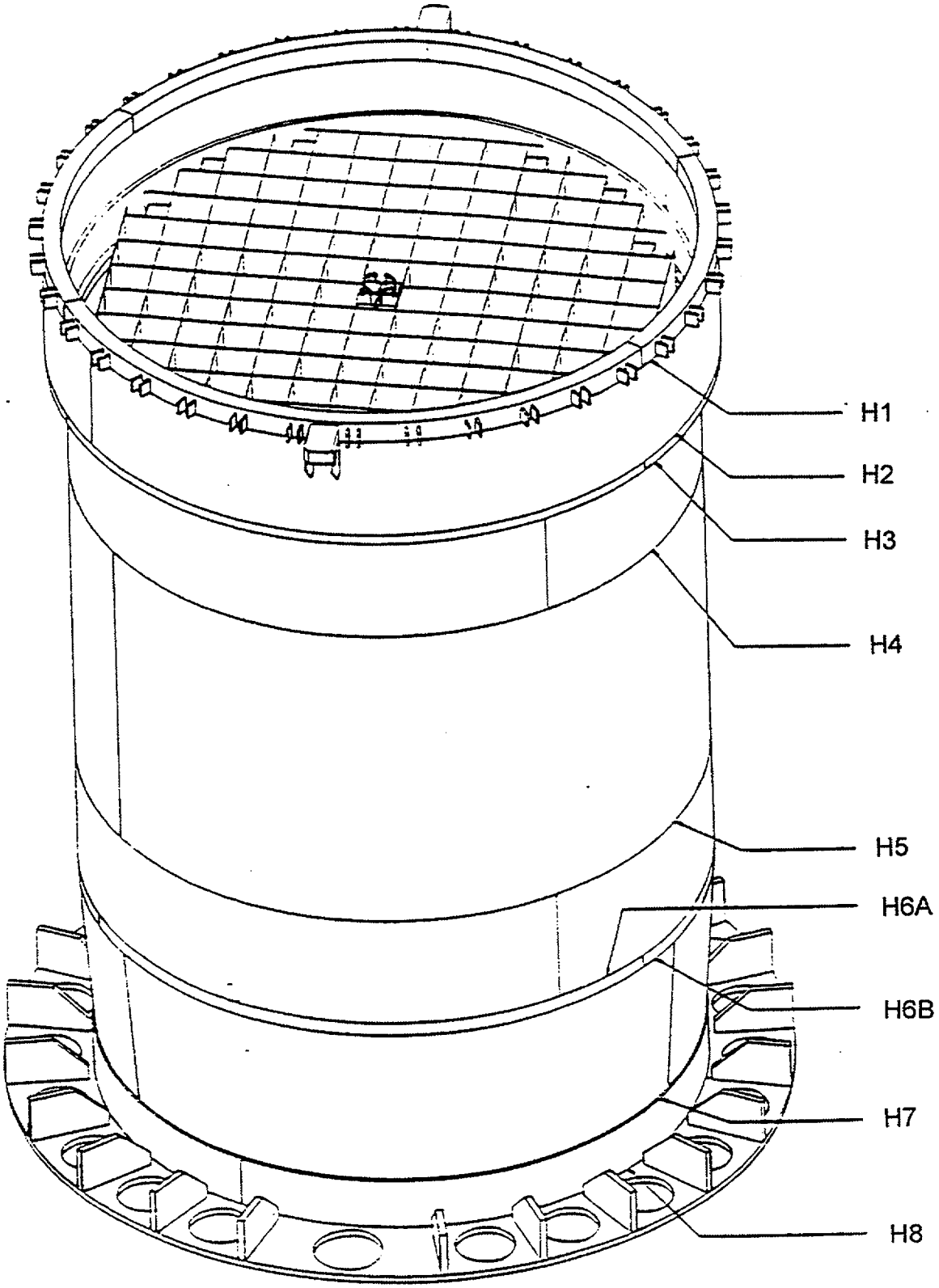

Figure 1-1. Typical BWR Core Shroud

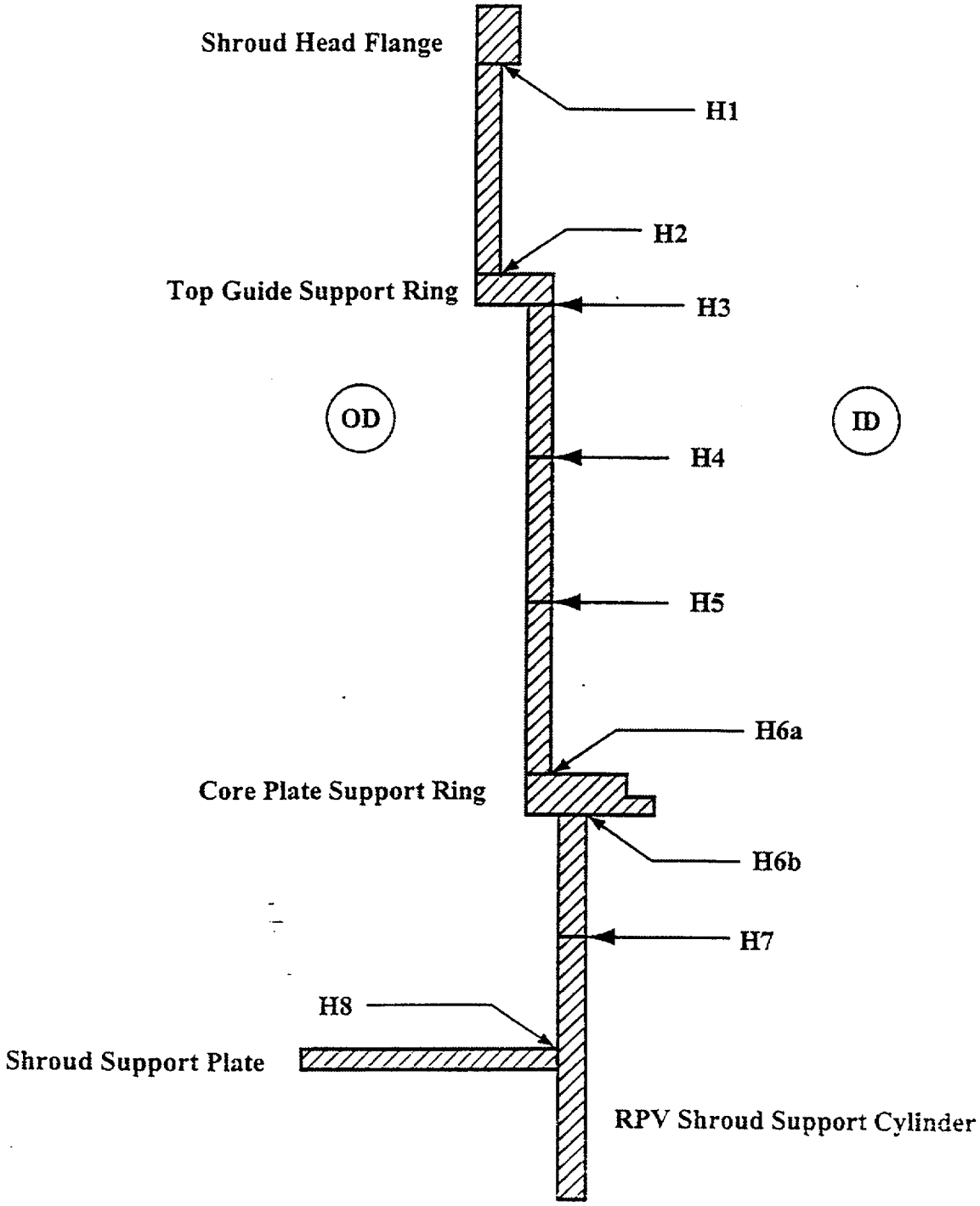

Figure 1-2. Location of BWR Core Shroud Circumferential Welds (BWR 3/4)

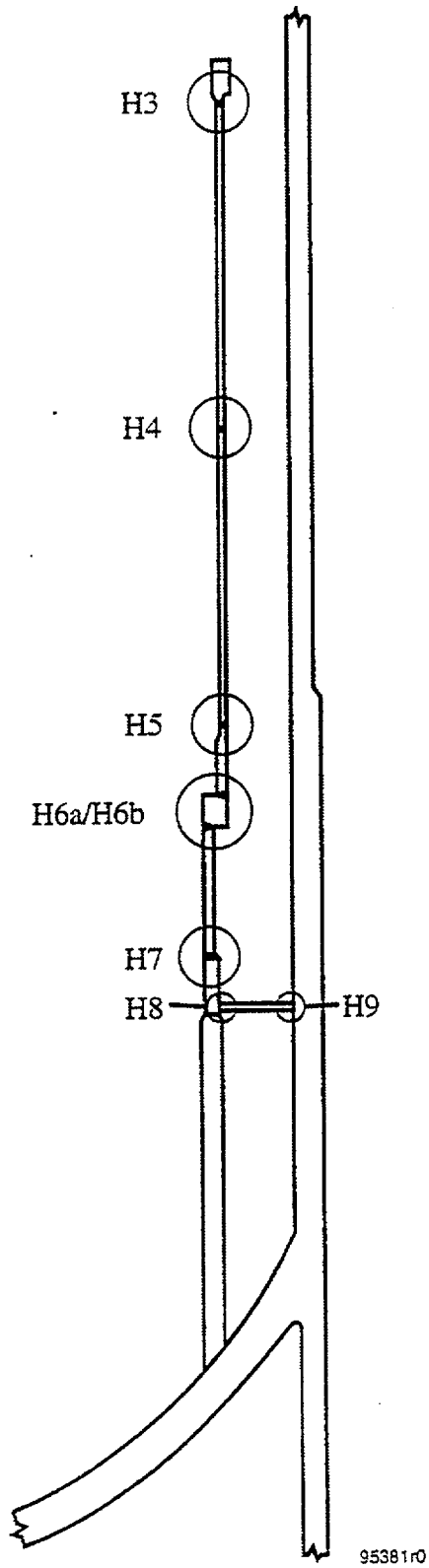

Figure 1-3. Location of BWR Core Shroud Circumferential Welds (BWR 6)

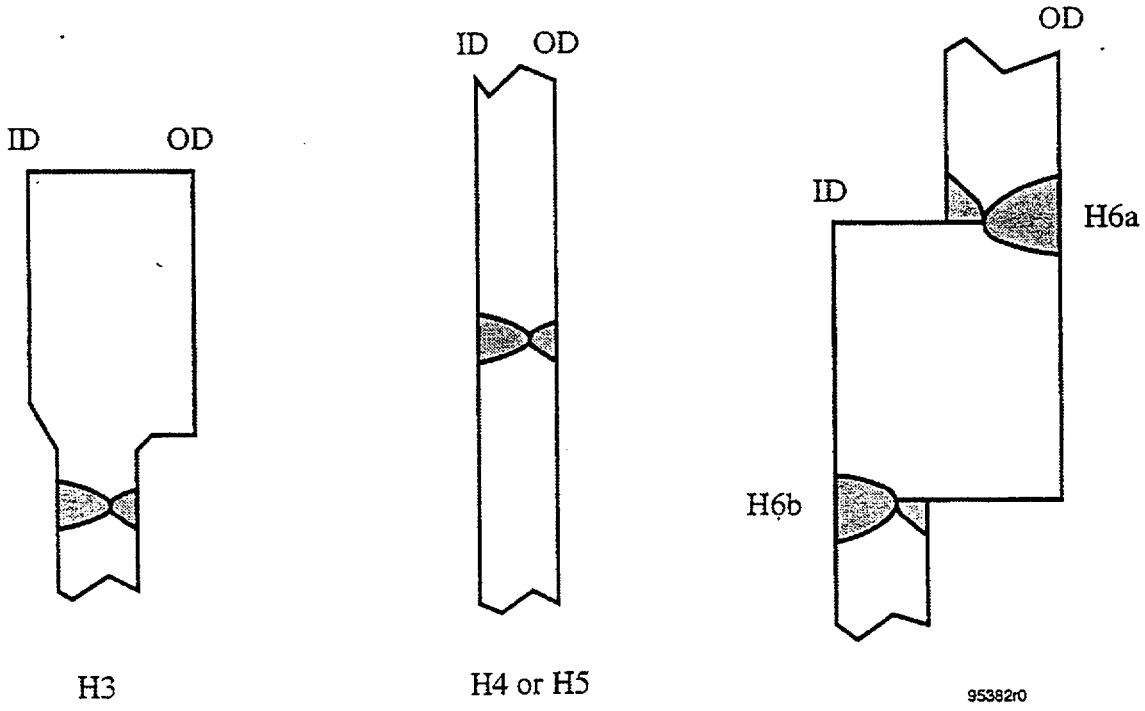

Figure 1-4. Typical Weld Details of Core Shroud Circumferential Welds

2.0 COMPILATION OF CRACK GROWTH DATA

Two separate databases were created to assist in the through-thickness crack growth correlation development for austenitic stainless steels. The first database was created by Structural Integrity Associates (SI) based on available information in several EPRI-sponsored research projects and also from work sponsored by the USNRC. The second database was based on laboratory and CAVS data developed by GE Nuclear Energy (GE).

2.1 Structural Integrity Associates Database

Details of this database are provided in Appendix A of this report. The data for this database was obtained from ABB-Atom through EPRI and from NRC-sponsored research at Argonne National Laboratories. The data from these two sources were chosen because, unlike other stainless steel crack growth data, they have all the identifiable testing parameters and testing conditions for all the test data. The data obtained from these sources were judged to be excellent in terms of completeness, relevance and traceability. Table 2-1 lists all the parameters that are associated with each of the test data in this database. References from which data was compiled are provided in Appendix A.

A total of 170 data points were obtained from ABB-Atom. The data included tests on corrosion fatigue and constant load tests. Most of these data were cyclic data. A total of 44 data points for Type 304 under constant load were used in the model formation. A summary of the range of data from this source is as follows:

A total of 272 data points were obtained from Argonne National Laboratories. Similarly, this data also consisted of corrosion fatigue and constant load tests. From this population, a total of 7 Type 304 constant load tests were used in developing the crack growth correlation. The following provides a summary of the range of key parameters contained in this database:

Content Deleted -
EPRI Proprietary Information

2.2 GE Nuclear Energy Database

Details of this database are provided in Appendix B of this report. The data were derived from two different sources (see Appendix B for references to the source of data). The first source of data were the studies that were performed as part of the pipe cracking investigations and were used as the basis for the NRC disposition line [3]. The data were reassessed for the test conditions and the stated crack growth rate. The tests that were performed were largely performed by GE. The tests that were performed were conducted in one of two environments: 0.2 ppm oxygen and 6 ppm (referred to in the literature as 8 ppm due to the upper test specification limit) oxygen 288°C high purity BWR water. The tests were conducted at conductivity levels that are higher than the conductivity levels associated with the current typical operational levels at BWRs. The data were performed under well-controlled test conditions and are useful to expand the total range for the correlation development. The tests that were run did not include any ECP measurements. Therefore, the ECP were assigned based on the test environment. The ECP assigned was derived from a comparison of several ECP/water chemistry correlations. The ECP values that were assigned were 60 mV(SHE) and 120 mV(SHE) for the GE 0.2 ppm and 6 ppm tests, respectively. Because of the uncertainty about ECP,

this data set was not used to develop the correlation but was used to test the correlation as illustrated in Appendix C.

The second, comprehensive data summary was developed by reviewing and assigning crack growth rates to the data from CAVS tests that were performed at actual operating plants. These tests were performed at Brunswick 1, Duane Arnold, FitzPatrick, Hatch 1, Limerick, Nine Mile Point 1, Pilgrim, Peach Bottom 2 and 3, and an overseas plant over the time period of 1988 through 1993. These test systems included ECP measurements and are fully documented tests. Data from these tests were used to develop the crack growth correlation.

3.0 EMPIRICAL CRACK GROWTH CORRELATION STUDIES

The database of laboratory data developed by Structural Integrity Associates (SI) and GE Nuclear Energy (GE) in Section 2 of this report are analyzed for the purpose of developing an empirical crack growth correlation for stainless steel. The objective is to analyze the data so as to derive a crack growth model of the form,

$$\frac{da}{dt} = CK^n \tag{3-1}$$

where K is the stress intensity factor. K is a parameter which describes the stress field near a crack. It is dependent on the applied stresses, the crack size and the geometry of the cracked body. The other parameters in Equation 3-1 are C, an environmental term, a, the crack depth, t, the time, and n, a power exponent. In this expression, C and possibly n may depend upon the electrochemical potential, the conductivity, and other variables as appropriate.

3.1 Evaluation of the Database for Model Development

The combined database was evaluated to ensure that only relevant data was used in the model correlation development. From this evaluation, it was observed that nearly half of the data were CAVS data provided by GE. These data are representative of plant water ionic species. The tests were conducted in autoclaves that were attached directly to various locations in the reactor coolant loop. Limited in-core crack growth data were also available from four reactors. These data were not used to develop the correlation but were instead used to test the final correlation (Appendix C). These data were excluded in developing the correlation since they are irradiated and the fluence was not available. There is presently considerable uncertainty as to the exact mechanism(s) that are responsible for irradiation-assisted stress corrosion cracking (IASCC), but it is also known that fluence is an important variable for correlating IASCC [1], and accurate values for that variable were not available within the in-core specimen database. In addition, they are wedge-loaded double cantilever beam (DCB) specimens whereas the specimens used to develop the correlation were thermally sensitized and were actively loaded compact tension (CT) specimens. One observation

Some CAVS specimens were listed with a comment in the database, such as start-up, beginning of hydrogen injection, hot standby, etc. These short-term transient conditions are not representative of the long duration, steady operating conditions. Consequently, data from these specimens were not used in the analysis.

Having eliminated the above data from further considerations, the resulting database had 122 useable observations which were used to develop the crack growth correlation model for stainless steel. The adequacy of this resulting database for model development is discussed in Appendix C of this report.

3.2 Development of Empirically-based Stainless Steel Crack Growth Rate Correlation

The empirically-based stainless steel crack growth rate correlation was developed using the pattern recognition and multivariate modeling tools that they have used on several previous projects [1,2]. Additional details of the model development are provided in Appendix C of this report and only a summary is provided in this section. The steps in the analysis included identifying correlations among the presumed independent variables, using pattern recognition techniques to identify the most sensitive variables and the form of functional dependence, performing multivariable modeling by nonlinear least square techniques, and analyzing the quality of fit by statistical methods and by plotting normalized and residual plots. The list of the variables that were considered in the pattern recognition and their range of values are shown in Table 3-1. The effect of these variables on the

crack growth correlation is provided in the following pages. It is noteworthy that the test of the model is performed against a field data set using the least squares fit and a 95th percentile to encompass this data. This approach is used to illustrate the conservative nature of the model encompassing all but a few of the field data.

Conductivity.

Content Deleted -
EPRI Proprietary Information

Stress Intensity Factor, K.

Content Deleted -
EPRI Proprietary Information

Temperature.

Content Deleted -
EPRI Proprietary Information

Electrochemical Corrosion Potential, ECP.

Content Deleted -
EPRI Proprietary Information

Electrochemical Potentiokinetic Reactivation, EPR.

Content Deleted -
EPRI Proprietary Information

Content Deleted -
EPRI Proprietary Information

3.3 Correlation Models

The above observations were used to derive a crack growth correlation model for Type 304 stainless steel for application to the BWR shroud. For purposes of developing the correlation given here, only those observations with measured values of conductivity and ECP were used for model calibration. This prevented the use of older data points that were used in the NUREG-0313, Revision 2 document, because conductivity and ECP could only be estimated for those points.

Content Deleted -
EPRI Proprietary Information

The range of data used to develop the model is shown in Table 3-1. It is recommended that the model should be applied only within these limits.

The above expression in Equation 3-2 represents the mean of the $\ell n\left(\frac{da}{dt}\right)$ data. The agreement between the data and the model given by Equation 3-2 can be evaluated graphically by examining normalized plots, in which the data points are adjusted as well as possible to a set of common conditions (assuming that the model correctly reflects the effect of each variable). The equation for this adjustment is:

Content Deleted -
EPRI Proprietary Information

Referring to the normalized plots for the best-fit model, Figures 3-1 through 3-4, there is reasonable agreement between the data used for calibration and the model when all are adjusted as nearly as possible to common conditions. The common conditions were:

Content Deleted -
EPRI Proprietary Information

Figure 3-2 shows how the best-fit model (solid line) compares with the NUREG-0313, Revision 2 line (long dash) when plotted at the normalizing conditions given above. The short dashed line is the estimated 95th percentile of the residuals about the model, assuming they are log-normally distributed. The short dashed line is plotted at +1.645 standard deviation above the model (a factor

of 10.3 on da/dt). The line will be referred to as the 95th percentile model or correlation in this report.

Content Deleted -
EPRI Proprietary Information

3.4 Comparison of Model Predictions With Experimental Data

The predictions of the 95th percentile model [10.3*da/dt from Equation (3-2)] at the BWR operating temperature of 288°C and three levels of conductivities (0.1, 0.2, and 0.3 μS/cm) at varying ECP values are shown in Figures 3-6 through 3-8. Also shown on these figures are the experimental data points used in to derive the model and the NRC disposition curve in NUREG-0313, Revision 2 as well as a horizontal line representing a crack growth rate of 5×10^{-5} in/hr which is currently used in flaw evaluation of the shroud.

Content Deleted -
EPRI Proprietary Information

Content Deleted -
EPRI Proprietary Information

3.5 Comparison of Model Predictions With Field Data

The 95th percentile prediction and comparison with crack growth data from three plants (KKM, Chinshan, and Brunswick) are shown in Figure 3-9. Details of the crack growth rate evaluation for these plants are provided in Appendices I and J. Figure 3-9 illustrates the NUREG curve and the empirical model generated for an ECP of 200 mV(SHE) and a conductivity of ≤ 0.15 μS/cm. These conditions are believed to be conservative for the core shroud environment.

Content Deleted -
EPRI Proprietary Information

Table 3-1

Variables and Range of Calibration Data Considered
in Crack Growth Correlation Studies

Content Deleted -
EPRI Proprietary Information

Content Deleted -
EPRI Proprietary Information

Figure 3-1. Effect of Conductivity

Content Deleted -
EPRI Proprietary Information

Figure 3-2. Effect of K on Crack Growth of Type 304 Stainless Steel

Content Deleted -
EPRI Proprietary Information

Figure 3-3. Effect of Temperature on Crack Growth of Type 304 Stainless Steel

Content Deleted -
EPRI Proprietary Information

Figure 3-4. Effect of ECP on Crack Growth of Type 304 Stainless

Content Deleted -
EPRI Proprietary Information

Figure 3-5. Model Prediction for Best-fit and 95th Percentile for Conductivity of 0.3 μS/cm

Content Deleted -
EPRI Proprietary Information

Figure 3-6. Comparison of Stainless Steel Crack Growth Model Predictions (95th Percentile) with Experimental Data (Conductivity of 0.1 μS/cm Temperature of 288° C and Varying ECP)

Content Deleted -
EPRI Proprietary Information

Figure 3-7. Comparison of Stainless Steel Crack Growth Model Predictions (95th Percentile) with Experimental Data (Conductivity of 0.2 μS/cm Temperature of 288°C and Varying ECP)

Content Deleted -
EPRI Proprietary Information

Figure 3-8. Comparison of Stainless Steel Crack Growth Model Predictions (95th Percentile) with Experimental Data (Conductivity of 0.3 μS/cm Temperature of 288°C and Varying ECP)

Content Deleted -
EPRI Proprietary Information

Figure 3-9. Comparison of Model Prediction With Field Data

4.0 OPERATING AND RESIDUAL STRESS EVALUATION

Stresses associated with BWR shrouds can be classified into two broad categories; operational stresses and fabrication-related stresses. Operational stresses are those associated with the normal operation of the plant and consist of stresses analyzed in the ASME Code stress reports. Fabrication stresses for the shroud consist mainly of weld residual stresses resulting from welding the various shroud plates and rings. Additional fabrication stresses include machining or grinding stresses and fit-up stresses.

4.1 Operating Stresses Experienced by Core Shroud

Operating stresses in the BWR shroud are relatively low. The main contributors to operating stresses are differential pressure and seismic loads. The membrane and bending stresses for upset and faulted conditions for two typical plants are shown in Tables 4-1 and 4-2.

Content Deleted -
EPRI Proprietary Information

4.2 Background on Weld Residual Stresses

During fabrication of the shroud, several plates and rings are welded together to form the cylindrical shape. As a result of the welding, residual stresses are developed. Key factors that determine the magnitude and distribution of the residual stresses are heat input during welding; weld sequence, weld starts and stops, and cooling time between passes; surrounding joint geometry; fit-up strains required to make pieces match up; base/weld metal mechanical properties; local weld repairs; post weld heat treatment; and any post weld mechanical processes such as grinding and machining. Even though it is believed that residual stresses play a significant role in any potential cracking of the shroud, the magnitude of these stresses and their distribution have not been studied extensively for the shroud configuration. A considerable amount of experimental and analytical work performed to determine the residual stress of butt welds in stainless steel piping [3,7,8,9] have shown that, in general, near-yield level tensile residual stresses are developed on the inside surface. Small-diameter

piping welds (thickness < 1.0 inch), exhibit through-wall linear bending residual stress distribution with tensile yield level stress on the inside surface [7]. The through-wall distribution for large-diameter piping is U-shaped, as shown in Figure 4-1, with tension on the inside and outside surface and compression in the middle half of the pipe wall. Also shown in Figure 4-1 is the through-wall axial residual stress distribution accepted by the NRC for IGSCC crack growth evaluation of large-diameter piping. Since the thickness of a typical BWR shroud is 1.5 inches, it can be expected that the through-wall residual stress distribution will be similar to that of the large-diameter piping shown in Figure 4-1. However, there are some significant differences between the two components such that the large-diameter piping residual stress distribution may not be directly applicable to the shroud.

Content Deleted -
EPRI Proprietary Information

4.3 Residual Stress Measurements of Core Shroud Welds

The weld residual stress measurements of the shroud employed both surface residual stress measurements by using a blind hole drilling method and through-wall residual stress measurements utilizing the crack compliance method. The measurements were performed on spare BWR/6 shrouds for two plants that were never put in service as described in the following sections.

4.3.1 Near-Surface Residual Stress Measurements

The near-surface residual stress measurements were performed on spare BWR/6 reactor core shrouds at Grand Gulf Nuclear Station (GGNS) and River Bend Nuclear Station (RBNS). Details of these measurements are provided in Appendices E and G of this report. The following provides a summary of these measurements.

Measurements at Grand Gulf Nuclear Station (GGNS)

The spare shroud at GGNS was fabricated using Type 304L stainless steel and measured approximately 20 ft. high by 20 ft. in diameter with a wall thickness of approximately 2 inches. Residual stress measurements were made by Sandia National Laboratories, Albuquerque, New Mexico, at five weld locations on the outside (OD) surface and corresponding locations on the inside (ID) surface. These five locations corresponded to the H3, H4, H5, H6A, and H6B weld shown in Figure 1-1. At each location, measurements were made at the weld, the heat affected zone (HAZ) and outside the HAZ. The H3 OD, H6A ID, and H6B ID and OD weld crowns were not measured since they are fillet welds.

The residual stress measurements were made using the blind hole drilling method. This method is the standard technique used to determine surface residual stresses and described in ASTM Standard E837-94 [10]. The method involves bonding three strain gages in the form of a rosette at three angles, 0°, 45°, and 90° to form a circle. A hole is drilled in the middle of the rosette and as the hole is being drilled, the strain that is relieved is measured. The depth of the hole is limited to 40% of the gage diameter. Residual stresses can then be determined from the relieved strain using relationships provided in ASTM Standard E837-94. During the tests, a gage diameter of 0.202 inches and two hole diameters of 0.062 inches and 0.072 inches were utilized. The full depth of the drilled hole was 0.081 inches and the strain measurements made to a depth of 0.072 inches.

A total of 39 strain measurements were made on the shroud. Each measurement consisted of 10 strain readings recorded at .008 inch increments. The data was then reduced to calculate the hoop,

longitudinal, and shear stresses.

Content Deleted -
EPRI Proprietary Information

The results of the residual stress measurements are presented in Appendix G (Figures 2a, 2b, 2c, and 2d) and summarized in Table 4-3.

Content Deleted -
EPRI Proprietary Information

Measurements at River Bend Nuclear Station

The spare shroud at River Bend was also fabricated from Type 304L stainless steel with measured room temperature base metal yield stress of 35 ksi. Near surface residual stress measurements were made on both the inside surface and outside surface at welds H3, H4, H5, H6a, and H6b by the EPRI NDE Center staff. At each location, measurements were made, at 1/4 inch above the weld fusion line, the weld centerline and 1/4 inch below the weld fusion line.

The blind hole drilling method was also employed for the measurements consistent with the requirements of ASTM Standard E837-94 [10]. Strain readings were taken at consistent depth intervals and continued until the strain readings stabilized. This ensured that a direct correlation could be made among all rosettes and gages. The drilling continued to a consistent depth of 0.090 inch. The relief strain values stabilized at a drilled depth of about 0.060 to 0.075 inch. The strain measurements were then reduced to calculate the residual stresses.

The measured residual stresses are shown in Table 4-4.

Content Deleted -
EPRI Proprietary Information

4.3.2 Through-Thickness Residual Stress Measurements at River Bend Nuclear Station

Through-wall residual stress measurements of the shroud welds H5, H6A, and H6B at River Bend were performed by University of California, Berkeley using the crack compliance method. The theoretical background of this method and details of the methodology in application to the measurements of the shroud at River Bend are provided in Appendix F of this report. In summary, the method involves installing a strain gage at an optimal location of a specimen containing the weld.

An electrical discharge wire machining (EDWM) is used to introduce a thin cut of increasing depth in the specimen. The strain distribution during the cutting process is measured. The relationship between the stress released and the measured strain is given by:

$$\varepsilon(a) = \sum_{i=0}^{n} \frac{\sigma_i}{E'} C_i(a) \tag{4-1}$$

The unknown residual stress distribution is represented by a series:

$$\sigma(x) = \sum_{i=0}^{n} \sigma_i P_i(x) \tag{4-2}$$

where:

$P_i(x)$	=	the surface traction
σ_i	=	the amplitude factor for the ith term $P_i(x)$
E'	=	an elastic constant
$C_i(n)$	=	the crack compliance function for $P_i(x)$

The crack compliance functions were obtained by using fracture mechanics solutions in the literature or finite element analysis. When a number m > n+1 of strain measurements are made, a less square fit can be used to minimize the average errors involved in the measurement and estimation resulting in n+1 linearly independent equations given as:

$$\frac{\partial}{\partial \sigma_i} \sum_{j=1}^{m} \left[\varepsilon(a_j) - \sum_{k=0}^{n} \sigma_k C_k(a_j) \right]^2 = 0 \qquad i = 0, \ldots, n \tag{4-3}$$

from which the unknown σ_i can be solved.

The above procedure was used to determine the through-wall residual stress distribution in the shroud for welds H5, H6a, and H6b. The geometry of the specimens that were used to obtain the measurements are shown in Figure 4-2, and the weld profiles as well as location of the measurements are shown in Figure 4-3. The strain and the through-wall residual stress distributions are presented in Appendix F (Figures F-4 through F-9).

The use of this procedure required that the specimen be cut out of the shroud. Details of the parting out of the test specimen from the shroud for the through-wall residual stress measurements are provided in Appendix E.

Content Deleted -
EPRI Proprietary Information

The original residual stress (σ_r) in the shroud consists of two parts:

$$\sigma_r = \sigma_1 + \sigma_2 \tag{4-4}$$

where: σ_1 = stress measured in the specimen as described

σ_2 = the change of stress when the specimen was cut out (parting out stress)

The distribution of σ_2 is determined by strain measurements obtained during the parting out process of the test specimen from the shroud. The through-wall measurements for σ_1, σ_2, and σ_r are presented in Appendix F.

Content Deleted -
EPRI Proprietary Information

4.4 Analytical Determination of Residual Stresses in Core Shroud Welds

In parallel with the experimental determination of weld residual stresses of the core shrouds at River Bend and Grand Gulf Nuclear Stations, finite element analyses were performed by Dominion Engineering Inc. to analytically determine the weld residual stresses. The objective of this activity was to develop an analytical technique to complement the experimental residual stress distribution.

The analyses were performed using geometrical and weld procedure information for the spare core shroud at River Bend and a shroud mock-up fabricated by Tokyo Electric Power Company (TEPCO). The choice of the parameters of the River Bend shroud for analytical modeling is convenient because it offered the opportunity of comparing the results of the analytical evaluation with the experiment results discussed in the previous sections. For River Bend, the study focused on the circumferential welds H4, H5, H6a, and H6b, since the most significant cracking, in terms of extent and depth, has been reported to be in the HAZ of the circumferential welds. The circumferential H2 and H3 welds were analyzed for the TEPCO shroud mockup design.

The weld residual stress analyses were performed using the ANSYS finite element code [11]. The symmetrical nature of the shroud permitted an axisymmetric finite element model to be employed. for the analysis. Because of the relatively high temperatures associated with the welding process and the resulting high strains, a thermo-elasto-plastic analyses was performed utilizing temperature-dependent material properties.

Content Deleted -
EPRI Proprietary Information

The simulation of the welding process consisted of three stages.

Content Deleted -
EPRI Proprietary Information

Content Deleted -
EPRI Proprietary Information

To account for all the shroud welds under consideration, the analyses were performed on three separate finite models. One model was created for weld H3. One model was created for welds H4 and H5 since the weld preparations are essentially identical for these two welds. The third model included welds H6a and H6b since the effects of one of these welds on the other may not be negligible. A separate model was developed for welds H2 and H3 in the TEPCO shroud mock-up.

The results of the analyses for all the welds considered are shown in Appendix H (Figures H-9 through H-15). The results show the distribution of through-wall axial and hoop stresses at key locations of the weldments as well as contour plots.

Content Deleted -
EPRI Proprietary Information

Content Deleted -
EPRI Proprietary Information

4.5 Comparison Between Experimental and Analytical Results

In this section, the surface and through-wall residual stress measurement reported earlier are compared with the analytical prediction, with the objective of establishing the basis for recommendation of appropriate residual stress distributions for use in the crack growth evaluation for the various welds of the shroud. The first comparison made with the analytical predictions examined the surface measurements. This comparison is considered to be of relatively less importance since only the analytically-predicted stress at the surfaces are used. It should be realized that the measured surface stresses could be influenced by a number of factors, including the surface preparation such as grinding, and therefore may not provide very meaningful comparison from plant to plant. Figures H-9 through H-14 provide the comparison between the measured surface stresses and the analytical predictions.

Content Deleted -
EPRI Proprietary Information

The comparison of the experimental and analytically-predicted through-wall axial residual stress measurements are shown in Figures 4-4 through 4-6 for welds H5, H6a, and H6b, respectively.

Content Deleted -
EPRI Proprietary Information

4.6 Recommendation of Residual Stress Distribution for Analysis of Core Shroud Welds

For the purpose of providing generic recommendations for residual stress distribution for analysis of core shroud welds, the welds were grouped into two categories. The first category includes the shell-to-shell welds. These are the H4 and H5 welds. The experimental (both surface and through-wall) and analytical through-wall residual stress distributions discussed earlier for these welds are shown in Figure 4-7.

Content Deleted -
EPRI Proprietary Information

The second category of welds includes the shell-to-ring welds similar to the H2, H3, H6a, and H6b welds. The experimental, analytical, and recommended through-wall distributions for welds in this category are shown in Figures 4-8 through 4-10 for H2/H3, H6a and H6b ring welds, respectively.

The trend in the through-wall distribution for these welds is similar to the shell-to-shell welds. The recommended distribution previously presented for the shell-to-shell welds is also shown in Figures 4-8 through 4-10.

Content Deleted -
EPRI Proprietary Information

It is acknowledged in the recommendation provided herein, that the through-wall residual stress profiles at local regions of the shroud can be affected by several factors including fit-up stresses, weld joint geometries, welding parameters such as heat input, welding sequence, welding starts and stops, repairs, material properties and distortions of the shroud during installation.

Content Deleted -
EPRI Proprietary Information

4.7 Stress Relaxation Effects

The recommended residual stress distributions in the shroud welds did not take into account possible stress relaxation during service. There are two primary sources of residual stress relaxation. The first is attributable to neutron irradiation. This effect has been studied in Reference 12 for several stainless steels and nickel alloy materials. The results of this study, for stainless steel, are shown in Figure 4-12.

Content Deleted -
EPRI Proprietary Information

The second source of weld residual stress relaxation is due to temperature effects.

Content Deleted -
EPRI Proprietary Information

Table 4-1

Operating Stress for Plant A

Content Deleted -
EPRI Proprietary Information

Table 4-2

Operating Stress for Plant B

Content Deleted -
EPRI Proprietary Information

Table 4-3
Summary of Near Surface Residual Stress Measurements at Grand Gulf Nuclear Station

Content Deleted -
EPRI Proprietary Information

Table 4-3
Summary of Near Surface Residual Stress Measurements at Grand Gulf Nuclear Station
(concluded)

Content Deleted -
EPRI Proprietary Information

Table 4-4

Summary of Near Surface Residual Stress Measurements
at River Bend Nuclear Station

Content Deleted -
EPRI Proprietary Information

Table 4-5

Recommended Through-Wall Axial Residual Stress Distribution
for BWR Shroud Welds

Content Deleted -
EPRI Proprietary Information

Content Deleted -
EPRI Proprietary Information

Figure 4-1. NRC Accepted Axial Weld Residual Stress Distribution for Large Diameter Piping [3]

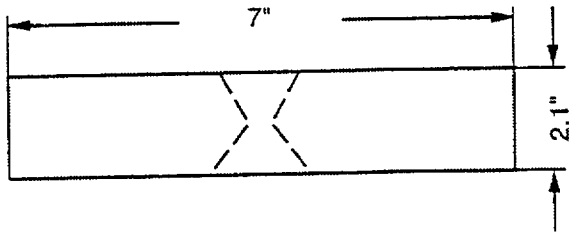

(Weld H5)

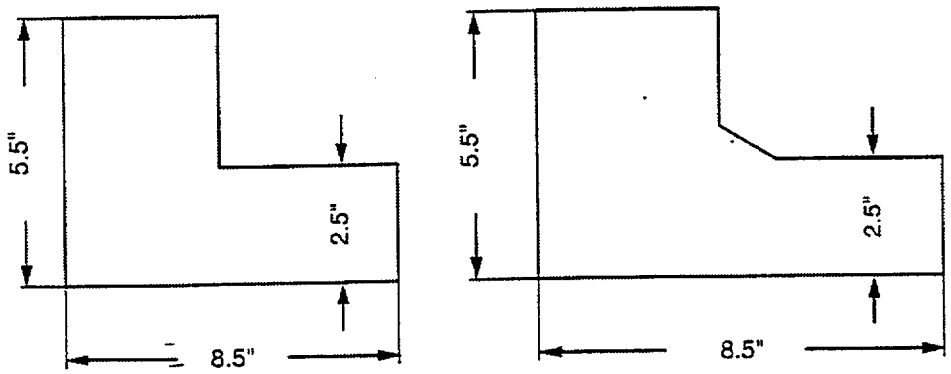

(Weld H6A and H6B)

Figure 4-2. Test Specimens for Through-Wall Residual Stress Measurements at River Bend Nuclear Station

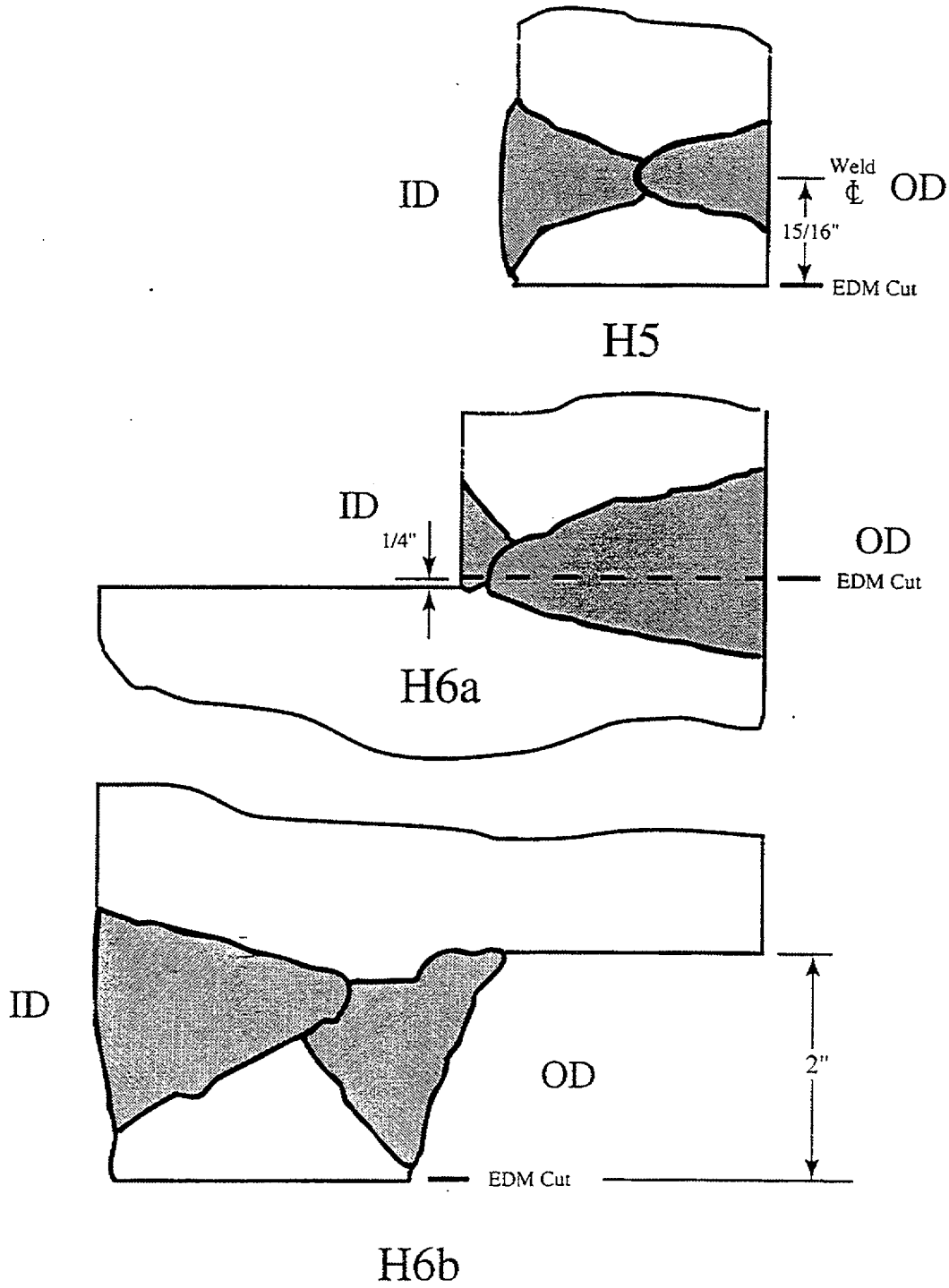

Figure 4-3. Weld Profiles and Planes for Through-Wall Weld Residual Stress Measurements at River Bend Nuclear Station

Shroud Weld H5 Axial Residual Stress in HAZ

Content Deleted -
EPRI Proprietary Information

Figure 4-4. Comparison of Experimental and Analytical Through-Wall Residual Stress Distribution for Weld H5

Shroud Weld H6a Axial Residual Stress
Through Weld Centerline

Content Deleted -
EPRI Proprietary Information

Figure 4-5. Comparison of Experimental and Analytical Through-Wall Residual Stress Distribution for Weld H6a

Shroud Weld H6b Axial Residual Stress
Through Ring Side HAZ

Content Deleted -
EPRI Proprietary Information

Figure 4-6. Comparison of Experimental and Analytical Through-Wall Residual Stress Distribution for Weld H6b

Analytical and Measured Axial Residual Stress
Shroud Welds H4/H5

Content Deleted -
EPRI Proprietary Information

Figure 4-7. Through-Wall Axial Residual Stress Distributions in HAZ for Shell-to-Shell Weld of Core Shroud (H4/H5) and Comparison with Recommended Curve

Analytical and Measured Axial Residual Stress Distributions
Shroud Welds H2/H3

Content Deleted -
EPRI Proprietary Information

Figure 4-8. Through-Wall Axial Residual Stress Distributions in HAZ for Core Shroud Shell-to-Ring Welds (H2/H3) and Comparison With Recommended Curve

Analytical and Measured Axial Residual Stress Distributions
Shroud Welds H6a

Content Deleted -
EPRI Proprietary Information

Figure 4-9. Through-Wall Axial Residual Stress Distribution in Weld for Core Shroud H6a Shell-to-Ring Welds and Comparison With Recommended Curve

Analytical and Measured Axial Residual Stress Distributions
Shroud Welds H6b

Content Deleted -
EPRI Proprietary Information

Figure 4-10. Through-wall Axial Residual Stress Distribution for Core Shroud H6b Shell-to-Ring Welds and Comparison With Recommended Curve

Measured Axial Residual Stress

Content Deleted -
EPRI Proprietary Information

Figure 4-11. Comparison of Experimental Measurements (Surface and Through-wall) With Recommended Curve

Effect of Irradiation on Stress Relaxation in Austenitic Materials

Content Deleted -
EPRI Proprietary Information

Figure 4-12. Stress Relaxation Due to Neutron Irradiation [12]

5.0 FRACTURE MECHANICS CONSIDERATIONS

A key parameter in the crack growth correlation developed in Section 3 for the core shroud horizontal welds is the stress intensity factor (K_I). In this section, the stress intensity factors for the operating stresses and the residual stresses discussed in Section 4 are developed to assist in the crack growth evaluation. Allowable flaw size determination for the shroud is also discussed. The crack growth evaluation and the allowable flaw size are used to determine the safe operating period of a flawed shroud.

5.1 Stress Intensity Factors Due to Applied Stresses

In general, the applied stresses consisting of dead weight, seismic and thermal loads are relatively small for the shroud as discussed in Section 4.1. As such, it will be conservatively assumed that these stresses are applied in pure tension. Several solutions for K_I have been provided in the literature for part-wall, part circumference flaws in cylinders.

Content Deleted -
EPRI Proprietary Information

Content Deleted -
EPRI Proprietary Information

5.2 Stress Intensity Factors Due to Weld Residual Stresses

Due to the non-uniform through-wall distribution of the weld residual stresses as shown in Section 4, a close form solution for K_I is not available for this case.

Content Deleted -
EPRI Proprietary Information

The above methodology was used to determine the K_I distribution for the recommended axial residual stress distributions presented in Figures 4-7 and 4-8 for BWR core shrouds. The K_I distribution resulting from the recommended axial residual stress distribution for both ID- and OD-initiated flaws is shown in Figure 5-3.

Content Deleted -
EPRI Proprietary Information

As discussed above, the fracture mechanics model used to obtain the K_I distribution for the weld residual stresses assumes a 360° flaw. There may be situations where this assumption may be overly conservative and some relief may be required to account for short flaws.

Content Deleted -
EPRI Proprietary Information

5.3 Effect of Localized Stresses on Stress Intensity Factor Distribution

As discussed in Section 4.6, for some localized regions of the shroud welds, the recommended axial residual stress may be non-conservative. This could therefore result in higher values of K_I in these regions compared to the recommended curve shown in Figure 5-4. It is possible that at these localized regions, the K_I distribution may stay entirely positive through-wall. This may result in localized regions having relatively high crack growth rates resulting in potentially through-wall cracks. However, as indicated in the discussion in Section 4.6, these localized regions of relatively high tensile weld residual stresses are necessarily compensated by other regions having high

components of compressive stresses due to equilibrium considerations. This compensating effect will result in lower K_I values and hence slower crack growth rates at these locations. This compensating phenomenon, therefore, lessens the possibility of having through-wall cracks around the entire circumference of the core shroud. Field experience has verified this concept. The K_I distribution shown in Figure 5-4 is expected to provide a very reasonable representation for the majority of the shroud weld locations and is recommended for use in our crack growth model.

As an illustration of the potential effect of the localized stresses discussed above, the result of superimposing a membrane stress of 10 ksi to account for the local effects is shown in Figure 5-5.

Content Deleted -
EPRI Proprietary Information

5.4 Allowable Flaw Size for BWR Shroud

As discussed earlier in this report, all existing BWR shrouds were fabricated from austenitic stainless steels. Several studies that have been performed to support the BWR pipe cracking problem have shown that stainless steels possess adequate toughness such that they fail in a ductile manner. As such, the net section plastic collapse principle, whereby the remaining ligament of the flawed pipe becomes fully plastic subsequent to failure, has been used as a failure mechanism in determining the allowable flaw sizes in ASME Code Section XI for austenitic stainless steels. It is expected that this should also be the case for the shroud welds which are remote from the highly irradiated regions.

Specific analyses that have been performed to support the evaluation of several flawed BWR shrouds using this methodology have shown that for the shroud welds which are not highly irradiated, the allowable flaw size even assuming a 360° circumferential flaw is at least 90% of the thickness of the

shroud [17]. This very favorable allowable flaw size is not surprising since the applied loads on the shroud are relatively small, as shown in Tables 3-1 and 3-2.

For the shroud welds in the high fluence region of the shroud (Weld H4), linear elastic fracture mechanics principles have typically been used to determine the allowable flaw size, since the toughness has been diminished slightly in this region due to irradiation. This approach is believed to be very conservative, for fluences at or below 1×10^{21} n/cm^2 (E>1MeV). Evaluations that have been performed on several BWR shrouds using this approach have shown that the allowable flaw size is at least 70% of the thickness of the shroud.

Table 5-1

Normalized Through-Wall Stress Intensity Factor Distribution
for BWR Shroud Welds

Content Deleted -
EPRI Proprietary Information

Content Deleted -
EPRI Proprietary Information

Figure 5-1. Parameter F_t to Describe Stress Intensity Factor K_I for the Part-Through-Wall, Part Circumference Flaws [15]

Content Deleted -
EPRI Proprietary Information

Figure 5-2. Magnification Factors for Circumferential Crack in Cylinder (t/R = 0.1) [16]

Recommended Normalized Stress Intensity Factor for BWR Core Shroud Welds

Content Deleted -
EPRI Proprietary Information

Figure 5-3. Recommended Normalized K_I Distribution for BWR Shroud Welds (ID and OD Initiated Flaws)

Factored K vs. a (360° = 1)

Part-Wall Circumferential Crack

Content Deleted -
EPRI Proprietary Information

Figure 5-4. Flaw Reduction Factors for Determination of K_I for Weld Residual Stresses in BWR Shrouds With Part-Circumference Flaws

Normalized Residual Stress Intensity Factor for BWR Core Shroud Welds (Including Local Effects)

Content Deleted -
EPRI Proprietary Information

Figure 5-5. Effect of Localized Membrane Stress on K_I Distribution for BWR Shroud Welds (ID and OD Initiated Flaws)

6.0 EVALUATION METHODOLOGY FOR CORE SHROUD CRACK GROWTH

The information developed in the prior three sections of this report is utilized in this section to illustrate the manner in which the crack growth data and correlation can be employed in a crack growth analysis of a typical BWR core shroud. Section 6.1 describes three alternative evaluation procedures for core shroud crack growth analysis. Section 6.2 provides an example illustrating the plant-specific evaluation procedure for a core shroud weld.

6.1 Evaluation Procedure

Three alternate approaches are proposed for the evaluation of crack growth in flawed BWR shrouds. Any of these approaches can be used in the evaluation. It is recognized that there are other models and other approaches available that can also be used to resolve the BWR shroud cracking issue especially with regards to sensitization and radiation effects.

If any of the three approaches described below provide the desired continued operating interval for the bounding flawed core shroud weld, the analysis is complete. If the result is unacceptable, the utility must take some action consistent with the BWRVIP guidelines, but which are outside the scope of this document.

6.1.1 Approach No. 1

Content Deleted -
EPRI Proprietary Information

6.1.2 Approach No. 2

Content Deleted -
EPRI Proprietary Information

6.1.3 Approach No. 3

Content Deleted -
EPRI Proprietary Information

6.2 Example of Plant-Specific Analysis

An analysis of a flawed core shroud weld using Approach No. 2 is presented in this section. More detailed examples of Approach No. 3 involving plant-specific analyses are provided in Appendix J. The analysis presented below, using Approach No. 2, illustrates the manner in which the crack growth correlation and the K-representation can be used to disposition a specific flaw in a core shroud. The ECP and conductivity presented in this example are conservative for BWR shroud evaluations. For

BWR plants operating under moderate HWC conditions, a lower ECP may be justified. The parameters used in this example are as follows:

Shroud Thickness:	1.5 inches
Flaw Characteristics:	10% through-wall by 90° around circumference on inside surface
Weld Type:	H5
Applied Stress:	2.22 ksi (from Table 4-1 Upset Condition)
Residual Stress:	Use Shell-to-Shell Distribution (Figure 4-7)
ECP:	200 mV(SHE)
Conductivity:	0.15 μS/cm

Content Deleted -
EPRI Proprietary Information

The crack growth correlation, represented by Equation 3-1 with the 95th percentile, is then employed to determine the crack growth with time through the wall.

Content Deleted -
EPRI Proprietary Information

Content Deleted -
EPRI Proprietary Information

Additional examples of the ability of the model to address core shroud crack growth is presented in Appendix J of this report. In this appendix, results of crack extension UT calculations for three plants (Brunswick, Chinshan, and KKM) are compared to the empirical model predictions.

Content Deleted -
EPRI Proprietary Information

Table 6-1

Results of Crack Growth Analysis for Example Problem

Content Deleted -
EPRI Proprietary Information

Table 6-1

(continued)

Content Deleted -
EPRI Proprietary Information

Table 6-1

(continued)

Content Deleted -
EPRI Proprietary Information

Table 6-1

(concluded)

Content Deleted -
EPRI Proprietary Information

ID Shell-to-Shell Connected Stress Intensity (t=1.5")

Content Deleted -
EPRI Proprietary Information

Figure 6-1. Through-Wall Stress Intensity Factor Distribution for Example Problem

Content Deleted -
EPRI Proprietary Information

Figure 6-2. Results of Crack Growth Analysis for Example Problem

7.0 SUMMARY AND CONCLUSIONS

The following provides a summary and conclusions of the work performed in this report to support the crack growth evaluation of flawed BWR shroud welds and other stainless steel internals.

- An empirical through-wall crack growth correlation has been developed in this report for use in the evaluation of BWR stainless steel internals, based on extensive crack growth data collected from several sources. The best-fit crack growth correlation is given as:

Content Deleted -
EPRI Proprietary Information

-

-

-
-

Content Deleted -
EPRI Proprietary Information

-
-

-
-
-
-
-

Content Deleted -
EPRI Proprietary Information

8.0 REFERENCES

1. Eason, E. D., and Nelson, E. E., "Correlations Between Grain Boundary Compositions and IASCC Susceptibility in Austenitic Stainless Steel," EPRI Report TR-103508, April 1994.

2. Eason, E. D., Wright J. E., and Nelson, E. E., "Multi-variable Modeling of Pressure Vessel and Piping J-R Data," NUREG/CR-5729, May 1991.

3. Hazelton, W. S., and Koo, W. H., "Technical Report on Material Selection and Processing Guidelines for BWR Coolant Pressure Boundary Piping," NUREG-0313, Revision 2, Nuclear Regulatory Commission, January 1988.

4. Ford, F. P., et al., "Corrosion-Assisted Cracking of Stainless and Low-Alloy Steels in LWR Environments," EPRI Report NP-5064, February 1987.

5. Gordon, B., and Horn, R., Personal Communication, September 1995.

6. Harris, D. O., Dedhia, D. D., Eason, E. D., and Patterson, S. D., "Probability of Failure in BWR Reactor Coolant Piping," NUREG/CR-4792, Vol. 3, December 1986, pp. 8-9.

7. USNRC Document NUREG-1061, Volume 1, "Report of the U.S. Nuclear Regulatory Commission Piping Review Committee - Investigation and Evaluation of Stress Corrosion Cracking in Piping of Boiling Water Reactor Plants," August 1984.

8. EPRI Document NP-1413, "Measurement of Residual Stresses in Type 304 Stainless Steel Piping Butt Weldments," June 1980.

9. EPRI Document NP-2662-LD, "Computational Residual Stress Analysis of Induction Heating of Welded BWR Pipes," December 1982.

10. ASTM Standard E837-94, "Determining Residual Stresses by the Hole-Drilling Strain Gage Method," American Society for Testing and Materials, Philadelphia, 1994.

11. ANSYS Finite Element Program, Version 5.1, Swanson Analysis System, Inc., 1994.

12. BWRVIP letter from Larry Nelson to Raj Pathania, "Stress Relaxation Due to Irradiation," November 10, 1995.

13. Sim, R. G., and Giannuzzi, A. J., "A Study of Stress Relaxation in AISI 304 Stainless Steel," General Electric Document NEDE 13334, April 1973.

14. Giannuzzi, A. J., "Studies on AISI Type 304 Stainless Steel Piping Weldments for Use in BWR Applications," EPRI Report No. NP-944, December 1978.

15. Zahoor, A., "Ductile Fracture Handbook," Volume II, EPRI Report No. NP-6301-D, June 1989.

16. Buchalet, C.B., and Bamford, W. H., "Stress Intensity Factor Solutions for Continuous Surface Flaws in Reactor Pressure Vessels," Mechanics of Crack Growth, ASTM STP S90, American Society for Testing and Materials, 1976, pp. 385-402.

17. USNRC, "Safety Evaluation by the Office of Nuclear Reactor Regulation Related to Core Shroud Cracking; Commonwealth Edison Company and Iowa-Illinois Gas and Electric Company; Dresden Nuclear Power Station, Unit 3; Quad Cities Nuclear Power Station Unit 1, Docket Nos. 50-249 and 50-254," July 21, 1994.

APPENDICES

APPENDIX A

Crack Growth Rate Data: ABB Atom and Argonne National Laboratories

Prepared by:

M. L. Pytel
A. J. Giannuzzi
N. G. Cofie
Structural Integrity Associates, Inc.

APPENDIX A
Crack Growth Rate Data

INTRODUCTION

The crack growth data presented in this appendix were obtained from ABB-Atom and Argonne National Laboratories. These sources were identified as having well documented austenitic stainless steel fracture mechanics SCC laboratory test data in high-purity water representative of typical BWR environments. Traceability of data, especially in the case of crack growth rate controlling parameters, are key requirements in establishing the relevance of the data. Table A-1 lists field names that identify the type of information required for each data point.

Stainless steel materials of interest include wrought Types 304, 304L, 316NG, 347 and cast steels of CF-3, CF-3M, CF-8, and CF-8M compositions. Material susceptibility to SCC is influenced by composition and processing. Heat-specific chemistry and specimen heat treatment data are desirable for completeness but parameters which measure the degree of sensitization are more desirable. Therefore, electrochemical potentiokinetic reactivation (EPR) measurements and ferrite content for forged and cast materials respectively assume a special importance that may become evident upon review of their effect on susceptibility to crack initiation and to crack growth.

Conductivity has been classified and is recognized as a key factor related to IGSCC in BWR environments [A-1,A-3,A-5]. Domestic BWRs routinely operate with conductivity near or below 0.1 μS/cm now that the deleterious nature of poor water quality is understood. CGR experiments with conductivity higher than the EPRI limit of 0.3 μS/cm are included in the principle database being compiled. Subsequent discrimination of CGR data points on the bases of ionic contributors or absolute level of conductivity are performed during the correlation and verification process to establish the influence of these variables on the IGSCC behavior of these structural materials in the BWR environment. At this point all apparently relevant data have been incorporated so that the IGSCC behavior can be substantiated on as large a data set as possible.

Electrochemical Corrosion Potential (ECP), influenced by oxidizing species, flow rate and material surface condition, is an additional important parameter for categorizing environmental effect. Unlike conductivity, potential has not been identified as a parameter to exclude any CGR data.

The observed cracking documented in this appendix resulted from loadings in the Mode I orientation principally by a constant Mode I stress state. It will be shown in subsequent sections of this report that one major contributor to core shroud cracking is fabrication residual stresses. Ideal experimental loading would reproduce this constant displacement stress state but in the interest of expediting data collection, many experiments were conducted by imposing a cyclic load on the mean stress. This type of testing is used to promote both cracking itself and to encourage these cracks to propagate with a uniform crack front. Data points where dynamic loading promoted corrosion fatigue cracking are included in the table for completeness, but were not necessarily incorporated into the crack propagation model. The data relevance was reviewed prior to inclusion or exclusion.

Table A-1. Stainless Steel Crack Propagation Database Field Names

General Information	Chemical Composition	Environment
Reference	Ni (wt%)	O_2 (ppb)
Material/Heat ID	Co (wt%)	H_2 (ppb)
Material	Cu (wt%)	CO_2 (ppm)
Heat Treatment	Ta (wt%)	H_2SO_4 (ppm)
Specimen ID	C (wt%)	HCl (ppm)
Test Number	Si (wt%)	SiO_2 (ppb)
Cracking Mode	Mn (wt%)	ZnO (ppb)
Load Ration (R)	P (wt%)	H_2CrO_4 (ppm)
Frequency (Hz)	S (wt%)	HF (ppb)
Mean Conductivity at 25 °C (μS/cm)	Cr (wt%)	
O_2 Concentration (ppb)	Mo (wt%)	
ECP (mV(SHE))	Fe (wt%)	
Crack Growth Rate (mm/s)	Ti (wt%)	
EPR (C/cm^2)	Nb (wt%)	
Ferrite level (%)	Al (wt%)	
	N (wt%)	

ABB-Atom

Laboratory studies were conducted and documented in several reports to determine the effects of water impurities on environmental cracking in stainless steel in simulated BWR water [A-1,A-2]. Both corrosion fatigue and constant load tests on compact tension specimens were performed in autoclaves arranged in a refreshed recirculation test loop. Because the focus of these experiments was on the effects of impurities, very good records were kept on water chemistry.

Three baseline environments were used to simulate normal BWR water (288°C, 200 ppb O_2, 10 ppb H_2) and two Hydrogen Water Chemistry conditions (288°C, 15 ppb O_2, 125 ppb H_2; 288°C, 5 ppb O_2, 125 ppb H_2). CGR data was collected for experiments made with and without impurity additions of 100 or 25 ppb sulfate, or 1 ppm carbon dioxide to the baseline environments. Nineteen distinct test environments were ultimately identified as being used.

Sensitized austenitic stainless steel of Types 304 and 316NG were tested as standard 25 mm compact tension (CT) specimens. EPR values associated with these specimens are 13 and 0.01 C/cm^2.

Both constant and active loading experiments were performed. Of the 170 experiments collected, 44 were run under constant load. Stress intensity values applied in constant load experiments ranged from 11 to 60 MPa$\sqrt{m}$. A large range of load ratios and frequency values were used in experiments with cyclic loading. All cyclic data were included and will be evaluated for relevance.

Table A-2 lists the data that were consolidated to reflect the ABB-Atom input data to be used in the CGR correlation work.

Argonne National Laboratory

As part of a large program to investigate environmentally-assisted cracking in light water reactors [A-3 - A-18], ANL investigated the crack growth of austenitic stainless steels in high-purity water. NUREG/CR-6176 "Review of Environmental Effects on Fatigue Crack Growth of Austenitic Stainless Steels" contains several tables taken from Appendix A of that report which documents 12 years of data collection that comprise the ANL Crack Growth Database for Wrought and Cast Austenitic Stainless Steels. Reference to the individual NUREG report where the data was originally reported is also provided in these tables. Materials included are Types 304, 316NG, 347, CF-3M, CF-3, CF-8M, and CF-8 in various heat treatment conditions.

The data obtained from this source is considered excellent in terms of completeness, relevance and traceability. Much of the data was obtained under dynamic, cyclic loading, or what the authors considered high-R (0.8-9.5) low-frequency (8×10^{-2} Hz) loading conditions. Maximum stress intensity values ranged from 18 to 72 MPa-m$^{1/2}$ with most of the tests performed at values around 30 MPa-m$^{1/2}$. Constant load tests were also performed and provide a basis for comparing the effects of active loading.

Exact oxygen concentrations were not reported for any particular 304 or 316NG CGR data points. Rather, sets of experiments were grouped as having approximately 200 ppb or 5-8 ppm oxygen. In the case of Type 347 and all cast materials experiments, specific O_2 concentrations were provided. The lack of O_2 content is of minor consequence since ECP is provided for each data point. The ECP was measured at the outlet of the autoclaves using A_g-A_gC1 reference electrodes. Conductivity for each data point is also provided. In cases where impurity was added, the concentration of that impurity is adequately provided.

The mode of cracking for each specimen is documented in the NUREG report where that particular experiment was first recorded. In general, all sensitized 304 SS specimens cracked intergranularly, 316NG SS cracked transgranularly, and the cast materials cracked transgranularly along ferrite austenite phase boundaries.

Table A-3 lists the data that was consolidated to form the ANL data set that was included in the CGR correlation work.

GE

General Electric has conducted extensive work on stainless steel crack propagation in BWR environments. Some GE data has been published in generalized CGR plots for evidence in support of the prediction of CGR using the PLEDGE model as provided in Appendix B of this report. Stainless steel CAVS data were provided to Modeling and Computing Services, Inc. in an electronic form and were included in the data set as provided in Appendix B.

Compilation of Database

Some of the data from the various sources was requested and provided in electronic form by the respective authors. The data that was not available in electronic form was typed, by hand, into a spreadsheet. The data was then compiled into a template with the files listed in Table A-1. The data, less any GE data, was then checked by comparing values and information from the original reports. The GE data has been validated by GE.

References

A-1 L. Ljungberg, "BWR Water Chemistry Impurity Studies, Volume 3: Fracture Mechanics Studies", EPRI NP-6773-SD, (March 1990).

A-2 L. Ljungberg, "BWR Water Chemistry Impurity Studies, Phase 2, Volume 2: Data Compilation", EPRI NP-7458-M, (September 1991).

A-3 W. E. Ruther, W. K. Soppet, and T. F. Kassner, Materials Science and Technology Division Light-Water-Reactor Safety Research Program: Quarterly Progress Report, October - December 1983, NUREG/CR-3689 Vol. IV, ANL-83-85 Vol. IV, pp. 75-87 (August 1984).

A-4 J. Y. Park and W. J. Shack, Light-Water-Reactor Safety Research Programs: Quarterly Progress Report, January - March 1985, NUREG/CR-4490 Vol. I, ANL-85-75 Vol. I, pp. 14-16 and 43-49 (March 1986).

A-5 W. E. Ruther, W. K. Soppet, J. Y. Park, and T. F. Kassner, Environmentally Assisted Cracking in Light Water Reactors: Semiannual Report, April - September 1986, NUREG/CR-4667 Vol. III, ANL-87-37 Vol. III, pp. 2-7 (September 1987).

A-6 W. E. Ruther, W. K. Soppet, J. Y. Park, and T. F. Kassner, Environmentally Assisted Cracking in Light Water Reactors: Semiannual Report, October 1986 - March 1987, NUREG/CR-4667 Vol. IV, ANL-87-41 Vol. IV, pp. 2-10 (December 1987).

A-7 W. E. Ruther, W. K. Soppet, J. Y. Park, and T. F. Kassner, Environmentally Assisted Cracking in Light Water Reactors: Semiannual Report, April - September 1987, NUREG/CR-4667 Vol. V, ANL-88-32 Vol. V, pp. 3-9 (February 1989).

A-8 W. E. Ruther, W. K. Soppet, J. Y. Park, and T. F. Kassner, Environmentally Assisted Cracking in Light Water Reactors: Semiannual Report, April - September 1988, NUREG/CR-4667 Vol. 7, ANL-89-40 Vol. V, pp. 3-14 (March 1990).

A-9 W. E. Ruther, J. Y. Park, T. F. Kassner, and W. K. Soppet, Environmentally Assisted Cracking in Light Water Reactors: Semiannual Report, October 1988 - March 1989, NUREG/CR-4667 Vol. 8, ANL-90/4, pp. 2-15 (June 1990).

A-10 W. E. Ruther, W. K. Soppet, and T. F. Kassner, Environmentally Assisted Cracking in Light Water Reactors: Semiannual Report, April - September 1991, NUREG/CR-4667 Vol. 13, ANL-92/6, pp. 16-19 (March 1992).

A-11 W. E. Ruther, W. K. Soppet, and T. F. Kassner, in Environmentally Assisted Cracking in Light Water Reactors: Annual Report, October 1983 - September 1984, NUREG/CR-4287 Vol. 13, ANL-85-33, pp. 110-113 (June 1985).

A-12 W. E. Ruther, W. K. Soppet, J. Y. Park, and T. F. Kassner, Environmentally Assisted Cracking in Light Water Reactors: Semiannual Report, October 1987 - March 1988, NUREG/CR-4667 Vol. VI, ANL-89/10, pp. 5-14 (August 1989).

A-13 W. E. Ruther, W. K. Soppet, and T. F. Kassner, Environmentally Assisted Cracking in Light Water Reactors: Semiannual Report, October 1990 - March 1991, NUREG/CR-4667 Vol. 12, ANL-91/24, pp. 22-30 (August 1991).

A-14 J. Y. Park, and W. K. Soppet, Environmentally Assisted Cracking in Light Water Reactors: Semiannual Report, April 1989 - September 1989, NUREG/CR-4667 Vol. 9, ANL-90/48, pp. 3-6 (March 1991).

A-15 J. Y. Park, and W. J. Shack, Light-Water-Reactor Safety Research Programs: Quarterly Progress Report, October - December 1984, NUREG/CR-3998 Vol. III, ANL-84-60 Vol. III, pp. 7-14 (October 1984).

A-16 W. E. Ruther, W. K. Soppet, J. Y. Park, and T. F. Kassner, Materials Science and Technology Division Light-Water-Reactor Safety Research Program: Quarterly Progress Report, April-June 1983, NUREG/CR-3689 Vol. II, ANL-83-85 Vol. II, pp. 44-48 (June 1984).

A-17 W. E. Ruther, O. K. Chopra, and T. F. Kassner, Environmentally Assisted Cracking in Light Water Reactors: Semiannual Report, October 1992 - March 1993, NUREG/CR-4667 Vol. 16, ANL-93/27, pp. 19-27 (September 1993).

A-18 J. Y. Park, Environmentally Assisted Cracking in Light Water Reactors: Semiannual Report, April - September 1992, NUREG/CR-4667 Vol. 15, ANL-93/2, pp. 13-20 (June 1993).

Table A-2

Content Deleted -
EPRI Proprietary Information

Table A-2 (continued)

Content Deleted -
EPRI Proprietary Information

Table A-2 (concluded)

Content Deleted -
EPRI Proprietary Information

Table A-3

Content Deleted -
EPRI Proprietary Information

Table A-3 (Continued)

Content Deleted -
EPRI Proprietary Information

Table A-3 (Continued)

Content Deleted -
EPRI Proprietary Information

Table A-3 (Concluded)

Content Deleted -
EPRI Proprietary Information

APPENDIX B

Crack Growth Rate Data: GE Nuclear Energy

Prepared by:

B. M. Gordon
R. M. Horn
General Electric Nuclear Energy

Appendix B

Crack Growth Rate Data: CAVS and Previous GE Nuclear Studies

November 7, 1995

Prepared for the BWRVIP Crack Growth Rate Committee

Prepared by: _____
B. M. Gordon

Prepared by: _____
R. M. Horn

Abstract

This Appendix contains a summary of the crack growth data that was derived from two different types of sources. The first source of data were the studies that were performed as part of the pipe cracking investigations and was use as the basis for the NRC disposition line. The data was re-assessed for the test conditions and the stated crack growth rate. The tests that were performed were largely performed by General Electric. The tests that were performed were conducted in one of two environments: 0.2 ppm oxygen and 6 ppm (referred to in the literature as 8 ppm due to the upper test specification limit) oxygen 288°C high purity BWR water. The tests were conducted at conductivity levels that are much higher than the conductivity levels associated with the current levels at operating plants. The data is useful to expand the range of the data used in the data correlation development. The tests that were run did not include any corrosion potential measurements. Therefore, the ECP were assigned based on the test environment. The ECP assigned was derived from a comparison of several ECP/water chemistry correlations. The ECP values that were assigned were 60 mV, SHE and 120 mV, SHE for the GE 0.2 ppm and 6 ppm tests.

The second, comprehensive data summary was developed by reviewing and assigning crack growth rates to the data from CAVS tests that were performed at actual operating plants. These tests were performed at Brunswick 1, Duane Arnold, Fitzpatrick, Hatch 1, Limerick, Nine Mile Point 1, Nuclenor, Pilgrim and Peach Bottom 2 and 3 over the time period of 1988 through 1993. These test systems included ECP measurements and are fully documented tests. The data provided was taken from data reports.

1

NRC Disposition Data

The data that has been used to support the NRC disposition line found in NUREG-0313 has been displayed in several different references (1, 2, 3). Figure 1-1 presents the curve along with the data points and the associated references. The data can be divided into two separate categories: that generated in high oxygen water, 6 ppm O_2 and that generated in normal water chemistry (NWC), 0.2 ppm O_2. The majority of the data presented is constant load data with some cyclic data also shown for comparison.

Content Deleted -
EPRI Proprietary Information

1.1 References

1. R. M. Horn, et al., "The Growth and Stability of Stress Corrosion Cracks in Large Diameter BWR Piping, Electric Power Research Institute, NP-2472, vol. 1,2, July 1982.

2. Section XI Task Group for Piping Flaw Evaluation, ASME Code, "Evaluation of Flaws in Austenitic Steel Piping, J. of Pressure Vessel Technology, vol . 108, p. 366, ASME, 1986.

3. W. S. Hazleton and W. H. Koo, "Technical Report on Material Selection and Processing Guidelines for BWR Coolant Pressure Boundary Piping", Final Report, NUREG-0313, rev. 2, July 1987.

1.1 References (Continued)

4. D. A. Hale, " Materials Performance in a Startup Environment, First Semiannual Progress Report, May 1981-January 1982, " NEDC-24392-1, April 1982.

5. M. T. Wang, unpublished results, GENE

6. H. D. Solomon, unpublished results, GE CR&D

7. I. Masaoki, unpublished results, Hitachi Research Lab

8. J. Y. Park and W. J. Shack, "Corrosion Studies in Nuclear Piping in BWR Environments,", Semiannual report, Electric Power Research Institute, (T117-1), July 1980.

9. R. D. Caligiuri, l. E. Eiselstein, and M. L. Fox, "Low Temperature Sensitization of Weld Heat Affected Zones in Type 304 Stainless Steel," IAAEA Meeting on Environmental Cracking, Freiburg, West Germany, May 1981.

Table B-1a. Environmental Conditions for Testing in Simulated Normal Water Chemistry (NWC) BWR Service Conditions

Content Deleted -
EPRI Proprietary Information

Table B-1b. Environmental Conditions for Testing in High Oxygen 288°C Water Environment

Content Deleted -
EPRI Proprietary Information

Table 1-2. Summary of Data Base for NRC Disposition Curve

Content Deleted -
EPRI Proprietary Information

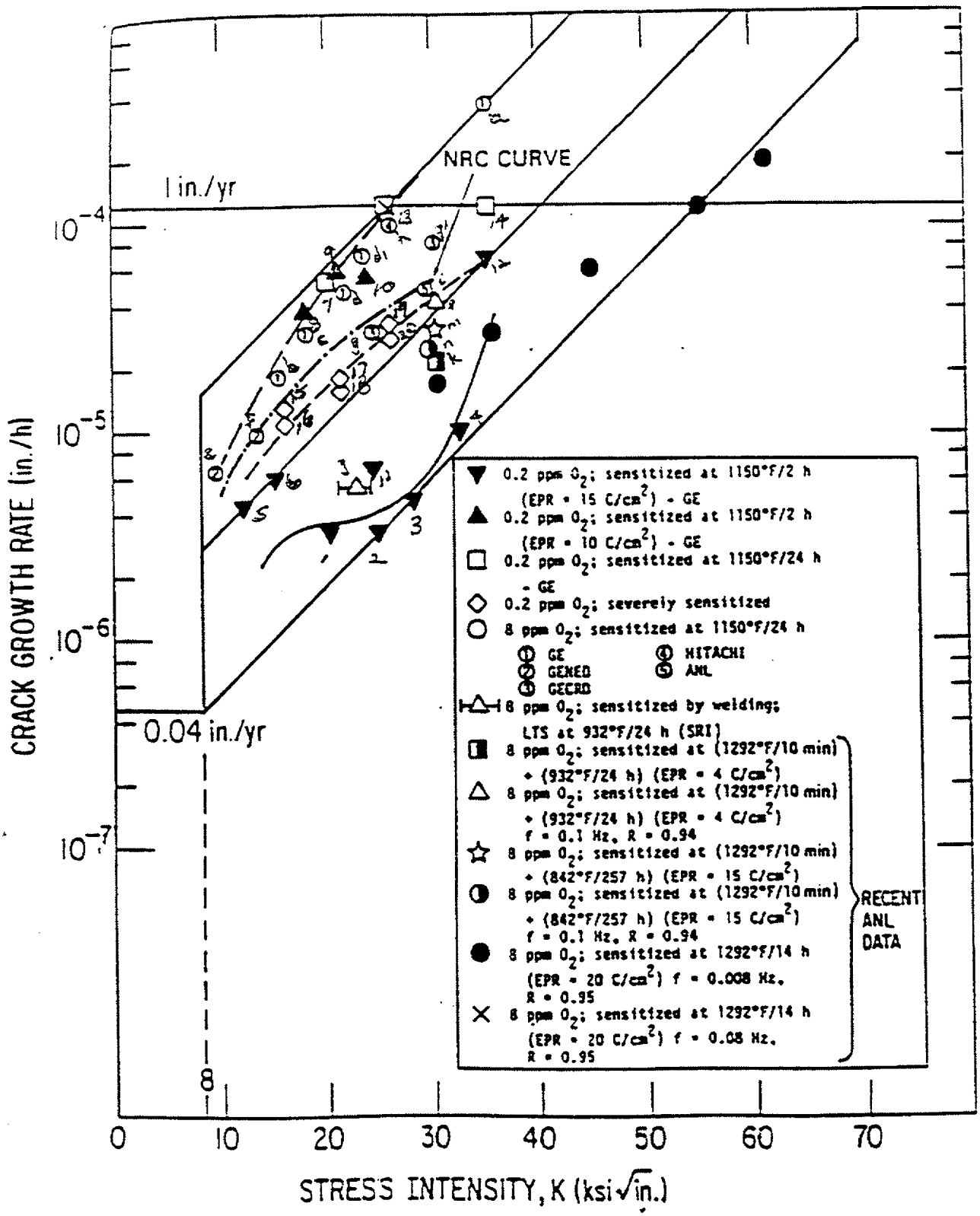

Figure 1-1. Crack Growth Rate Data

2

CAVS Crack Growth Data

Table 2-1 presents the readily available GE Nuclear Energy crack growth data obtained from compact tension (CT) and double cantilever beam (DCB) specimens of various heats of Type 304 stainless steel in various heat treated conditions. The table presents the following items in columns from left to right:

Content Deleted -
EPRI Proprietary Information

2.1 References

1. C. D. Frederickson, "Brunswick 1 CAV System Startup," SASR 91-42, May 1, 1991

2. C. D. Frederickson, "Status of Brunswick 2 CAV System," SASR 90-14, February 9, 1990

3. W. D. Miller and G. M. Gordon, "Duane Arnold HWC Program Results," PMWG-G-562, October 11, 1989

4. W. D. Miller, R. A. Head and M. E. Indig, "Measurement of In-core and Recirculation System Response to Hydrogen Water Chemistry at the Duane Arnold Energy Center," EPRI TR-102310, April 1993

5. L. L. H. King, "J. A. FitzPatrick Crack Arrest Verification (CAV) System, Progress Letter No. 1," SASR 88-92, March 12, 1988

6. D. A. Hale et al, "FitzPatrick Chemistry Evaluation First 1989 Report Period," 1989

7. D. E. Farmer et al, "FitzPatrick Chemistry Evaluation Second 1989 Report Period," 1989

8. J. E. Weber, "James A. FitzPatrick Nuclear Power Plant Crack Arrest Verification System, Report Period August 1989 - March 1990," SASR 90-94, 1990

9. R. A. Head and M. Siegler, "In-core Response to Hydrogen Water Chemistry at J. A. FitzPatrick Plant," January 1992

10. D. A. Hale, "Plant Hatch 1 Crack Arrest Verification (CAV) System Summary Report Fuel Cycle 13," SASR 91-147, September 1991

11. C. W. Jewett, "Effects of Dissolved Oxygen, Hydrogen and Water Purity on Crack Growth of Boiling Water Reactor Structural Alloys in High Temperature Water," NEDE-31618P, Class III, October 1988

12. D. A. Hale, "Limerick Unit 1 Crack Arrest Verification (CAV) System, Progress Letter No. 1" SASR 89-58, July 7, 1989

13. K. P. Dias, "Limerick Unit 1 Crack Arrest Verification (CAV) System, Progress Letter No. 5" SASR 91-28, May 1991

14. R. A. Head et al, "Nine Mile Point-1 Hydrogen Water Chemistry Final Report," PCRT, Transmittal 88-RAH07-31, August 1988

15. C. D. Frederickson, "Santa Maria de Garona Crack Arrest Verification System, Progress Letter No. 1" SASR 89-105, November 1989

2.1 References

16. D. A. Hale, J. L. Simpson and J. M. Skarpelos, "BWR Coolant Impurities Program at Peach Bottom Units 2 and 3," EPRI NP-7310-L, May 1991

17. D. A. Hale letter to G. M. Gordon, "Type 316L Stainless Steel, Summary of PB-3 Performance," WPPSLTR2.WP, March 19, 1990

18. A. E. Pickett, "Pilgrim Nuclear Power Station Crack Arrest Verification System, Progress Letter No. 2" SASR 90-64, June 1990

Table 2-1 GENE BWR and Laboratory T-304 Stainless Steel CT and DCB Crack Growth Data

Content Deleted -
EPRI Proprietary Information

Table 2-1 GENE BWR and Laboratory T-304 Stainless Steel CT and DCB Crack Growth Data (Continued)

Content Deleted -
EPRI Proprietary Information

Table 2-1 GENE BWR and Laboratory T-304 Stainless Steel CT and DCB Crack Growth Data (Continued)

Content Deleted -
EPRI Proprietary Information

Table 2-1 GENE BWR and Laboratory T-304 Stainless Steel CT and DCB Crack Growth Data (Continued)

Content Deleted -
EPRI Proprietary Information

Table 2-1 GENE BWR and Laboratory T-304 Stainless Steel CT and DCB Crack Growth Data (Continued)

Content Deleted -
EPRI Proprietary Information

Table 2-1 GENE BWR and Laboratory T-304 Stainless Steel CT and DCB Crack Growth Data (Continued)

Content Deleted -
EPRI Proprietary Information

APPENDIX C

Crack Growth Rate Correlation

Prepared by:

E. D. Eason
A. A. Merton
Modeling and Computing Services

MCS 951001

APPENDIX C

DEVELOPMENT OF AN EMPIRICALLY-BASED STAINLESS STEEL CRACK GROWTH RATE CORRELATION

E. D. Eason
Principal Investigator

A. A. Merton

Prepared by
Modeling & Computing Services
6400 Lookout Road, Suite #105
Boulder, CO 80301-3377

November 1995

INTRODUCTION

Purpose of this Investigation

The purpose of this investigation is to analyze the stainless steel stress corrosion crack (SCC) propagation data that are currently available from environments representative of modern BWR water chemistry. The desired result is a model of the form:

$$\frac{da}{dt} = C\ K^n \qquad \text{(C-1)}$$

where C and possibly n depend on electrochemical potential, conductivity, and other variables as appropriate. Static SCC tests using pre-cracked specimens are the primary focus. The variables considered in the analysis are as shown in Table C-1.

Table C-1: Variables Considered	
Response Variable:	Crack growth rate (mm/s)
Loading Variables:	Stress intensity, K (MPa$\sqrt{m}$) Frequency (Hz), R-ratio
Metallurgical Variables:	Heat, Heat Treatment EPR sensitization (C/cm^2)
Type of Material:	304, 316L, 316NG
Environment Variables:	Temperature (°C), Conductivity (µS/cm), ECP (mV_{SHE})

Database Description

A database of laboratory data was compiled by Structural Integrity Associates (SIA), as documented in Section 2 of this report and Appendix A. A second database was

independently developed at GE Nuclear Energy, including GE laboratory and in-plant CAVS data, as discussed in Section 2 and Appendix B. The values which were tabulated in these databases were used directly by M&CS.

Nearly half of the data are CAVS data provided by GE. These data are particularly important because they are directly representative of actual plant water chemistry conditions. The tests were conducted in autoclaves that were attached directly to various locations in the reactor coolant loop. In-core data were also available from GE, from near-beltline regions of the core. However, these data were not included in the analysis reported here because (1) they are irradiated and the fluence was not available, and (2) they are wedge-loaded DCB specimens and all of the others are actively loaded CT specimens. There is presently considerable uncertainty as to the exact mechanism(s) that are responsible for irradiation-assisted stress corrosion cracking (IASCC), but it is known that fluence is an important variable for correlating IASCC[1].

Some CAVS specimens were listed with a comment in the database, such as start-up, beginning of hydrogen injection, hot standby, etc. These short-term transient conditions are not representative of the long duration, steady operating conditions. Consequently these specimens were not used in the analysis.

A relatively large subset of laboratory data was excluded because of cyclic loading. Even though some of the frequencies were relatively low, preliminary pattern recognition results showed higher crack growth rates for the cyclic data, increasing as the frequency increases. The purpose of the present work was to develop a correlation for stress corrosion cracking, i.e. static load; consequently only static load data were used in the calibration.

Modifications to Data Base for Analysis

In setting up the data base for analysis, the objective was to include all variables for which the observations were reasonably complete. Many potential variables could not be used because values were missing for many of the specimens. For instance, the

chemical composition variables were missing in many cases. The most important chemical elements are probably carbon and molybdenum (if Types 316 and 304 data are combined). In principle, these variables could be determined and added to the data set. In order to meet the time scale, a good alternative approach was taken: Type 304 and 316 data were separately analyzed, EPR sensitization was considered (which reflects both carbon content and heat treatment), and the heats were identified in the analysis by a categorical variable.

Unfortunately, the EPR measurements were not available for all of the specimens. M&CS estimated EPR where necessary based on the heat identifiers and heat treatment details that were provided in the database.

Content Deleted -
EPRI Proprietary Information

M&CS also filled in temperatures for a number of the CAVS data based on temperature-time traces in available detailed reports. GE (Barry Gordon) also filled in additional temperature estimates during the course of the analysis. Temperature in the CAVS autoclaves does vary, so the intent was to choose representative temperatures over the period of time during which the CAVS specimens were on test. Minor temperature variations were ignored in this process.

ANALYSIS APPROACH

Transformation Analysis

A primary tool used for this study is TAC (Transformation Analysis Code), a powerful computer code for multivariable modeling that has been used in several prior M&CS

projects.[1,2] The purpose of TAC is to identify key variables and the optimal form of functions to use for multivariable surface-fitting. Unlike traditional approaches, where modeling forms are assumed and then force-fitted to the data (e.g. linear or polynomial regression), TAC uses the data directly to show the analyst what form of model is needed. TAC identifies the numerically-defined transformations E(Y) and $G_j(X_j)$ such that:

$$E(Y) = \sum_{j=1}^{n} G_j(X_j) \tag{C-2}$$

The transformations are not chosen in advance, but are calculated by the code and displayed graphically. The form specified by Equation C-2 is reasonably general, capable of representing any function of a sum of arbitrary nonlinear functions, products of arbitrary functions, etc.

TAC requires as input the raw data in a matrix format, with one row for each observation, one column for each variable. The independent variables X_j can be either continuous or categorical. Typical categorical variables might be different heats of material, different laboratories, or different investigators when correlating data from multiple sources.

The output from TAC is in graphical form, including plots of E(Y) *vs* Y and each $G_j(X_j)$ vs. X_j. The plots are presented in nondimensional form with the vertical axis in standard deviation units of Y, so that it is easy to identify the variables that account for most of the variation in response values. A screening version of TAC has also been developed (TACMVS) for checking for inadvertent correlations among "independent" variables and for identifying the most important variables.

Model Calibration

The primary method of model calibration was non-linear least squares, using the code SURFIT. SURFIT implements a non-linear least squares algorithm based on the methods of M.J.D. Powell. It is particularly convenient for calibrating engineering models.

SURFIT has been used in many engineering modeling projects over the past 20 years by the principal investigator, and has been successfully benchmarked against many other least squares codes based on the methods of Marquardt and Fletcher and the recent orthogonal distance regression code (ODR) from NIST.

An iterative process is used for calibrating the models as shown in Figure C-1. Beginning with the database development, which in this case was done by SIA and GE, the first step is the pattern recognition and transformation analysis described above. Then preliminary modeling functions are devised that have the appropriate shape based on the transformation analysis results. These are calibrated by least squares and then the quality of fit is assessed by statistical and graphical means. The quality of fit assessment often results in identification of outliers, changes in the database and an additional analysis cycle, as happened in the present analysis. The original database was analyzed, producing preliminary results, which led to an expansion of the database and the deletion of certain sets that proved to be outliers (such as the irradiated in-core data). Then a second cycle of pattern recognition and model calibration was performed, producing the final models presented here.

RESULTS

Correlations Among "Independent" Variables

The first analysis step is to analyze whether the assumed "independent" variables are truly independent. In engineering databases some variables are often inadvertently correlated with other variables. Figure C-2 shows the results of the analysis of independence, where the correlation coefficient R^2 has the usual meaning (0 implies no correlation, ±1 implies perfect correlation). Solid lines indicate strong correlations, as are

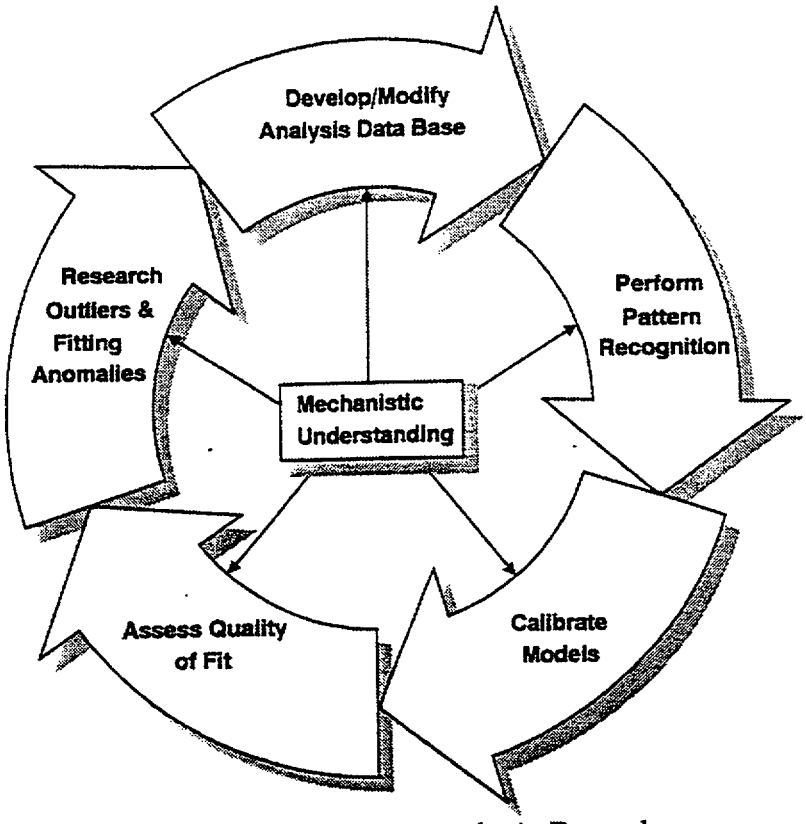

Figure C-1: Iterative Analysis Procedure

Content Deleted -
EPRI Proprietary Information

Figure C-2: Correlations Among Variables

Content Deleted -
EPRI Proprietary Information

The presence of correlations among supposedly independent variables, as shown in Figure C-2, greatly complicates the analysis. These correlations must be kept in mind when choosing modeling variables, because effects that show up in one particular variable may in fact be a combination of effects involving other variables. In addition, the fitting parameters for functions of correlated variables are often not well determined numerically.

Summary of Final TAC Runs

Table C-2 summarizes the results of the TAC runs on Type 304 material data.

Content Deleted -
EPRI Proprietary Information

Table C-2: Relative Effects of Variables

Content Deleted -
EPRI Proprietary Information

Correlation Models

For purposes of developing the correlation given here, only those observations with measured values of conductivity were used for model calibration. This prevented the use of older data points that were used in the NUREG/CR-0313 rev. 2 document, because conductivity and ECP could only be estimated for those points.

The best fit model for the 304 data is:

Content Deleted -
EPRI Proprietary Information

Content Deleted -
EPRI Proprietary Information

Figure C-3: Overall Quality of Model

Content Deleted -
EPRI Proprietary Information

When fitting Equation C-3, specimens that exhibit no SCC (runouts) were included. The fitting process was modified so that if the upper bound on da/dt from the runout is greater than the model estimate, there is no contribution to the sum of squares. If the model estimate is higher than the upper bound da/dt from the runout, the squared difference is included in the sum of squares. This sort of one-sided fitting process makes use of the one-sided estimates provided by runout data. The runouts are indicated by open circles and/or arrows in the following plots.

The agreement between the data and the model given by Equation C-3 can be evaluated graphically by examining normalized plots, in which the data points are adjusted as well as possible to a set of common conditions (assuming that the models correctly reflect the effect of each variable). The equation for this adjustment is:

Content Deleted -
EPRI Proprietary Information

Referring to the normalized plots for the best fit model, Figures C-4 through C-7, there is reasonable agreement between the data used for calibration and the model when all are adjusted as nearly as possible to common conditions.

Content Deleted -
EPRI Proprietary Information

Figure C-7 shows how the best fit model (solid line) compares with the NUREG/CR-0313 rev. 2 line (long dash) when plotted at the normalizing conditions given above. The short dashed line is an estimate of the 95th percentile of the residuals about the model, assuming they are log-normally distributed. The short dashed line is plotted at +1.645 standard deviations above the model (a factor of 10.3 on da/dt).

Content Deleted -
EPRI Proprietary Information

Content Deleted -
EPRI Proprietary Information

Figure C-4: Effect of Conductivity

Content Deleted -
EPRI Proprietary Information

Figure C-5: Effect of ECP

Content Deleted -
EPRI Proprietary Information

Figure C-6: Effect of Temperature

Content Deleted -
EPRI Proprietary Information

Figure C-7: Effect of K

DISCUSSION

Adequacy of Database

The database on sensitized Type 304 Stainless Steel, tested for SCC in representative environments, has 122 useable observations. In an earlier stage of this analysis, the database had 95 observations. Useful clues about the adequacy of the database can be found in the changes in results that occurred as the size of the database was increased by 28%. Most of the increase was from additional CAVS data, so that the current database is more biased toward actual field environments than the previous one. A major difference is the exclusion of in-core, irradiated specimens in the current calibration set.

Content Deleted -
EPRI Proprietary Information

Many of the variable effect trends identified by TAC are similar between the 95 and 122 observation sets, and the same variables were found to be important.

Content Deleted -
EPRI Proprietary Information

Content Deleted -
EPRI Proprietary Information

Variable Effects

Conductivity.

Content Deleted -
EPRI Proprietary Information

Figure C-8: Data with Addition of Sulfate, Chloride and CO_2

Stress Intensity Factor, K.

Content Deleted -
EPRI Proprietary Information

Temperature.

Content Deleted -
EPRI Proprietary Information

Electrochemical Potential, ECP.

Content Deleted -
EPRI Proprietary Information

Electrochemical Potentiokinetic Reactivation, EPR.

Content Deleted -
EPRI Proprietary Information

Content Deleted -
EPRI Proprietary Information

Fluence

Content Deleted -
EPRI Proprietary Information

Content Deleted -
EPRI Proprietary Information

Figure C-9: Data from Irradiated Material - (A) Annealed, (S) Sensitized

Comparison of Model with Subsets of Data

The models developed in this project were calibrated to a subset of homogeneous data that was complete in all of the important variables. In this subsection these models are compared to other subsets of data that were not used for model calibration. The first of these subsets is the set of data previously used to calibrate the curve in NUREG/CR-0313 Rev. 2. Both normal water chemistry conditions (nominally 200 ppb oxygen, assumed to be 60 mV_{SHE}, 0.5 µS/cm) and high oxygen conditions (nominally 6 ppm, assumed to be 120 mV_{SHE}, 1.0 µS/cm) were considered. The assumed ECP and conductivity were provided by GE (see Appendix B). Both of these data sets are shown with the present model and 95th percentile at estimated levels of ECP and conductivity in Figure C-10.

Content Deleted -
EPRI Proprietary Information

Figure C-10: NUREG/CR-0313 Rev. 2 Data *vs* Type 304 Model

Content Deleted -
EPRI Proprietary Information

Another interesting comparison is between Type 316 and other stainless steel data and the current model, as shown in Figure C-11.

Content Deleted -
EPRI Proprietary Information

Figure C-11: Other Stainless Steels *vs* Type 304 Model

Content Deleted -
EPRI Proprietary Information

Content Deleted -
EPRI Proprietary Information

Figure C-12: Type 304 at frequency, $f = 2 \times 10^{-4}$ Hz

Content Deleted -
EPRI Proprietary Information

Content Deleted -
EPRI Proprietary Information

Figure C-13: Type 304 at frequency, $f = 2 \times 10^{-3}$ Hz

Content Deleted -
EPRI Proprietary Information

Figure C-14: Type 316 at frequency, $f = 2 \times 10^{-4}$ Hz

Content Deleted -
EPRI Proprietary Information

Figure C-15: Type 316 at frequency, $f = 2 \times 10^{-3}$ Hz

Correlation Between C and n in Equation C-1

When power-law functions are fitted, as in Equation C-1, the coefficient C and exponent n are often correlated. The PLEDGE code[3] makes use of this correlation, estimating the slope of the log(da/dt) vs log(strain rate) line (and by implication, the value of the exponent on K) from the independent variables and then calculating the power law coefficient as a linear function of that slope. There is some evidence of a linear dependence of lnC on n (or vice versa) in the current study in the few sets where two or more K levels were tested for the same heat and environment. Thus an alternative model was calibrated in which lnC is estimated from the independent variables and then n is calculated from lnC. The result is:

Content Deleted -
EPRI Proprietary Information

Content Deleted -
EPRI Proprietary Information

Range of Applicability

The model was developed over the range of data listed below in Table C-3. Not all combinations of variables were represented in the database even within these ranges. Because the model describes the available data over these ranges, it is recommended to apply the model only within these limits. Great caution must be taken when applying the model outside these limits; however, the model should serve as a first order approximation for data which fall just outside these limits. The database consisting of 122 data points used to develop the model is shown in Table C-4.

Table C-3: Range of Calibration Data

Content Deleted -
EPRI Proprietary Information

Table C-4
Database Used for Model Development

Content Deleted -
EPRI Proprietary Information

Table C-4
(concluded)

Content Deleted -
EPRI Proprietary Information

CONCLUSIONS

This study has produced empirical crack growth rate correlations for sensitized Type 304 stainless steel and several conclusions regarding the database.

-

-

-

Content Deleted -
EPRI Proprietary Information

-

-

ACKNOWLEDGMENTS

The assistance of SIA and GE personnel, particularly Martin Pytel, Barry Gordon and Ron Horn, and the comments of Tony Giannuzzi (SIA) and Raj Pathania (EPRI) are greatly appreciated. This work was performed under subcontract to SIA.

REFERENCES

1. Eason, E.D. and Nelson, E.E., "Correlations Between Grain Boundary Compositions and IASCC Susceptibility in Austenitic Stainless Steel," EPRI Report TR-103508, April 1994.

2. Eason, E.D., Wright J.E. and Nelson, E.E., "Multivariable Modeling of Pressure Vessel and Piping J-R Data," NUREG/CR-5729, May 1991.

3. Ford, F.P. et al., "Corrosion-Assisted Cracking of Stainless and Low-Alloy Steels in LWR Environments," EPRI Report NP-5064, February 1987.

4. Gordon, B. and Horn, R., Personal Communication, September,1995.

5. Harris, D.O., Dedhia, D.D., Eason, E.D. and Patterson, S.D., "Probability of Failure in BWR Reactor Coolant Piping," NUREG/CR-4792, Vol.3, December 1986, pp 8,9.

6. Bruemmer, S.M. and Simonen, E.P., "Radiation Hardening and Radiation-Induced Chromium Depletion Effects on Intergranular Stress Corrosion Cracking of Austinitic Stainless Steels", Paper # 616, NACE Corrosion 93, (October 1992).

7. Jenssen, A. and Ljungberg, L.G., "Irradiation Assisted Stress Corrosion Cracking. Post Irradiation CERT Tests of Stainless Steels in a BWR Test Loops", Proceedings 7th International Symposium on Environmental Degradation of Materials in Nuclear Power Systems - Water Reactors, August 1995, pp 1043-1054.

8. Tsukada, T., Mywa, Y., and Nakajima, H., "Stress Corrosion Cracking of Neutron Irradiated Type 304 Stainless Steels", Proceedings 7th International Symposium on Environmental Degradation of Materials in Nuclear Power Systems - Water Reactors, August 1995, pp 1009-1019.

9. Eason, E.D. and Nelson, E.E., "Multivariable Analysis of IASCC Data," unpublished MCS Report 950201, June 1995.

10. Andresen, P.L., "Irradiation-Assisted Stress Corrosion Cracking", Stress Corrosion Cracking: Materials Performance and Evaluation, R. Jones ed, ASM, 1992, pp 181-210.

11. Hide, K., Dohi, K., Mayuzumi, M., Onchi, T., and Saitoh, M., Personal Communication, March 1994.

APPENDIX D

River Bend Shroud Material Properties

Prepared by:

J. Brihmadesam
Entergy Operations, Inc.

APPENDIX D

River Bend Shroud Material Properties

MATERIAL PROPERTY EVALUATION OF ENTERGY OPERATIONS, INCORPORATED BWR CORE SHROUD MATERIALS FROM GRAND GULF NUCLEAR STATION - UNIT 2 AND RIVER BEND STATION - UNIT 2

R. A. Keck for

PREPARED BY: J.S. Brihmadesam DATE: 11-3-95
J. S. Brihmadesam
ENGINEERING PROGRAMS

REVIEWED BY: J. W. Chism DATE: 11/3/95
J. W. Chism
ENGINEERING PROGRAMS

APPROVED BY: J R Hamilton DATE: 11-3-95
J. R. Hamilton
MANAGER, ENGINEERING PROGRAMS

Central Design Engineering
Entergy Operations, Inc.
Jackson, MS 39213

TABLE OF CONTENTS

SECTION	TITLE	PAGE NO.
	List of Tables	3
	List of Figures	4
D.1	Introduction	5
D.2	Testing of Shroud Materials	5
D.3	Results of Tests	6

LIST OF TABLES

TABLE NO.	TITLE	PAGE NO.
D-I	Mechanical Properties of Entergy Core Shroud Materials	8
D-II	River Bend Weld H6B Microhardness	9
D-III	River Bend Weld H6A Microhardness	10
D-IV	River Bend Weld H5 Microhardness	11
D-V	Grand Gulf Weld H5 Microhardness	12
D-VI	Grand Gulf Weld V5 Microhardness	13

LIST OF FIGURES

FIGURE NO.	FIGURE TITLE	PAGE NO.
D-1	RBS Core Shroud Specimen Layout	14
D-2	GGNS Core Shroud Specimen Layout	14
D-3	Typical Locations for Microhardness Tests	15
D-4	Strength Properties of Entergy Core Shroud Materials	16
D-5	Ductility Properties of Entergy Core Shroud Materials	17
D-6	RBS Weld H6B	18
D-7	RBS Weld H6A	19
D-8	RBS Weld H5	20
D-9	GGNS Weld H5	21
D-10	GGNS Weld V5	22

D.1 INTRODUCTION

Entergy Operations, Incorporated (Entergy) owns two unused shrouds from the canceled Unit 2 projects at the Grand Gulf Nuclear Station (GGNS) and at the River Bend Station (RBS). Entergy management made these spare shrouds available to the Boiling Water Reactor Vessel Internals Project (BWRVIP) for the purpose of conducting evaluations necessary for the proper and comprehensive resolution of the core shroud cracking issue. Entergy's direct contribution to the effort of the shroud crack growth project include:

- Provision of all site related support for the in situ near surface residual stress calculations by Sandia National Laboratories at GGNS (Appendix G) and by EPRI-RRAC at RBS (Appendix E).
- Abrasive Water Jet Cutting of portions of both shrouds for further testing and evaluation.
- Preparation of accurately machined samples from the GGNS shroud cut out for through thickness residual stress measurements by Neutron Diffraction at the Oak Ridge National Laboratories (ORNL).
- Mechanical Testing of samples from the two shroud cut outs (GGNS & RBS) to corroborate and verify the mechanical properties utilized in the analytical evaluation of the welds for residual stresses (Appendix H) using finite element methods.

The objective of the work presented in this Appendix was to determine the mechanical properties of BWR Core shroud materials (weld and base metal). In addition, macrometallography of the welds and microhardness testing were performed.

D.2 TESTING OF SHROUD MATERIALS

D.2.1 Sample Location and Removal

Location of specimens for mechanical testing (Tensile tests) at various temperatures from the two shroud cut outs are presented in Figures D-1 and D-2. The weld samples were taken in the circumferential direction in order to maintain an all weld metal morphology in the specimens. Also, the base metal specimens from the RBS shroud were in the same (circumferential) orientation as the weld metal specimens. Only one base metal specimen from the GGNS shroud cut out could be obtained for this effort. The location of the GGNS specimen is shown in Figure D-2.

In addition to the mechanical testing specimens, all the welds from RBS and the H5 circumferential weld and the vertical weld from GGNS were removed for microhardness testing with macrometallography.

D.2.2 Mechanical Testing

Tension testing was performed at various temperatures from room temperature (70°F) to 800°F. The purpose of this testing was to determine the material property behavior at elevated temperatures. The testing was performed on a Instron testing machine with a temperature controlled chamber. Strain measurements up to 30% strain were recorded with a digitally controlled extensometer. After this strain value, an effective strain from the cross-head displacement was plotted until failure. All tests and recording of data were performed in accordance with ASTM E-21. The strain rates utilized were 0.005 in/in/minute up to yield and after yield the displacement was limited to 0.15 in/minute. The elevated temperature tests commenced after a 30 minute soak at temperature and with a temperature control accuracy of ± 5°F.

D.2.3 Metallography and Microhardness

Specimens for this evaluation were prepared by conventional metallographic methods. The polished specimens were etched with 10% oxalic acid electrolytic etch. The etched specimens were then subjected to microhardness testing at various locations. The microhardness testing (Vickors 10kg load) was performed at 25 different locations in accordance with ASTM E-92 as shown in Figure D-3. However, it should be noted that for the H5 weld sample from RBS, the location of the Outside Diameter (OD) and the Inside Diameter (ID) were accidentally reversed during the microhardness testing. The microhardness data locations for RBS weld H5 shown in Table D-IV have been reversed from the original test data table to correct this problem.

D.3 RESULTS OF TESTS

D.3.1 Tension Testing

The results from the tension testing at various temperatures for both the base metal and the weld metal are presented in Table D-Ia (base metal) and Table D-Ib (weld metal). These results are also graphically presented in Figure D-4a for the base metal and Figure D-4b for the weld metal. Figures D-5a & D-5b show the ductility properties (Elongation and Reduction of Area) for the base metal and the weld metal, respectively.

D.3.2 Metallography and Microhardness Testing

The macrophotographs showing the various welds are presented in Figures D-6 through D-10. Weld details for these figures are as follows:

Figure D-6: RBS Weld H6B - OD welded first, followed by ID weld.

Figure D-7: RBS Weld H6A - ID welded first, followed by OD weld.
Figure D-8: RBS Weld H5 - ID welded first, followed by OD weld.
Figure D-9: GGNS Weld H5 - OD welded first, followed by ID weld.
Figure D-10: GGNS Weld V5 (Vertical) - ID welded first, followed by OD weld.

In each of the photomacrographs, the microhardness indentions can be observed.

The microhardness data from tests at room temperature for each weld is presented in Tables D-II through D-VI. The data presented in these tables show that the weld metal is slightly harder than the base metal as is borne out by the tension test results. In addition, there does not appear to be significant differences in hardness properties between the shroud materials from GGNS and RBS.

TABLE D-I: Mechanical Properties of Entergy Core Shroud Materials

Content Deleted -
EPRI Proprietary Information

TABLE D-II: River Bend Weld H6B Microhardness

Content Deleted -
EPRI Proprietary Information

TABLE D-III: River Bend Weld H6A Microhardness

Content Deleted -
EPRI Proprietary Information

TABLE D-IV: River Bend Weld H5 Microhardness
(Note: The location column of this table has been reversed relative to the other microhardness tables.)

Content Deleted -
EPRI Proprietary Information

TABLE D-V: Grand Gulf Weld H5 Microhardness

Content Deleted -
EPRI Proprietary Information

TABLE D-VI: Grand Gulf Weld V5 Microhardness

Content Deleted -
EPRI Proprietary Information

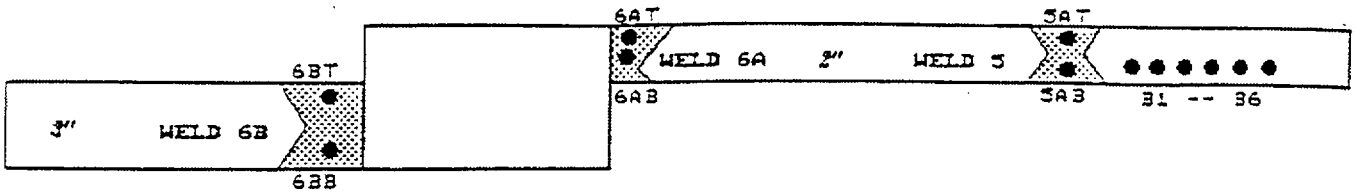

Figure D-1: RBS Core Shroud Specimen Layout
Schematic plot of the core shroud cut out from the River Bend Station - Unit 2.
The location of the samples are noted

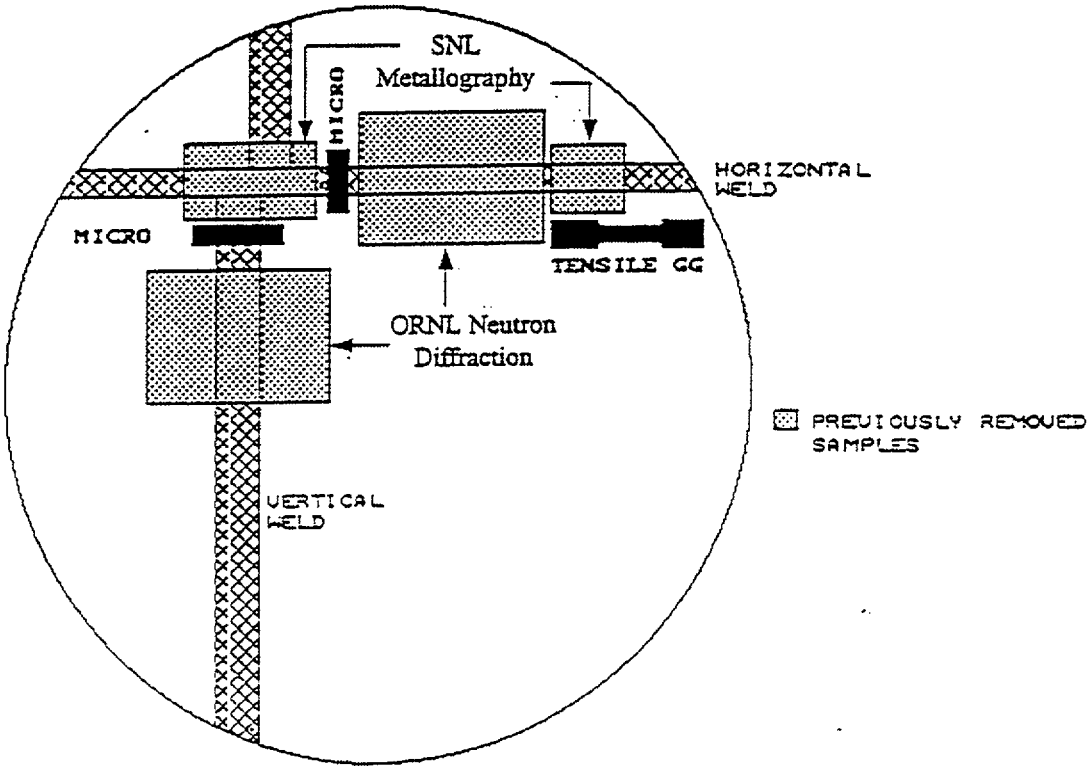

Figure D-2: GGNS Core Shroud Specimen Layout
Schematic plot of the core shroud cut out from the Grand Gulf Station - Unit 2.
The location of the samples are noted.

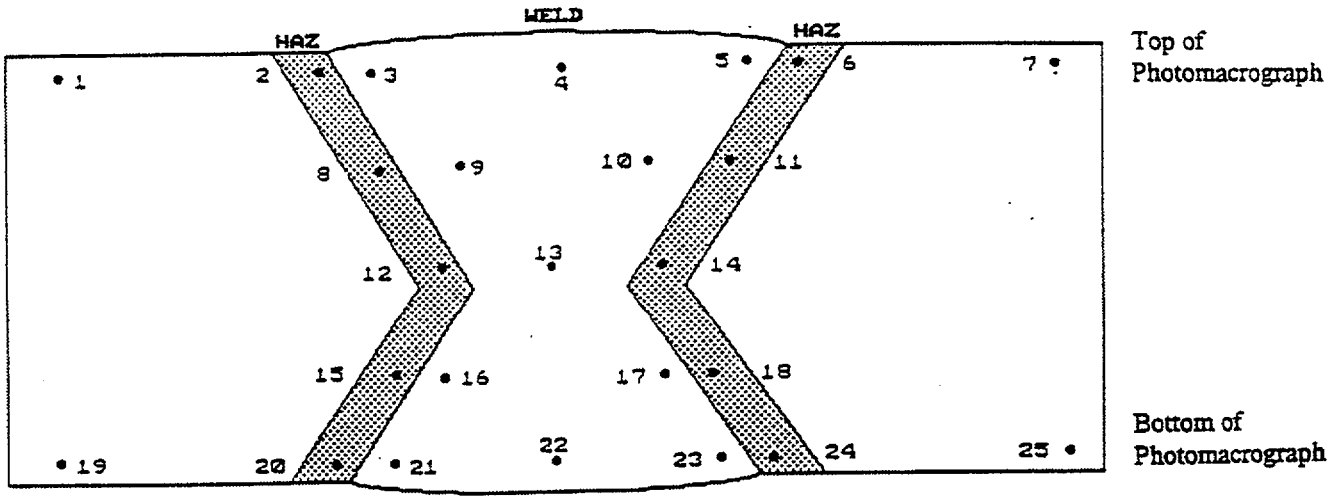

Figure D-3: Typical Locations for Microhardness Tests

Figure D-4: Strength Properties of Entergy Core Shroud Materials

Content Deleted -
EPRI Proprietary Information

Figure D-5: Ductility Properties of Entergy Core Shroud Materials

Content Deleted -
EPRI Proprietary Information

Content Deleted -
EPRI Proprietary Information

Figure D-6: RBS Weld H6B
Mag.: 1.1X Etchant: 10% Oxalic Acid, Electrolytic
Photomacrograph of microhardness sample from River Bend Weld 6B.

Content Deleted -
EPRI Proprietary Information

Figure D-7: RBS Weld H6A
Mag.: 1.1X Etchant: 10% Oxalic Acid, Electrolytic
Photomacrograph of microhardness sample from River Bend Weld 6A.

Content Deleted -
EPRI Proprietary Information

Figure D-8: RBS Weld H5
Mag.: 1.1X Etchant: 10% Oxalic Acid, Electrolytic
Photomacrograph of microhardness sample from River Bend Weld H5.
(Note: OD and ID locations on this figure have been reversed with respect to the other figures.)

Content Deleted -
EPRI Proprietary Information

Figure D-9: GGNS Weld H5
Mag.: 1.2X Etchant: 10% Oxalic Acid, Electrolytic
Photomacrograph of microhardness sample from Grand Gulf Weld H5.

Content Deleted -
EPRI Proprietary Information

Figure D-10: GGNS Weld V5
Mag.: 1.1X Etchant: 10% Oxalic Acid, Electrolytic
Photomacrograph of microhardness sample from Grand Gulf Vertical Seam Weld V5.

Content Deleted -
EPRI Proprietary Information

Figure H-9
TEPCO H2/H3 Weld Residual Stresses
Analytical Results vs. Measurements
Revised 10/4/95

Content Deleted -
EPRI Proprietary Information

Figure H-10
River Bend H3 Weld Residual Stresses
Analytical Results vs. Measurements
Revised 10/4/95

Content Deleted -
EPRI Proprietary Information

Figure H-11
River Bend H4 Weld Residual Stresses
Analytical Results vs. Measurements
Revised 10/4/95

Content Deleted -
EPRI Proprietary Information

Figure H-12
River Bend H5 Weld Residual Stresses
Analytical Results vs. Measurements
Revised 10/4/95

Content Deleted -
EPRI Proprietary Information

Figure H-13
River Bend H6a/H6b Weld Residual Stresses
Analytical Results vs. Measurements
Revised 10/9/95

Content Deleted -
EPRI Proprietary Information

Figure H-14
River Bend H5 Weld
Axial Stress During Crack Growth
Analytical Predictions
Revised 10/4/95

Content Deleted -
EPRI Proprietary Information

Figure H-15
Axial Stress Through the Thickness
Analysis vs. Measurements
Revised 10/12/95

APPENDIX E

Near Surface Residual Stress Measurements at River Bend Nuclear Station

Prepared by:

A. Peterson
EPRI Repair and Replacement Center

Residual Stress Measurements of a Core Shroud at the River Bend Nuclear Station

September 28, 1995

Prepared for:
Electric Power Research Institute

1.0 Introduction

Past experience has shown that intergranular stress corrosion cracking (IGSCC) has attacked the weldments of a number of Boiling Water Reactor (BWR) recirculation loop piping systems, requiring either repair of the welds or piping replacement. Recent inspections have found indications of cracking on the stainless steel core shroud at least two plants. IGSCC is the result of three primary factors; material susceptibility, aggressive environment and tensile residual stresses. High tensile residual stresses, whether induced by the original fabrication process or by welding, can be a major cause of stress corrosion cracking.

Concerns over the potential for crack initiation/propagation on the surface of the core shroud have prompted EPRI to investigate the residual stresses in the circumferential weldments of an unused shroud. The sample to be examined is located at the River Bend Nuclear Station. This shroud was to be used for Unit 2, which was cancelled, and the shroud was mothballed prior to installation.

Two segments of this testing were investigated by EPRI's Repair and Replacement Applications Center. The first phase involved cutting out a portion of the shroud and monitoring the relieved strain via bonded electrical resistance strain gages. The second phase was to determine the surface residual stresses of the circumferential weldments using a semi-destructive called "blind hole drilling".

Complementary testing is being conducted at Grand Gulf, UC - Berkeley and Sandia National Labs.

2.0 Crack Compliance Specimen

A section was removed from the main body of the shroud for evaluation of a new destructive technique developed at the University of California at Berkeley. Two samples were to be taken from the shroud and sent to UC - Berkeley for examination. The two coupons were to contain the H5 weld and the H6 welds.

The severed piece was parted out of the remainder of the shroud via water jet cutting. This process employed high pressure water for propulsion and a fine grit powder as the cutting media. Using the water jet insteal of plasma arc cutting allowed for a fairly smooth edge finish without inducing excessive heat build-up. This was necessary for the protection of the strain gages.

The strain gages were mounted axially and circumferentially to the sample prior to cutting and centered on the outside surface of the H5 weld. The location of the gages was chosen based on the position of an intersecting vertical weld. The vertical weldment extended from the H6A weld up to H5. These vertical welds are staggered throughout the shroud and should offer the points of highest stress.

A carbon steel plate was tack welded to the shroud to allow the magnetically mounted track a means of support. The water jet's arm assembly was set to make a perimeter cut around the plate extending 3 inches past each edge.

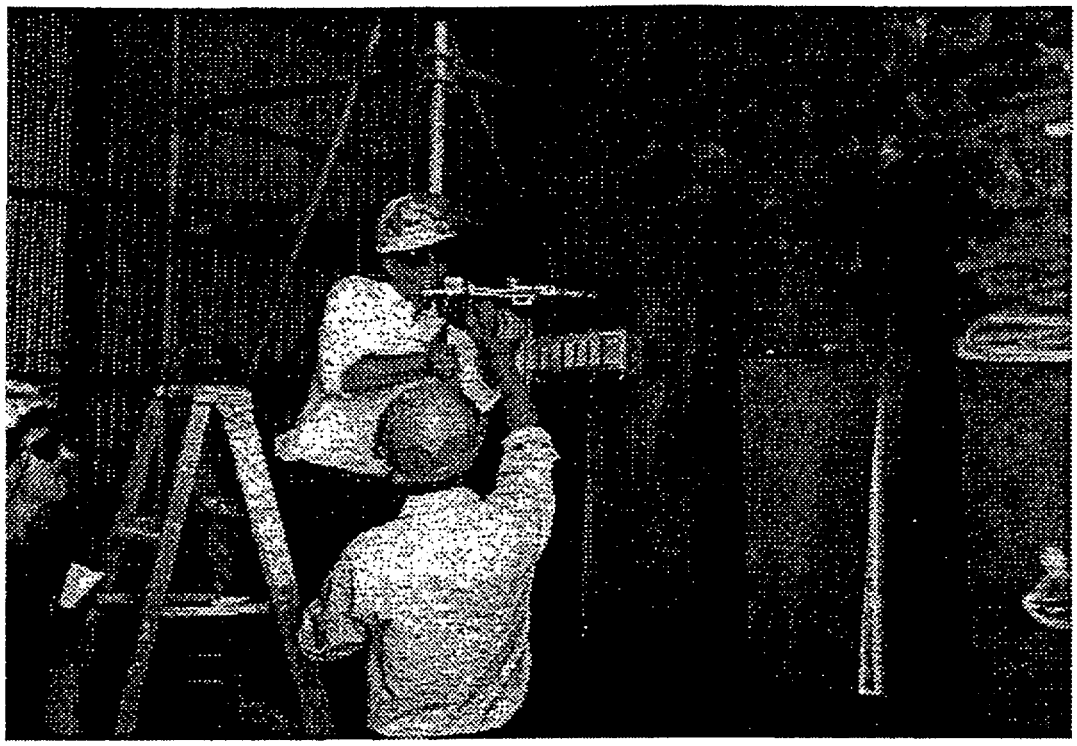

Water Jet Torch Alignment

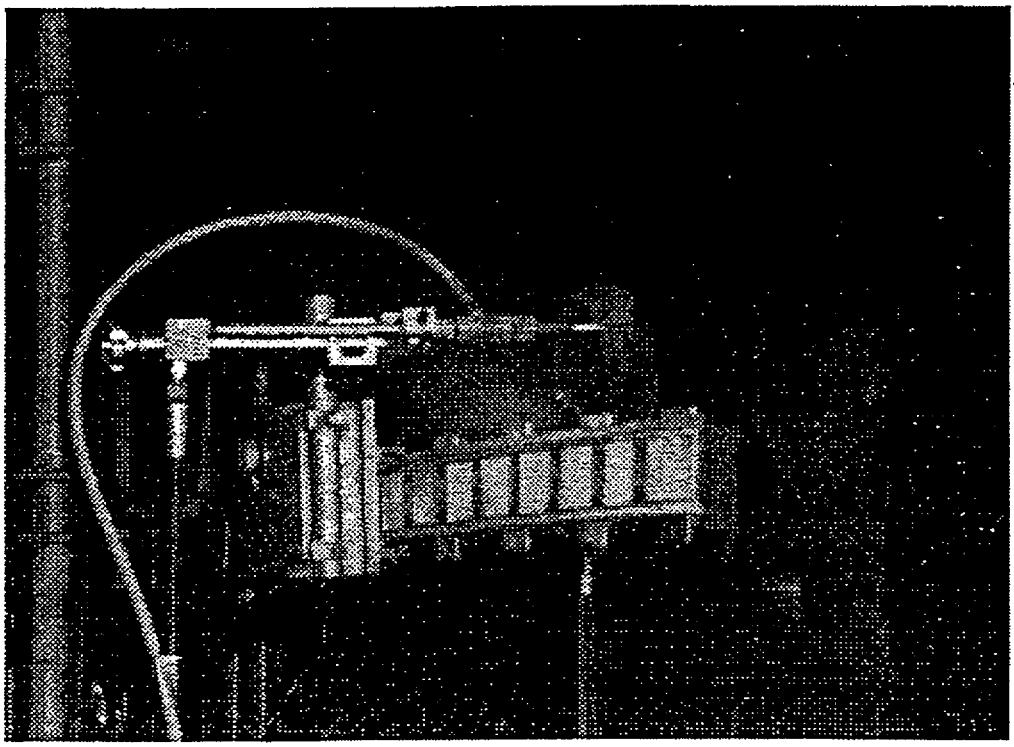

Water Jet Cutting

After removing the coupon from the shroud, the sample was shipped to the RRAC facility for additional cutting. The component was saw cut to a manageable size for shipment to UC-Berkeley. Each cut relieved some residual strain in the weld, and was monitored for total strain relaxation. The table and figure below, illustrate the amount of strain relieved from each cutting operation.

Content Deleted -
EPRI Proprietary Information

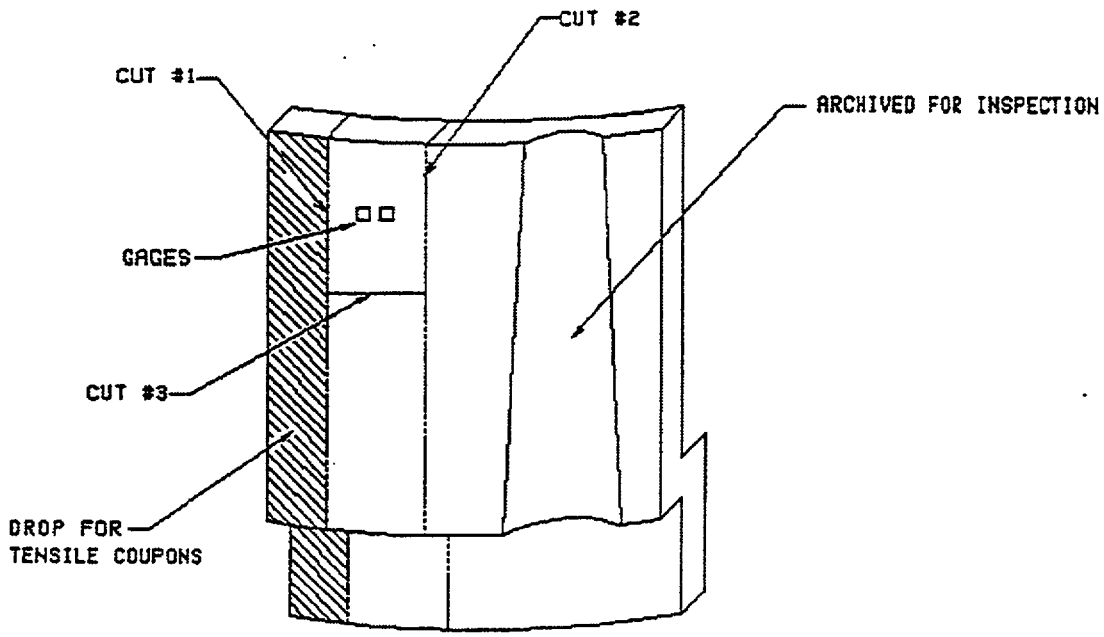

Coupon Removed From Core Shroud

3.0 Hole Drilling

An experimental technique was employed to obtain quantitative information regarding relative stresses of the various weldments. The experimental technique utilized electrical resistance strain gages and a blind hole drilling technique described in ASTM-E837. This technique, in brief, is performed as follows:

- Prepare the surface area of interest, removing minimal material.

- Epoxy the strain gage rosette to the substrate.
- Calibrate the rosette output to zero strain.
- Drill a hole through the center of the rosette using a low stress technique.
- Read the change in strain caused by metal relaxation.

Principal stresses can then be calculated based on the change in strain.

The procedures used for the strain gage application are outlined by Measurements Group Inc. in their Technical Bulletins and were used consistently throughout the project. The drilling was done with a high speed "dentist drill" as opposed to using the air abrasive method. This method provided greater speed and required less preparation and cleanup. Previous "round robin" studies performed at the EPRI NDE Center have shown that more consistent results are obtained with the drill technique..

It was necessary to develop some means of ensuring proper alignment of the drill in relation to the rosette when working within the full sized component. The drill must be centered over the rosette and it also must be perpendicular to the rosette. This prevents "drilling under" one gage element and influencing the response of that element more than other gage elements. This requirement was accomplished by implementing an optical alignment system utilizing a LASER to ensure the requisite perpendicularities.

The LASER is first positioned into the drilling fixture and illuminated. The incident beam that strikes the rosette is reflected back at some angle. The reflected beam then strikes the surface of the LASER fixture. While observing this reflected beam, adjustments can be made to the fixture until the incident and reflected beams are in alignment. This procedure is repeated until perpendicularity is assured.

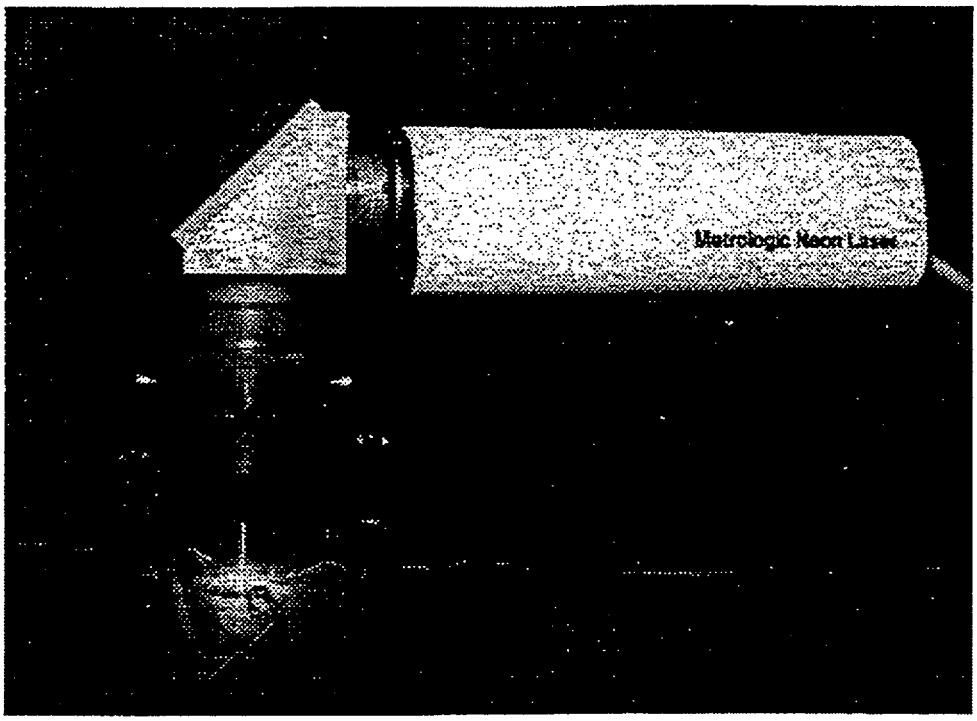

Drill Fixture With Laser

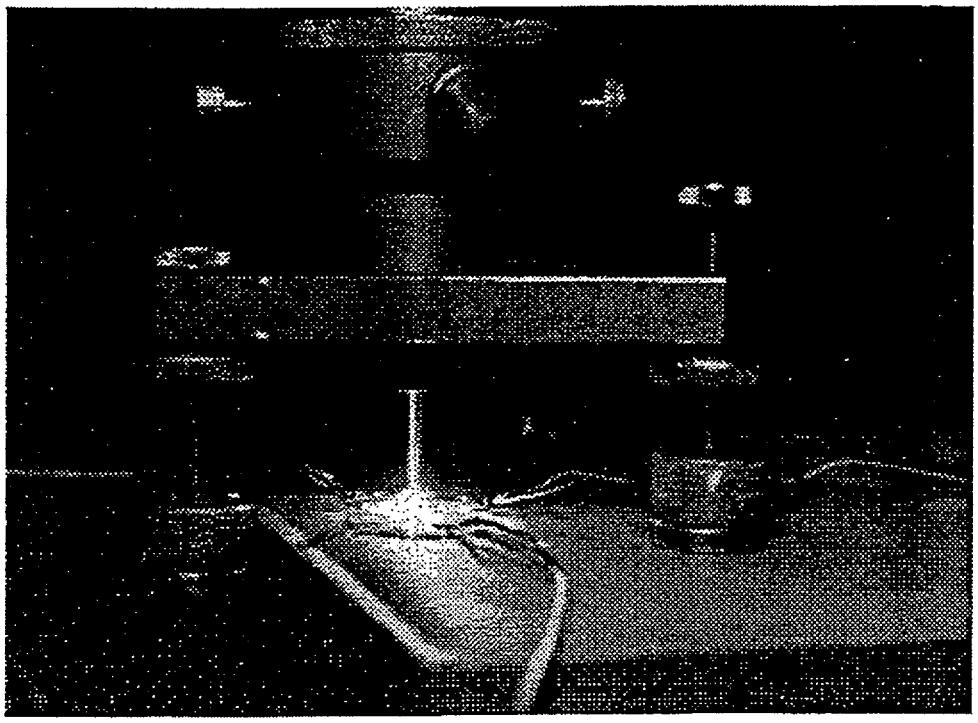

Reflected Laser Beam Indicating Improper Alignment

The strain measurements were made by first zeroing the gages in order to establish a known reference point, then drilling through the center of the rosette and measuring the relaxation strain. Strain readings were taken at consistent depth intervals and continued until the strain readings stabilized. This insured that a direct correlation could be made among all rosettes and gages. The drilling continued to a consistent depth of 0.090 inches. Additional drilling was not required since the relief of surface strain values stabilized at a drilled depth of about 0.060 to 0.075 inches.

3.1 Measurement Locations

The shroud was stored in an upright position at the River Bend warehouse facilities. This actually increases the difficulty in working with blind hole drilling equipment as the drill typically operates by gravity feed. Drilling horizontally was accomplished by attaching elastic bands to the stationary drill fixture and the drill column. This provided a constant tension on the drill, pulling it into the wall of the shroud. Hole depth is controlled by standard graduated feed screws.

The points of interest were the circumferential welds identified as H3, H4, H5, H6A & H6B. The location for the actual placement of the gages was chosen based on the area removed for the crack compliance specimen. The measurements were made 180° away from the hole starting several inches above H5 and extending below H6B. Measurements made at the H3, H4 & H5 were done without special fixturing. Measurements made at H6A & H6B locations required shims for positioning of the drill directly over the rosette.

Measurements were made at the intersection of the circumferential and vertical welds in all locations except H6B. These locations should have the greatest residual stress.

3.2 Residual Stress Results

Typical weldments produce high tensile stress and subsequently, plastic deformation. During normal fabrication, these tensile stresses cannot be prevented without some external mitigating process. Recognizing that high tensile stress is prevalent, quantifying the stress for comparison to historical service life data is imperative.

The tables below list the principal residual stresses measured in the circumferential welds. Since the shroud has not been used in service, dynamic cycling loads have not been an influence.

1/4 Inch Above Weld Fusion Line

Inside Surface Principal Stress (ksi) Outside Surface Principal Stress (ksi)

Content Deleted -
EPRI Proprietary Information

Weld Centerline

Inside Surface Principal Stress (ksi) Outside Surface Principal Stress (ksi)

Content Deleted -
EPRI Proprietary Information

1/4 Inch Below Weld Fusion Line

Inside Surface Principal Stress (ksi) Outside Surface Principal Stress (ksi)

Content Deleted -
EPRI Proprietary Information

Axial and Hoop Stresses

1/4 Inch Above Weld Fusion Line

Inside Surface Stress (ksi) Outside Surface Stress (ksi)

Content Deleted -
EPRI Proprietary Information

Weld Centerline

Inside Surface Stress (ksi) Outside Surface Stress (ksi)

Content Deleted -
EPRI Proprietary Information

1/4 Inch Below Weld Fusion Line

Inside Surface Stress (ksi) Outside Surface Stress (ksi)

Content Deleted -
EPRI Proprietary Information

Content Deleted -
EPRI Proprietary Information

4.0 Metallography

Samples of welds H5, H6A and H6B were cut from the compliance piece to provide metallographic coupons. These coupons were polished and etched with 1-2-3 etchant prior to hardness testing. After acid etching, bead placement is clearly shown. The effect of partially welding the joint from one side then back-gouging to clean filler metal explains the sequence in which the weld was completed. The joint configurations show a double "V" weld prep to allow for full penetration of weld metal.

The following graphics and tables illustrate the locations of hardness measurements. All hardness values are reported in Vickers values. The third impression on each scan sequence represents the hardness of the weld fusion line. Subsequent impressions were then made at increments of 1mm moving away from the WFL in both directions.

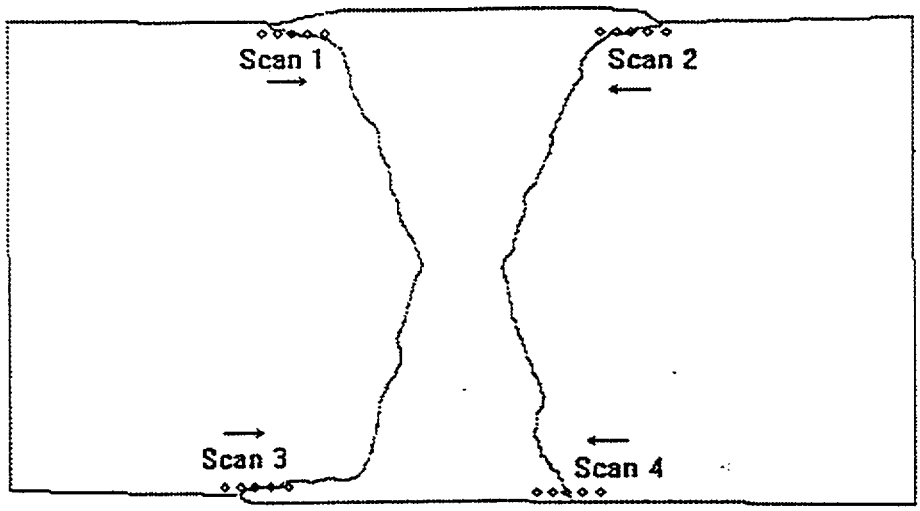

Weld H5

Impression #	Scan 1	Scan 2	Scan 3	Scan 4

Content Deleted -
EPRI Proprietary Information

Cross Section of Weld H5

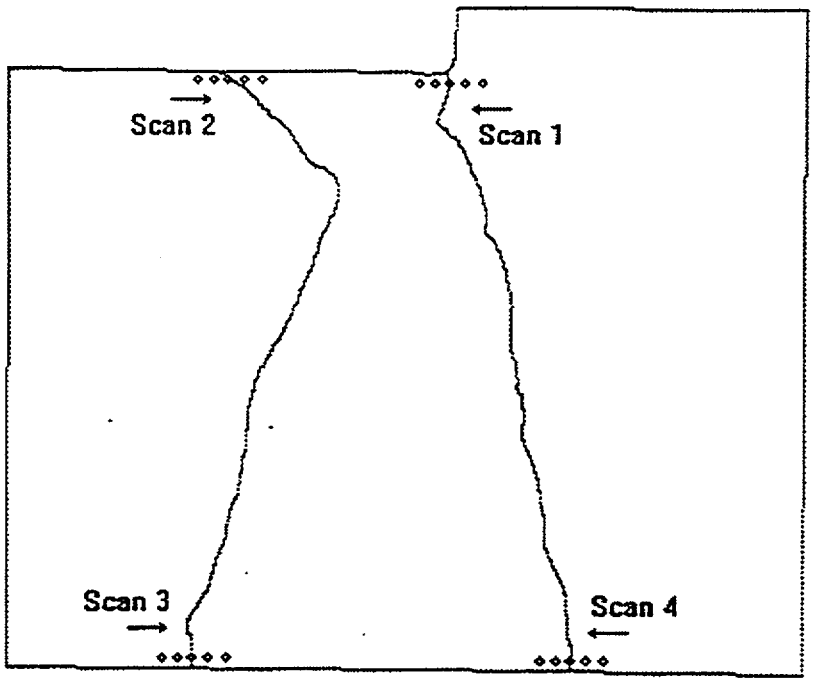

Weld H6A Impression #	Scan 1	Scan 2	Scan 3	Scan 4

Content Deleted -
EPRI Proprietary Information

Cross Section of Weld H6A

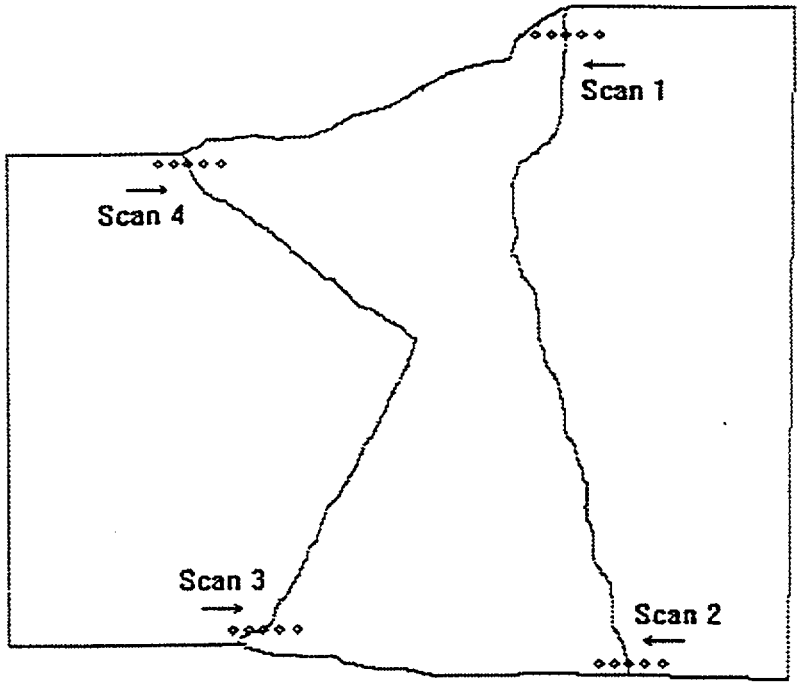

Weld H6B

Impression #	Scan 1	Scan 2	Scan 3	Scan 4

Content Deleted -
EPRI Proprietary Information

Cross Section of Weld H6B

Conclusions

Content Deleted -
EPRI Proprietary Information

References

1. *BWR Recirculation Piping System Replacement.* EPRI Document NP-6723-D, Project T305. June 1990

2. ASTM Standards, Specification E837

3. Avallone, E.A., Baumeister, T. Marks Standard Handbook for Mechanical Engineers, Ninth Edition 1987

4. Cofie, N.G., et al. *Evaluation of Corrosion Assisted Cracking of BWR Vessel Attachment Welds.* Interim Technical Report, November 1994

APPENDIX F

Through-Thickness Residual Stress Measurement on River Bend Core Shroud

Prepared by:

W. Cheng
I. Finnie
University of California, Berkeley

Appendix F: Through-Thickness Residual Stress Measurement - River Bend (UCB)

F.1 Through-the-Thickness Residual Stress Measurement

The residual stresses in the core shroud welds H5, H6A and H6B were measured by using the crack compliance method. In what follows a brief overview of the theoretical background and experimental procedures of the method is given. The results of the measurement for the core shroud welds are then presented.

F.2 Theoretical Background

The crack compliance method is based on the linear superposition for a thin cut of progressively increasing depth introduced on a body with residual stresses. That is, the deformation due to releasing residual stresses, as shown in Fig. F-1, is the same as that produced by applying the same stress with opposite sign to the faces of the crack. The computational model for the crack compliance method is obtained for a crack subjected to an arbitrary surface traction on its faces [1].

The unknown residual stress distribution is first represented by a series

$$\sigma(x) = \sum_{i=0}^{n} \sigma_i P_i(x) \tag{1}$$

in which σ_i is the amplitude factor for the ith term $P_i(x)$. When the change of strain ε is measured during cutting, the relation between the stress released and the strain measured may be expressed as

$$\epsilon(a) = \sum_{i=0}^{n} \frac{\sigma_i}{E'} C_i(a) \tag{2}$$

where E' is an elastic constant and $C_i(a)$ is the crack compliance function for the surface traction $P_i(x)$. Crack compliance functions have been obtained by using solutions from fracture mechanics or by finite element computations. When a number m > n+1 of strain measurements are made, a least squares fit can be used to minimize the average error involved in the measurement and estimation. This procedure leads to a set of n+1 linearly independent equations, i. e.

$$\frac{\partial}{\partial \sigma_i} \sum_{j=1}^{m} [\epsilon(a_j) \quad \sum_{k=0}^{n} \sigma_k C_k(a_j)]^2 \quad 0 \qquad i \quad 0, \ldots, n \tag{3}$$

from which the unknown σ_i can be solved.

F.3 Experimental Procedures

Strain gages are installed on specimens at locations optimal for measurement of residual normal stresses. Electrical discharge wire machining (EDWM) is usually used to introduce a thin cut of increasing depth as shown in Fig F-2. The test is carried out in a temperature-controlled

environment. For through-thickness measurement more than fifty strain reading can be recorded in a test and are used to estimate the residual stresses over about 4% to 96% of the thickness.

F.4 Measurement of Residual Stress Distribution in Core Shroud Welds

Figure F-3a shows the configurations of the specimens for welds H5, H6A and H6B. Since the state of residual stress changes when the specimens were removed from the core shroud, the original residual stresses σ consist of two parts

$$\sigma = \sigma_1 \quad \sigma_2 \tag{4}$$

in which σ_1 is the stress to be measured in a specimen and σ_2 is the change of the stress when the specimen is cut out. The first part of the stress (σ_1) determination is discussed in the next section. The profile of the welds and the planes, on which the residual axial stress will be measured, are shown in Fig. F-3b.

F.4.1 Residual Stresses in the Specimens for H5, H6A and H6B

F.4.1.1 Results for H5

The residual stress in weld H5 was measured first. A cut of progressively increasing depth is made from I.D. on a plane near the heat affected zone (HAZ) while the change of strain was measured by two strain gages (CEA-06-062UW-120) on the back face opposite the cut. Figure F-4 shows the strains measured as a function of the depth of cut. The strain readings of the two gages were stable and consistent throughout the test. The average of the readings from the two strain gages was used to estimate the residual stress.

Only the elastic properties of the material are required for stress estimation. It is assumed that the properties for the base and weld metals are the same. Table F.1 lists the material properties used in the computation.

Content Deleted -
EPRI Proprietary Information

F.4.1.2 Results for H6A

The specimen containing weld H6A had machined surfaces on both I.D. and O.D.. An axial weld was also contained in the thin section of the specimen. The measurement was carried out on a plane near the corner of the joint between the thin and thick sections by a cut introduced from the I.D.. Two strain gages (CEA-06-062UW-120) were installed on the back face (O.D.) opposite the

cut. Strains measured during cutting are plotted in Fig. F-6 against the depth of cut. Again, the readings were stable and consistent throughout the test.

Content Deleted -
EPRI Proprietary Information

F.4.1.3 **Results for H6B**

Both I.D. and O.D. surfaces of the specimen containing weld H6B were very rough in as received condition. To have a smooth surface for installation of strain gages, the surfaces were machined lightly by milling. The measurement was carried out on a plane near the HAZ on the thin section by a cut introduced from O. D. Two strain gages (CEA-06-062UW-120) were installed on the back face (I.D.) opposite the cut. Strains measured during cutting are plotted in Fig. F-8 against the depth of cut. Similar to the previous two tests, the readings were stable and consistent throughout the test.

Content Deleted -
EPRI Proprietary Information

F.4.2 **Estimation of the Stress Change Due to Removal of the Specimen (H5)**

When the specimen was removed from the core shroud, the change of hoop and axial strains were recorded on O.D., which are given in Table F.2. The change of the stresses on the surface can be obtained directly from stress-strain relation, which leads to :

Content Deleted -
EPRI Proprietary Information (5)

Assuming that the original residual stresses are axisymmetric and the change of the axial stress is only due to release of a resultant moment[1], for a thin-walled cylinder the distribution of stress σ_2 in Eq. (4) may be expressed as

$$\sigma_2 = \sigma_a(1 - 2\frac{x}{t}) \tag{6}$$

where t is the wall thickness and x is the distance from the inside wall. Figure F-10 displays the total stress σ as a function of the distance normalized by the wall thickness.

F.4.2 **Estimation of the Stress Change Due to Removal of the Specimen (H6A)**

In the previous section the bending stress released at weld H5 was obtained. Since H5 was made last in manufacturing, the bending stress produced by "tuck in" during cooling is expected to

[1]The resultant force due to weight is found to be very small and is therefore neglected.

be higher than those at other welds. Also, we need to estimate the influence of the bending stress that may have on the nearest weld H6A. In what follows an analysis will be carried out to obtain the magnitude of the moment that exists at H6A.

For a thin-walled cylinder the solution of the radial displacement w(x) is given by [2]

$$w(x) = e^{\beta x}(C_1 \cos\beta x + C_2 \sin\beta x) + e^{-\beta x}(C_3 \cos\beta x + C_4 \sin\beta x) \tag{7}$$

from which we find

$$\frac{dw(x)}{dx} = \beta e^{\beta x}[C_1 \phi(\beta x) + C_2 \theta(\beta x)] - \beta e^{-\beta x}[C_3 \theta(\beta x) - C_4 \phi(\beta x)] \tag{8}$$

$$\frac{d^2w(x)}{dx^2} = 2\beta^2 e^{\beta x}(-C_1 \sin\beta x + C_2 \cos\beta x) + 2\beta^2 e^{-\beta x}(C_3 \sin\beta x - C_4 \cos\beta x) \tag{9}$$

$$\frac{d^3w(x)}{dx^3} = 2\beta^3 e^{\beta x}[-C_1 \theta(\beta x) + C_2 \phi(\beta x)] + 2\beta^3 e^{-\beta x}[C_3 \phi(\beta x) + C_4 \theta(\beta x)] \tag{10}$$

where $\beta = [3(1-\mu^2)/(R^2t^2)]^{1/4}$.

$$\phi(\beta x) = \cos\beta x - \sin\beta x \quad \textit{and} \quad \theta(\beta x) = \cos\beta x + \sin\beta x \tag{11}$$

We now proceed to determine the constants C_1 through C_4 for a cylinder consisting of three sections with different R/t ratios. The boundary conditions at x = 0, x = L_1 and x = L_2 are

$$\left(\frac{d^2w_1}{dx_1^2}\right)_{x_1=0} = -\frac{M}{D}; \quad \left(\frac{d^3w_1}{dx_1^3}\right)_{x_1=0} = 0;$$

$$w_1(L_1) = w_2(0); \quad \left(\frac{dw_1}{dx_1}\right)_{x_1=L_1} = \left(\frac{dw_2}{dx_2}\right)_{x_2=0}; \tag{12}$$

$$\left(\frac{d^2w_1}{dx_1^2}\right)_{x_1=L_1} = \left(\frac{d^2w_2}{dx_2^2}\right)_{x_2=0}; \quad \left(\frac{d^3w_1}{dx_1^3}\right)_{x_1=L_1} = \left(\frac{d^3w_2}{dx_2^3}\right)_{x_2=0};$$

$$w_2(L_2) = w_3(0); \quad \left(\frac{dw_2}{dx_2}\right)_{x_2=L_2} = \left(\frac{dw_3}{dx_3}\right)_{x_3=0};$$

$$\left(\frac{d^2w_2}{dx_2^2}\right)_{x_2=L_2} = \left(\frac{d^2w_3}{dx_3^2}\right)_{x_3=0}; \quad \left(\frac{d^3w_2}{dx_2^3}\right)_{x_2=L_2} = \left(\frac{d^3w_3}{dx_3^3}\right)_{x_3=0}, \tag{13}$$

in which $D = Et^3/[12(1-\mu^2)]$ and superscripts 1, 2 and 3 are used to denote the three sections of the cylinder. Since the final result is independent of D we set it to unity for simplicity. Also, as x_3 approaches infinity the first two constants C_1^3 and C_2^3 for w_3 must vanish. Thus we have a total of ten equations with ten unknowns: C_1^1 to C_4^1, C_1^2 to C_4^2 and C_3^3 to C_4^3.

Using Eqs. (7) to (10), Eqs. (12) and (13) in a matrix form become

$$\underline{A} \bullet C = B \tag{14}$$

where $\underline{A}$ =

$$\begin{bmatrix}
0 & 2\beta_1^2 & 0 & -2\beta_1^2 & 0 & 0 & 0 & 0 & 0 & 0 \\
-2\beta_1^3 & 2\beta_1^3 & 2\beta_1^3 & 2\beta_1^3 & 0 & 0 & 0 & 0 & 0 & 0 \\
e^{\lambda_1}\cos\lambda_1 & e^{\lambda_1}\sin\lambda_1 & e^{-\lambda_1}\cos\lambda_1 & e^{-\lambda_1}\sin\lambda_1 & -1 & 0 & -1 & 0 & 0 & 0 \\
\beta_1 e^{\lambda_1}\phi(\lambda_1) & \beta_1 e^{\lambda_1}\theta(\lambda_1) & -\beta_1 e^{-\lambda_1}\theta(\lambda_1) & \beta_1 e^{-\lambda_1}\phi(\lambda_1) & -\beta_2 & -\beta_2 & \beta_2 & -\beta_2 & 0 & 0 \\
-2\beta_1^2 e^{\lambda_1}\sin\lambda_1 & 2\beta_1^2 e^{\lambda_1}\cos\lambda_1 & 2\beta_1^2 e^{-\lambda_1}\sin\lambda_1 & -2\beta_1^2 e^{-\lambda_1}\cos\lambda_1 & 0 & -2\beta_2^2 & 0 & 2\beta_2^2 & 0 & 0 \\
-2\beta_1^3 e^{\lambda_1}\theta(\lambda_1) & 2\beta_1^3 e^{\lambda_1}\phi(\lambda_1) & 2\beta_1^3 e^{-\lambda_1}\phi(\lambda_1) & 2\beta_1^3 e^{-\lambda_1}\theta(\lambda_1) & 2\beta_2^3 & -2\beta_2^3 & -2\beta_2^3 & -2\beta_2^3 & 0 & 0 \\
0 & 0 & 0 & 0 & e^{\lambda_2}\cos\lambda_2 & e^{\lambda_2}\sin\lambda_2 & e^{-\lambda_2}\cos\lambda_2 & e^{-\lambda_2}\sin\lambda_2 & -1 & 0 \\
0 & 0 & 0 & 0 & \beta_2 e^{\lambda_2}\phi(\lambda_2) & \beta_2 e^{\lambda_2}\theta(\lambda_2) & -\beta_2 e^{-\lambda_2}\theta(\lambda_2) & \beta_2 e^{-\lambda_2}\phi(\lambda_2) & \beta_3 & -\beta_3 \\
0 & 0 & 0 & 0 & -2\beta_2^2 e^{\lambda_2}\sin\lambda_2 & 2\beta_2^2 e^{\lambda_2}\cos\lambda_2 & 2\beta_2^2 e^{-\lambda_2}\sin\lambda_2 & -2\beta_2^2 e^{-\lambda_2}\cos\lambda_2 & 0 & 2\beta_3^2 \\
0 & 0 & 0 & 0 & -2\beta_2^3 e^{\lambda_2}\theta(\lambda_2) & 2\beta_2^3 e^{\lambda_2}\phi(\lambda_2) & 2\beta_2^3 e^{-\lambda_2}\phi(\lambda_2) & 2\beta_2^3 e^{-\lambda_2}\theta(\lambda_2) & -2\beta_3^3 & -2\beta_3^3
\end{bmatrix}$$

and

$$C = \begin{bmatrix} C_1^1 \\ C_2^1 \\ C_3^1 \\ C_4^1 \\ C_1^2 \\ C_2^2 \\ C_3^2 \\ C_4^2 \\ C_3^3 \\ C_4^3 \end{bmatrix}, \qquad B = M_0 \begin{bmatrix} -1 \\ 0 \\ 0 \\ 0 \\ 0 \\ 0 \\ 0 \\ 0 \\ 0 \\ 0 \end{bmatrix} \tag{16}$$

where $\lambda_1 = \beta_1 L_1$ and $\lambda_2 = \beta_2 L_2$.

For the configuration given in Table F-3 and Poisson's ratio $\mu = 0.3$ the constants C_1^1 to C_4^1, C_1^2 to C_4^2 and C_3^3 to C_4^3 are calculated numerically and are shown in Table F-4. The moment at $x_1 = L_1$ is given by

$$M = -\left(\frac{d^2 w_1}{dx_1^2}\right)_{x_1 = L_1} = 0.21 \times M_0$$

Content Deleted -
EPRI Proprietary Information

References

1. Cheng, W. and Finnie, I., "An Overview of the Crack Compliance Method for Residual Stress Measurement," Proceedings of Fourth Int. Conf. on Residual Stresses, pp.449-458, 1994.

2. Den Hartog, J. P., Advanced Strength of Materials, McGraw-Hill, Chapter V, 1952.

Table F.1 Material Properties Used in Computation

Elastic modulus $E = 29\times10^6$ psi	Poisson's ratio $\mu = 0.3$

Table F.2 Change of strains measured after the specimen is removed.

Content Deleted -
EPRI Proprietary Information

Table F-3 Configuration of a thin-walled cylinder with three sections

$L_1 = 18$ inches	$R_1 = 91.625$ inches	$t = 2.5$ inches	$\beta_1 = 0.08493$
$L_2 = 7.5$ inches	$R_2 = 90.125$ inches	$t = 5.5$ inches	$\beta_2 = 0.05773$
$L_3 =$ infinite	$R_1 = 89.19$ inches	$t = 2.5$ inches	$\beta_3 = 0.08608$

Table F-4 Values of the constants determined for the displacement solution

Content Deleted -
EPRI Proprietary Information

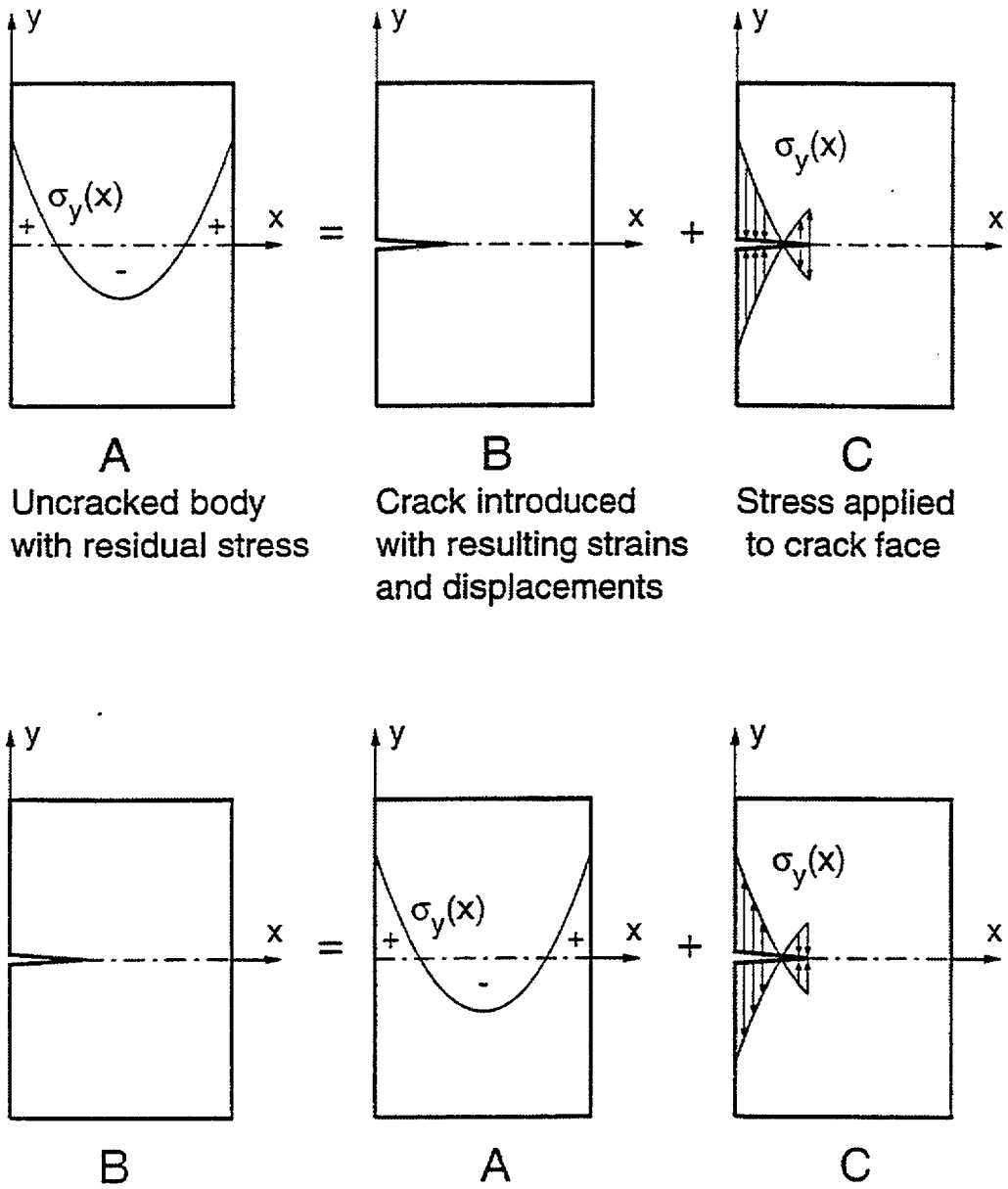

Figure F-1 Illustration of linear superposition for determining strains due to introducing a crack into a body with residual stresses

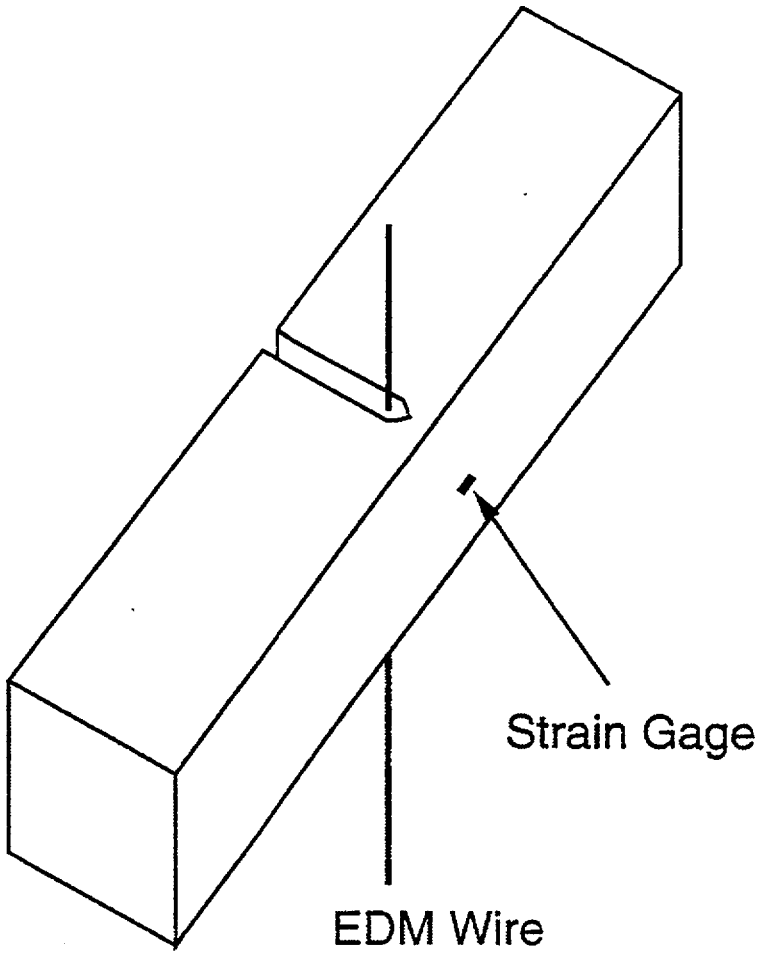

Figure F-2 Residual stress distribution in a beam obtained by introducing a cut of increasing depth while measuring strain on the back face

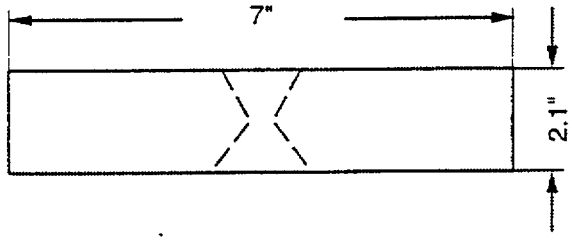

(Weld H5)

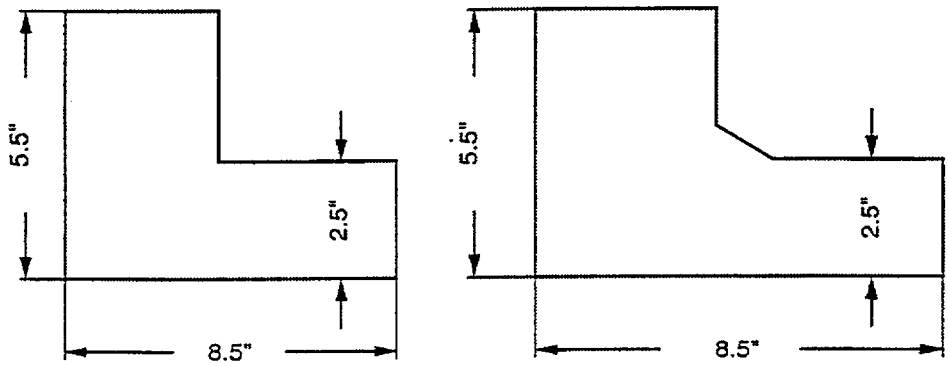

(Weld H6A and H6B)

Figure F-3a Specimens for weld joints H5, H6A and H6B

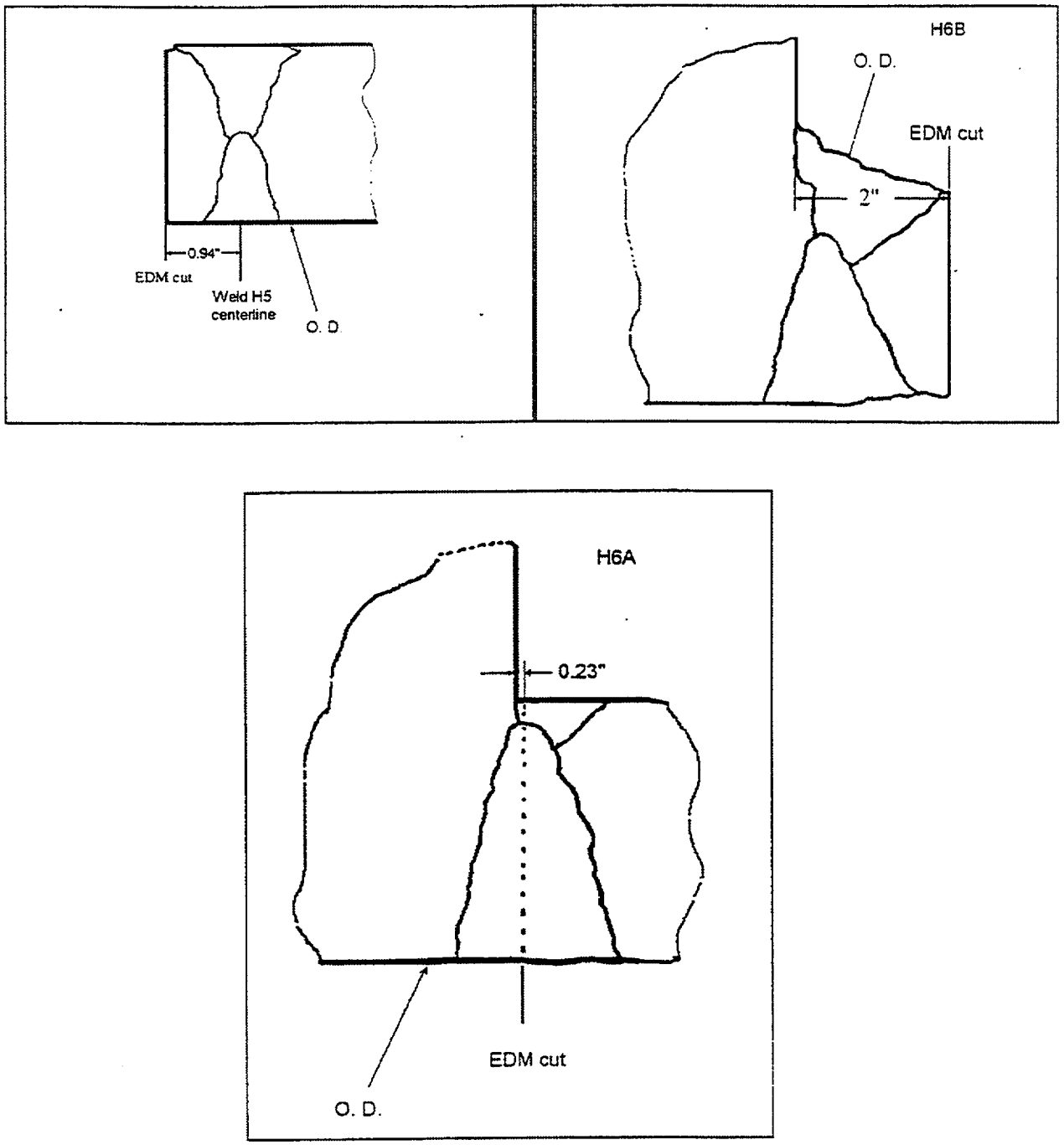

Figure F-3b Profile of the welds and the planes where residual axial stresses to be measured.

Content Deleted -
EPRI Proprietary Information

Figure F-4 Strain measured for weld H5

Content Deleted -
EPRI Proprietary Information

Figure F-5 Residual normal stress distribution near weld H5

Content Deleted -
EPRI Proprietary Information

Figure F-6 Strains measured for weld H6A

Content Deleted -
EPRI Proprietary Information

Figure F-7 Residual normal stress distribution at the weld H6A

Content Deleted -
EPRI Proprietary Information

Figure F-8 Strains measured for weld H6B

Content Deleted -
EPRI Proprietary Information

Figure F-9 Residual normal stress distribution near weld H6B

Content Deleted -
EPRI Proprietary Information

Figure F-10 Residual axial stress distribution near weld H5

APPENDIX G

Near Surface Residual Stress Measurements at Grand Gulf Nuclear Station

Prepared by:

M. Shields
S. Toledo
T. Togami
Sandia National Laboratories

Results of the Residual Stress Measurements Performed on the

Grand Gulf Nuclear Station Core Shroud

Field Test Date: June 25-July 1, 1995
Report Submitted: August 25, 1995

Report by: Thomas Togami

Team Members: Marlene Shields
Seyfred Toledo
Thomas Togami

Acknowledgment

This project was funded by the DOE Office of Nuclear Energy Science and Technology in support of the Boiling Water Reactor Vessel and Internals Project (BWRVIP). The project was developed and coordinated with the BWRVIP and Stan T. Rosinski, DOE's Light Water Reactor Technology Center at Sandia National Laboratories/New Mexico.

Introduction

The goal of this field test was to provide the BWRVIP (Boiling Water Reactor Vessel and Internals Project) with residual stress measurements performed on a spare reactor core shroud. These measurements would supplement a larger study whose goal was to determine a new crack growth rate constant for these reactor core shrouds.

The spare reactor core was stored outdoors at the Grand Gulf Nuclear Station (GGNS) in Mississippi. The shroud was constructed of 304 Stainless Steel and measured approximately 20 feet in height and 20 feet in diameter. Overall, the shroud had a wall thickness of approximately 2 inches.

Residual stress measurements were desired for five weld locations on the outer and inner surfaces, at the same location on the circumference. The test plan called for measurements at the H3, H4, H5, H6A and H6B welds. The locations of the welds are shown in Figure 1. At each weld location, a measurement was desired at the weld, inside the heat affected zone (HAZ) and outside the HAZ. The H3 OD (Outer Diameter), H6A ID (Inner Diameter) and H6B ID & OD welds would not be measured since they were fillet welds. Initially, 26 measurements were required.

The first step in the test plan was to identify a test method that would be most appropriate for the shroud and the environment in which these measurements would be made. Due to the size of the shroud and the measurement locations, the test method had to be portable and simple with a quick set-up period. The method would also have to be insensitive to an outdoor test environment.

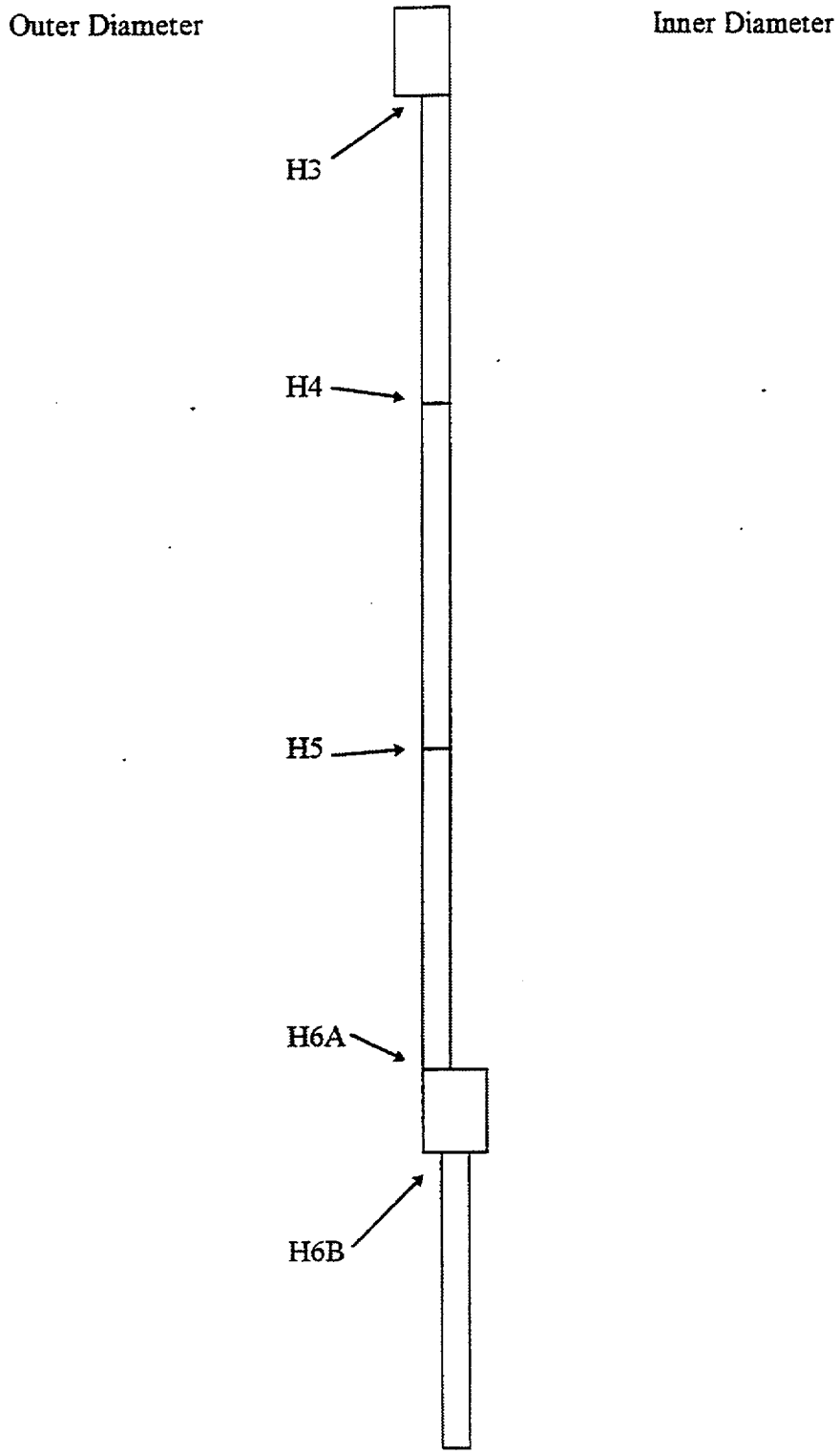

Figure 1. Approximate Location of Welds. (DWG not to Scale)

After reviewing several different residual stress testing methods and considering the working environment, the blind-hole-drilling method was chosen. The hole-drilling method was one in which a strain gage rosette was bonded to a test specimen. The rosette was made up of three strain gages arranged on a circle at three angles, 0°, 45°, and 90°. At the center of the circle, referred to as the gage-circle, were alignment marks indicating the center of the gage-circle. Each gage was monitored using a single strain indicator. A hole had to be introduced into the center of the gage circle within $\pm$ 0.001 inch. The hole diameter was defined by a ratio of the hole diameter D_0, and the gage-circle diameter D. The suggested limit for the ratio of D_0/D was within 0.30 to 0.50. The hole depth, Z was defined as a fraction of the gage-circle diameter, 0.4D.

As the hole was drilled into the test material, strain was relieved proportionally to the residual stress. The relieved strain was measured as a function of depth such that the stress uniformity could be evaluated as a function of depth. The purpose of this step was not to determine the residual stress as a function of depth, but to determine if the residual stress was uniform with depth. The residual stress measurement was made at the full hole depth of Z = 0.4D.

Assumptions

The blind-hole drilling method was a simple process but it did have limitations and certain assumptions had to be considered. The hole drilling method was based upon a strain gage measurement which was a surface measurement. This implied that the surface

and near surface conditions of the test material had to meet certain requirements to arrive at an accurate measure of the residual stress.

1. The surface of the material should not be sandblasted or ground. These processes would introduce compressive and tensile residual stresses respectively, near the surface of the test material
2. The stress must be uniform with depth. A non-uniform stress condition can result in calculated stresses lower than the actual maximum residual stress.
3. The drill operation should not introduce stress into the test material. This would obviously contaminate the measurements and result in erroneous data.
4. Because the measurement is based on the elastic response of the test material, the stress must be in the elastic range of the material. If the residual stress is at or beyond the yield stress of the material, the calculated stress may be higher than the actual stress. The magnitude of the error depends upon the slope of the stress strain diagram in the plastic region and the amount of localized yielding at the hole.
5. The temperature of the shroud should be monitored such that the measurements would not include variation due to thermal stresses.

The second assumption is based on the fact that no closed form solution from the theory of elasticity exists for the blind-hole geometry. However, if the stress is uniform as a function of depth, then the blind-hole analysis is very similar to the through-hole analysis. Assumption 1 was a primary concern but the information provided initially suggested that the welds were in an "as welded" condition.

Hole Drilling Apparatus

The Measurements Group Inc. RS-200 Milling Guide was used for the residual stress measurements because it provided the features required in the technique in a complete package. The milling guide consisted of an adjustable base on which an optical scope and a high speed air turbine could be mounted. The milling guide had three adjustable feet that were bonded to the test specimen after the rosette was mounted. The milling guide was roughly centered on the gage-circle and then leveled. A type of "dental cement" was used to mount the milling guide to the test material. The milling guide was realigned on the rosette after bonding with the use of the optical scope and the fine X-Y adjustment screws. The scope was then replaced with the high speed air turbine in the milling guide. The milling guide had a micrometer depth gage that accurately measured the incremental hole depth.

The high speed air turbine was used with a carbide end-mill because it had been shown that this arrangement could be used to successfully test without introducing stress into the test material.[1,2] The air turbine arrangement was also shown to be operator independent unlike a typical drill procedure.

The two types of strain gage rosettes that were used in this test series were manufactured by Measurements Group Inc. The TEA-09-062RK-120 rosette was designed such that gage number one was positioned at 90°, gage two at 225° and gage three at 0°. The rosette measured approximately 0.6 inch by 0.6 inch square. This rosette was best suited for measuring outside the HAZ and in some cases. the weld center line. The CEA-09-062UM-120 was designed with gage number one at 135°, gage two at

90° and gage three at 45°. This rosette was specifically designed for making measurements very close the edge of the weld since all the gages were on one side of the gage-circle. This rosette was used to make measurements in the HAZ and on narrow welds. The CEA rosette was smaller than the TEA rosette and measured 0.4 by 0.5 inches.

Both gages had a gage-circle diameter of 0.202 inches. The end-mill hole diameter measured 0.072 inches. The carbide end-mill had a 0.062 inch diameter but the hole diameter was larger due to the slight eccentricity of the high speed air turbine. The air turbine was rotated in the milling guide to eliminate the hole offset due to the eccentricity. The full depth of the drilled hole was 0.081 inches. Strain measurements were made at 0.008 inch increments until a depth of 0.072 inches.

Following the calibration process and equipment checkout, it was decided to include two locations on the circumference 180° apart. This would double the number of measurements but it was felt that it could be accomplished in a reasonable amount of time.

Field Test

The tests were performed from June 25 through July 1, 1995 at the lay-down yard at the Grand Gulf Nuclear Power Station. The shroud was in an upright position on a concrete slab. Visual inspection revealed that the welds were ground and sandblasted. Although this could result in erroneous data, it was decided to proceed.

A TEA or CEA rosette was to be bonded on the weld center and a CEA rosette would be used for the HAZ measurement. The placement of the rosette outside the HAZ

was difficult to determine because the weld and surrounding area was sandblasted. It was advised by personnel at GGNPS that the HAZ was very narrow and the rosette could be placed 1.0 to 1.5 inches from the fusion line for a measurement outside the HAZ.

Before the rosette could be bonded to the shroud, the surface had to be cleaned and prepared. The mounting area on the shroud was sanded with 400 grit sand paper and M-Prep cleaner. The sanding was kept to a minimum so as not to relieve the residual stress near the surface.

Measurements Group M-Bond 200 adhesive was used to bond the gage to the shroud. M-Bond 200 has a tendency to absorb moisture and delaminate under high humidity conditions so the rosettes and surrounding glue lines were coated with M-Coat C. M-Coat C was a clear silicone coating that was insensitive to moisture. M-Coat C also had the advantage that it did not reinforce the rosette. The M-Coat C was very effective as none of the rosettes delaminated during the test series.

The outdoor conditions dictated that an additional strain gage be mounted to the shroud to monitor the strain induced by thermal expansion. If the measurement from the additional strain gage fluctuated noticeably over a five minute period, testing was discontinued until the following morning. To increase the number of measurements that could be made while the shroud was free from varying thermal stresses, testing began at 4:00 AM and continued until approximately 11:00 AM. The last three days were overcast and allowed measurements to be made until approximately 3:00 PM.

Testing began at two locations on the circumference. Two witness marks from the fabrication of the shroud were located, indicating the 0° position and the 180° position.

Measurements on the circumference were made relative to these marks. Measurements performed on the West side of the shroud were at the 14.9° location. On the East side of the shroud, measurements were performed at the 194.7° location.

The H6A ID (Inner Diameter) at the 14.9° and 194.7° locations and the H6A OD (Outer Diameter) at the 194.7° location were machined and therefore not measurable. The H3 HAZ locations at both circumferential locations on the OD were not measured because the flange above the weld did not allow sufficient clearance for the milling guide.

The drilling proceeded smoothly with only a few minor problems. The end-mills were changed after two or three holes depending on the condition of the end-mill and how easily the hole was drilled. The only measurement that was compromised by a bad end-mill was the H5 weld, inner diameter, outside the HAZ, at the 194.7° position. The end-mill fractured and caused a considerable change in measured strain when the bit failed.

Many of the welds exhibited various drilling characteristics with no discernible pattern. The HAZ and weld centers exhibited various degrees of difficulty in drilling the holes. Some areas were extremely tough and required very careful drilling, while the identical weld at the same zone on the opposite side of the wall was easily drilled. Overall, the locations outside the HAZ were easily drilled.

On some occasions, gages that were mounted close to each other were both monitored as the hole was being drilled. This was done as a check to determine if drilling of one gage could possibly effect the adjacent gage. It was determined that the close proximity of some of the gages had no effect on each other.

Data Reduction

The first step in the data reduction process was to determine if the stress was uniform as a function of depth. This was accomplished using relations provided by Measurements Group along with their data-reduction coefficients for the rosettes. Two sets of the coefficients, a and b, were derived. One set was to calculate the equivalent stress at incremental depths, and the other set was to calculate the residual stress at the final hole depth [2,3]. The relation for the equivalent principal stress magnitudes is given by Equation 1.

$$\sigma_{\min}, \sigma_{\max} = \frac{\varepsilon_3 + \varepsilon_1}{4A} \pm \frac{\sqrt{(\varepsilon_3 - \varepsilon_1)^2 + (\varepsilon_3 + \varepsilon_1 - 2\varepsilon_2)^2}}{4B} \tag{1}$$

Where:

$$A = \left(-\frac{1+\upsilon}{2E}\right) \cdot a \qquad B = \left(-\frac{1}{2E}\right) \cdot b$$

ν = Poisson's Ratio
E = Modulus of Elasticity
ε_i = i^{th} Strain gage measurement

If the stress is uniform with depth, then the equivalent stresses versus hole depth will plot as two horizontal lines. The coefficients a and b for the equivalent stresses, derived by [3] were given as a function of normalized depth ratio of Z/D. The variable Z was the hole depth and D was the gage-circle diameter. The coefficients were given over a Z/D range from 0.0 to 0.25. The final normalized drill depth used in the tests was 0.4 so the equivalent stress could only be derived up to 50% of the hole depth. For the final evaluation of the residual stress, the constants a and b were given by Measurements Group for the two rosettes.

The principal stress directions were determined using Equation 2 as referenced in Measurements Group Technical Note TN-503-4, and the ASTM Spec. E 837-94.

$$\beta = \frac{1}{2}\arctan\left[\frac{\varepsilon_3 + \varepsilon_1 - 2\varepsilon_2}{\varepsilon_3 - \varepsilon_1}\right] \tag{2}$$

The angle β is measured relative to the number one strain gage on the rosette. Since this relation may be incorrect by ±90°, a comparison of the numerator and denominator was made to obtain the correct angle.

Experimental Results

A total of 39 measurements were made on the shroud. Each measurement consisted of ten strain measurements recorded at 0.008 inch increments. The data was reduced as recommended in the Measurements Group Technical Note TN-503-4 and ASTM Spec. E 837-94. Once the data were reduced, the equivalent stresses were calculated for each measurement at the incremental depths. It should be emphasized that the calculated stresses presented here were based on an elastic response.

Content Deleted -
EPRI Proprietary Information

The data presented does not account for the effects of the grinding and sandblasting. The uniform nature of the stress as a function of depth was based upon the equivalent stress derived for the depths beyond 0.024 inches. The nature of the stress as a function of hole depth was evaluated and categorized into three groups. Equivalent stresses that plotted out as straight horizontal lines were referred to as "good," equivalent stresses that plotted as slightly curved lines or were slightly angled were referred to as "marginal." The last category referred to as "non-uniform" were equivalent stress plots that did not fall into the other two categories.

Content Deleted -
EPRI Proprietary Information

Figures 2a, 2b, 2c, and 2d are the plots of the stress levels for the two locations, inner and outer diameter. Measurements evaluated as non-uniform are omitted from these plots. The results can vary a great deal at one weld location, but that was expected since

Content Deleted -
EPRI Proprietary Information

Figure 2a. Residual Stresses for the NW Sector, 14.9° Location, Outer Diameter.

Content Deleted -
EPRI Proprietary Information

Figure 2b. Residual Stresses for the NW Sector, 14.9° Location, Inner Diameter.

Content Deleted -
EPRI Proprietary Information

Figure 2c. Residual Stresses for the SE Sector, 194.7° Location, Outer Diameter.

Content Deleted -
EPRI Proprietary Information

Figure 2d. Residual Stresses for the SE Sector, 194.7° Location, Inner Diameter.

the welding process itself is not a uniform process. The results also show the variation between the two locations on the circumference as well as the difference between the inner and outer diameter.

Content Deleted -
EPRI Proprietary Information

Table 1a. Residual Stresses for the 14.9° Position, Outer Diameter

Content Deleted -
EPRI Proprietary Information

Table 1b. Residual Stresses for the 14.9° Position, Inner Diameter.

Content Deleted -
EPRI Proprietary Information

Table 1c. Residual Stresses for the 194.7° Position, Outer Diameter.

Content Deleted -
EPRI Proprietary Information

Table 1d. Residual Stresses for the 194.7° Position, Inner Diameter.

Figures 3 and 4 show the difference between the uniform and non-uniform equivalent stresses. The plot shown in Figure 3 has the two horizontal lines following the initial depths affected by the sandblasting. Figure 4 shows the erratic response more likely caused by a non-uniform stress gradient through the depth of the hole.

Content Deleted -
EPRI Proprietary Information

Figure 3. "Good" Uniform Equivalent Stress

Content Deleted -
EPRI Proprietary Information

Figure 4. Non-Uniform Equivalent Stress

Conclusions

When the hole-drilling technique was chosen for this test, concerns were raised about the surface condition of the welds and the possibility of non-uniform stress conditions. The results show that these two factors were encountered and affected the

Content Deleted -
EPRI Proprietary Information

Content Deleted -
EPRI Proprietary Information

Content Deleted -
EPRI Proprietary Information

References

1. "*Measurement of Residual Stress by the Hole-Drilling Strain Gage Method,*" Measurements Group Inc. Technical Note TN-503-4, Raleigh, NC 1993.

2. "*Determining Residual Stresses by the Hole-Drilling Strain Gage Method,*" ASTM Standard E837-94, Philadelphia, 1994.

3. Schajer, G.S., "Measurement of Non-Uniform Residual Stresses Using the Hole Drilling Method," *Journal of Engineering Materials and Technology*, **110**, No 4: Part I, 338-343; Part II, 344-349 (1988).

DOMINION ENGINEERING, INC.

Analytical Prediction of Residual Stresses in BWR Shroud Welds

November 1995

Prepared by:

M. A. Kreider
D. J. Gross
E. S. Hunt

Prepared for

Electric Power Research Institute
3412 Hillview Avenue
Palo Alto, CA 94303

Table of Contents

Section		Page
H.1	Weld Joints Analyzed	H-1
H.2	Analysis Approach	H-1
	Factors Which Affect Weld Residual Stresses	H-2
	Key Modeling Assumptions	H-2
	Material Properties	H-3
	Finite Element Mesh Characteristics	H-5
	Modeling of Welding Process	H-6
	Modeling of Post Weld Heat Treatment	H-9
	Modeling of Crack Growth	H-9
H.3	Analysis Results	H-10
H.4	Comparison of Calculated and Measured Residual Stresses	H-11
	Surface Stresses	H-11
	Through-Thickness Stresses	H-12
H.5	References	H-14

Analytical Prediction of Residual Stresses in Shroud Welds

The purpose of this appendix is to describe finite element analyses which were performed to compute residual stresses in typical BWR core shroud welds. This appendix also compares the computed welding residual stresses to the results of experimental residual stress measurements performed on actual shrouds and shroud mockups.

H.1 Weld Joints Analyzed

BWR core shrouds are fabricated from rolled plate sections and rings. These parts are joined by full-penetration welds which run in the longitudinal and circumferential directions as shown in Figure H-1. This study focuses on modeling the circumferential welds since the most significant cracking in terms of extent and depth has been reported to be in the heat-affected zones (HAZ) of the circumferential welds. In comparison, axial cracks have tended to be both short and relatively shallow.

Analyses were performed for circumferential welds in both the River Bend (BWR-6) shroud and a shroud mockup fabricated by TEPCO. The River Bend shroud was selected for analysis since the unused shroud for River Bend Unit 2 has been experimentally examined to determine residual stresses in several circumferential welds. The TEPCO shroud mockup was selected for analysis since it included an H2/H3 weld joint similar in design to shrouds which have developed cracks in the United States, and also because stresses in the mockup were determined experimentally.

The location of each River Bend weld that was analyzed is shown on Figures H-2a through H-2d. In addition, each figure includes an excerpt from the relevant design drawing for the shroud (Reference (8)) that details the weld of interest. Figure H-2e shows the location of the TEPCO welds that were analyzed. Schematic enlargements of the weld details for the two designs are provided in Figures H-3 and H-4.

H.2 Analysis Approach

Welding residual stresses and crack-tip stress intensities in the circumferential shroud welds were computed using the ANSYS finite element code (Revision 5.1).

Factors Which Affect Weld Residual Stresses

The residual stresses in the vicinity of shroud welds depend upon many factors including:

- Dimensions of the shroud and welds
- Thermal and mechanical properties of the base metal and weld metal as a function of temperature
- Cold work performed on the base metal during fabrication (e.g., forming into a round shell, surface grinding, polishing)
- Thermal and physical characteristics of the welding process (e.g., heat input rate, weld rod size, number and distribution of weld passes, welding speed, interpass temperature)
- Fabrication and heat treatment history of the shroud assembly

All of these factors can have a significant impact on the final stresses existing after the last weld pass has cooled.

Key Modeling Assumptions

While all of the factors described in the previous paragraph can affect residual stresses in the parts after welding, attempts to quantify many of these variables often result in one of two situations: a) the desired information is unavailable, probably because it was never recorded during the fabrication process, or b) inclusion of the information would result in an unacceptably complex finite element model. As a result, it is necessary to make simplifying assumptions in the analysis work.

The main assumptions used for the shroud residual stress analyses are listed below.

1. All models are fully axisymmetric, i.e., they are two-dimensional in nature. Variations in the circumferential direction are neglected. This has two important consequences: a) the welding process is assumed to deposit weld metal at all locations around the circumference simultaneously, and b) when a circumferential crack is initiated, it covers the full 360° of the circumference.

2. The volume of metal in each weld pass remains static during the welding process, and conforms to the shape of the finished pass. This is an

approximation, since an actual weld is deposited over time. Mixing between base metal and weld metal is neglected.

3. The heat distribution throughout the weld pool is approximated by assuming a uniform heat generation rate throughout the weld pool. The heat generation rate is increased linearly over a short period of time, then held constant at a maximum value, then decreased linearly to zero.

4. The weld metal reaches a peak temperature which is typically in the range of 3000–4000°F, and the HAZ, which is located about 50 mils from the fusion line, reaches a peak temperature which is typically in the range of 1200-1800°F. The heat generation rate in the weld pool and the length of the heating cycle are adjusted to produce these desired peak temperatures.

5. There is approximately one weld pass for every quarter inch of shroud thickness. This results in 8–10 weld passes for most of the welds examined. This figure is based on a sketch provided in the Sun Shipbuilding welding procedure (4) indicated on the shroud drawings (8). Although the procedure states that welded joints are to look like the sketch, the procedure does not state the number or distribution of passes for joints of different size and shape.

6. In all of the FEA models, the thickness of successive weld passes is adjusted to generate weld pools of approximately the same volume.

7. Except for the yield strength, all material properties for the base metal and weld metal are assumed to be identical.

8. The shroud and weld metal behave in an elastic-perfectly plastic manner. That is, once the nominal yield stress has been reached, the material will continue to experience additional strain without an increase in stress. It is considered that this provides a reasonable approximation to the residual stress state induced by the welding process.

9. Cold work of the base material prior to welding is not included in the finite element analysis. Although cold work undoubtedly provides a significant contribution to the residual stress state, there is no quantitative data on the amount of cold work which existed before welding. Also, the temperatures developed during the welding process will relieve some of the cold work stresses in the vicinity of the weld and HAZ.

Material Properties

The welding process raises the weld metal and portions of the base metal to temperatures above the melting point (about 2550–2600°F for 304 stainless steel). In addition, large volumes of the base metal are heated sufficiently to affect the thermal and mechanical properties of the material. Consequently, the analyses

were performed using temperature-dependent material properties. Specific values used in the analysis are reported in Table H-1. With the exception of the material yield strength, the values for temperatures 1200°F and less were taken from References (2) and (11).

Table H-1
Temperature-Dependent Material Properties Used in FEAs

Temp. °F	Yield Strength (ksi) (1)	Yield Strength (ksi) (2)	Young's mod. (10^6 psi)	Thermal exp. coeff. (10^-6/°F)	Poisson's ratio	Specific heat (BTU/lb-F)	Thermal Cond. (BTU/hr-ft-°F)
70	67.0	40.0	28.3	8.8	0.29	0.12	7.8
400	54.1	32.3	26.8	9.1	0.29	0.129	9.9
800	47.3	28.2	24.1	9.3	0.30	0.14	12
1200	34.9	20.8	23.0	9.8	0.29	0.15 (ext)	14.4
1600	18.4	11.0	17.0 (ext)	10.0 (ext)	0.25 (ext)	0.16 (ext)	16.8 (ext)
2300	2.3 (est)	1.4 (est)	1.0 (est)	10.3 (ext)	0.25 (est)	0.16 (est)	16.8 (est)
3500	2.3 (est)	1.4 (est)	0.5 (est)	10.6 (ext)	0.25 (est)	0.16 (est)	16.8 (est)

(ext) = extrapolated from lower temperatures
(est) = estimation
(1) = Used for the weld metal in all analyses and for the base metal in some analyses
(2) = Used for the base metal in some analyses

For all shroud models, the room-temperature yield strength of the weld metal is assumed to be 67 ksi as reported in weld certification tests for River Bend Unit 2 (3). The yield strength values at higher temperatures were scaled according to the stress-strain curve given on p. 9.29 of Reference (2) for 304 stainless steel. For temperatures intermediate to a pair of table entries (e.g., 1000°F), ANSYS interpolates linearly between the upper and lower values.

For each model, an initial analysis was performed in which the base metal has the same yield stress as the weld metal in the as-welded condition (67 ksi at room temperature). The base metal may actually have a yield stress lower than 67 ksi. However, the assumption of elastic-perfectly plastic material behavior does not provide for any strain hardening of the base metal. As a consequence, it is judged appropriate to select a higher yield strength than the nominal yield of the material. A logical choice for this higher value is the flow stress, which can be defined as the average of the yield and tensile strengths. For some forms of 304 stainless steel, Reference (11) lists 30 ksi and 75 ksi as minimum values for these properties, resulting in a minimum flow stress of 53 ksi. While this value is somewhat lower than the 67 ksi used in the first set of analyses, it is judged that

the use of 67 ksi tends to provide an upper bound for the residual stresses in the base metal. For the River Bend models, an additional set of analyses was performed using a base-metal yield strength of 40 ksi, a value typical of the material property tests cited in Reference (3). These analyses are expected to provide a somewhat more realistic distribution of the stresses in the base metal.

Little material property information is available for temperatures greater than about 1200°F. For temperatures above 1200°F, properties that behave in a nearly linear fashion at lower temperatures are extrapolated. For temperatures near or above the melting point (i.e., 2300°F and 3500°F), the yield strength and Young's modulus are estimated based on extrapolations carried out for a similar material (309 stainless steel). Except for the coefficient of thermal expansion, which is judged appropriate to extrapolate to 3500°F, the other properties (Poisson's ratio, specific heat, and thermal conductivity) are assumed to remain constant at their values for 1600°F.

With the exception of the yield strength, the mechanical and physical properties are assumed to be identical for the 304L stainless steel base metal and 308 stainless steel weld metal since these materials have similar characteristics.

Finite Element Mesh Characteristics

The finite element models generated in this study consist of 2-D planar elements. The ANSYS solid modeler is used to generate the basic features of the shroud and welds. This approach allows variables such as the shroud radius, weld size and shape, and the number of weld passes to be easily modified. The areas created with the solid modeler are meshed with ANSYS PLANE77 elements (8-node thermal solids) or PLANE82 elements (8-node structural solids), depending on the type of analysis performed. All elements are quadrilaterals, except in the vicinity of crack-tip locations.

In order to allow calculation of crack tip stress intensities (K_I), a series of crack-tip locations is generated along a path where cracks have been reported (7). This path is located parallel to, and 0.050 inches on the base-metal side of, the fusion line.

Crack-tip locations are surrounded by eight triangular wedges (ANSYS crack-tip elements) arranged to form a regular octagon (i.e., in the shape of a pizza pie).

The triangular crack-tip elements have mid-side nodes located one-quarter of the distance from the crack tip to the end of the element side. This placement generates a $\frac{1}{\sqrt{r}}$ singularity in the element shape function, which is essential for calculating stress intensity factors using linear elastic fracture mechanics theory. Figure H-5 shows an example of the mesh generated in the vicinity of the crack-tip locations.

In order to allow formation of a crack, the portions of the model above and below the crack line are connected by thermal and structural links during the welding process. After completion of welding, the links can be sequentially deleted to simulate growth of a crack.

Weld passes are modeled with four elements through the thickness of the pass and four elements along the axial length of the pass, for a total 16 elements per weld pass. Each model also includes sufficient material remote from the weld to simulate the presence of the remainder of the shroud (typically about 12 inches of material on either side of the weld centerline). Figure H-6 shows a typical element plot with the basic features labeled.

Three finite element models were created for the River Bend shroud using dimensions provided in Reference (8). One model was created for weld H3 which connects the shell to the upper ring. One model was created for welds H4 and H5 since the weld preparations are essentially identical for these two welds. One model includes welds H6a and H6b since the effects of one weld on the other may not be negligible.*

A separate model includes the H2 and H3 welds in the TEPCO shroud mockup using dimensions provided in Reference (9). The size and shape of the weld preps are estimated from the drawings and sketches in that reference.

Modeling of Welding Process

Each weld pass is analyzed by a two step process consisting of a thermal analysis to determine the temperature distributions as a function of time and a structural

* An additional fillet weld discovered on an actual River Bend shroud at the H6b location does not appear on the design drawing. It is included for the second set of analyses of the H6a/H6b welds (40 ksi base-metal yield). It is not included in the first H6a/H6b analysis (67 ksi base-metal yield).

analysis to determine the resultant stresses. Because the thermal and structural portions of the problem are independent, the thermal analyses can be performed for all passes before starting the structural analyses. The temperature distributions calculated in the thermal analysis are then imposed as loads for the structural analysis. Further details regarding the thermal and structural analyses are as follows:

Thermal Model. The thermal analysis involves application of thermal boundary conditions followed by simulation of each welding pass. The thermal boundary conditions used in the models are:

1. Convection on all exterior surfaces (5 BTU/hr-ft^2-°F per Reference (6))
2. Assumed heat sinks at the axial ends of the FEA models. This is achieved by holding the nodal temperatures at these boundaries at 70°F.
3. Coupling of all temperatures across the crack line.

Weld passes are simulated by successively "turning on" the elements that make up each weld pass (with the ANSYS "EALIVE" command), applying a uniform heat generation rate to all of the elements in the pass, and then allowing the weld metal and shroud to cool to room temperature. Temperature distributions are calculated at a number of points in time during each weld pass and are saved for use with the structural model. While Reference (4) states that the interpass temperature is allowed to be as high as 350°F for the River Bend 2 shroud, the residual stress state will not be significantly affected by allowing the shroud model to cool to 70°F between passes. Figure H-7 shows a typical plot of internal heat generation rate vs. time. The peak heat generation rate and the times of heat application are adjusted to provide reasonable peak temperatures in the weld pool and HAZ (i.e., approximately 3000-4000°F in the weld and 1200-1800°F at the HAZ boundary).

For the initial River Bend analyses (67 ksi yield strength for all material), the first weld pass is assumed to be located at the root of the larger of the 2 weld preparations at each joint.* All subsequent weld passes for that weld prep are completed, followed by a back gouge from the opposite side (per Reference (4)) and all weld passes from that side. For example, the weld prep on the ID side of

* The one exception is the 67 ksi base-metal yield strength case for weld H6a, for which the ID passes (smaller weld) were completed prior to the OD passes.

the H4/H5 model is larger than the OD weld prep. Thus, all ID weld passes are completed first (from the root radially inward), followed by a single back-gouge pass and then all other OD passes (from the root radially outward). Note that for the H6a/H6b model, the successive passes for each weld are made simultaneously, since it is unclear which weld was fabricated first. Figure H-8 shows the weld passes labeled in order for a typical model.

For the second set of River Bend analyses (67 ksi weld-metal yield strength and 40 ksi base-metal yield strength), etchings of an existing River Bend shroud were available. The weld pass sequences were chosen to match the sequences indicated by the etchings. The resultant sequences are:

Weld	Sequence
H3**	ID/OD
H4 and H5**	ID/OD
H6a	ID/OD
H6b	OD/ID

Two analyses for H6a/H6b were carried out because the sequencing of the fillet weld on the OD of H6b was unclear from the etchings. The first analysis (denoted by "67/40–1") assumes that the fillet weld was added last, after all other H6b passes. The second (denoted by "67/40–2") assumes that the fillet weld is added after the other OD passes but prior to the ID passes.

For the TEPCO model (welds H2 and H3), the welding sequence substantially matches that indicated in Reference (9). For H2, the OD passes are completed first, followed by the ID passes. For the H3 weld, this sequence is reversed. As for the H6a/H6b model, the passes for each weld are made simultaneously. Note that the total number of passes used in the analysis is fewer than the number used in the TEPCO experiments and analysis. No surface cover passes were modeled.

Structural Model. After calculating the temperature distributions for the welding passes, the element and nodal geometry is converted to a structural

** Etchings of H5 were made. H4 and H5 are similar welds and are assumed to have the same pass sequence.

model by changing the PLANE77 thermal elements to PLANE82 structural elements. The following structural boundary conditions are applied:

1. All nodes across the bottom edge of the model are constrained to zero axial displacement. This constraint produces zero rotation at the bottom of the modeled portion of the shroud.

2. All nodes on the top edge of the model are constrained to have the same axial displacement. This constraint produces zero rotation at the top of the model, but permits net axial expansion or contraction.

3. All pairs of coincident nodes across the crack line are coupled in both the radial and axial directions. This effectively "sews" the crack together during the welding process.

Residual stresses are determined by sequentially imposing the temperature distributions at each time step as loads on the structural model and then solving for the resultant stresses. Note that the elements associated with each weld pass are not activated structurally (with the EALIVE command) until the time associated with the end of heat input for these passes. Activating these elements any sooner generates artificial plastic strains in the weld while it is still a liquid.*

Modeling of Post Weld Heat Treatment

Some shroud welds were subjected to a post weld heat treatment for 24–48 hours at 750°F. For welds subjected to this treatment (i.e., the H3, H4, and H6a/H6b welds in the River Bend shroud), the finite element models include an increase in temperature to a uniform 750°F after completion of the welding. This operation has the effect of reducing peak stresses since the 48 ksi weld-metal yield strength at 750°F is less than the 67 ksi room temperature yield strength.

Modeling of Crack Growth

Growth of a crack through the shroud wall can be simulated by releasing the displacement couples between nodes on either side of the crack up to the crack tip. This allows redistribution of the residual stress state as would occur during the formation of a real crack.

---

* In addition, activation of the weld elements prior to the peak of heat-up would cause artificial strains and stresses to be generated in the base metal because the weld metal has significant strength and stiffness at lower temperatures. In an actual welding process, the weld metal will not cause significant forces in the base metal until it begins to gain strength during cooling.

H.3 Analysis Results

Finite element analyses were performed for each of the weld geometries described in Paragraph H.1. The primary results, shown in Figures H-9 through H-13, consist of contour plots of the hoop and axial stress distributions through each cross section and line graphs of hoop stress and axial stress along the inside and outside surfaces of the shroud wall near the welds. For the River Bend models (Figures H-10 through H-13), plots reflect different yield strengths for the base metal and weld metal (room-temperature values of 40 ksi and 67 ksi; see "Material Properties" in Paragraph H.2). For the TEPCO model (Figure H-9), the plots reflect identical yield strength values for the base metal and weld metal (67 ksi). All of the stress contour plots use the same contour scale so that analysis results for each weld location can be easily compared.

The content of these figures is as follows:

Figure No.	Shroud Design	Welds Included
H-9	TEPCO	H2 and H3
H-10	River Bend*	H3
H-11	River Bend*	H4
H-12	River Bend	H5
H-13a	River Bend*	H6a and H6b (fillet last)
H-13b	River Bend*	H6a and H6b (fillet before ID passes)

Observations from these results are as follows:

Content Deleted -
EPRI Proprietary Information

* These models included a uniform heat treatment of 750°F.

Content Deleted -
EPRI Proprietary Information

H.4 Comparison of Calculated and Measured Residual Stresses

In parallel with the analysis effort described in the preceding paragraphs, residual stresses in the vicinity of the welds were measured experimentally on three shroud designs.

Surface Stresses

The first set of experimental data is reported in Reference (9) for the TEPCO shroud mockup. The results of the experimental measurements on this shroud mockup consist of surface stresses, and are plotted on the line graphs in Figure H-9.

Content Deleted -
EPRI Proprietary Information

Content Deleted -
EPRI Proprietary Information

A second set of measurements was taken at Sandia National Laboratories (5) on the Grand Gulf shroud. The Grand Gulf shroud is similar in design, but not identical to, the River Bend design. The results of the experimental tests consist of surface stresses, and are compared to the River Bend FEA predictions on the line graphs in Figures H-10 through H-13 (triangular symbols represent axial stress measurements and circles represent hoop stress measurements). As reported in Reference (5), several measurements of both axial stress and hoop stress were taken at the following locations: a) at the center of each weld, b) in the HAZ of each weld, and c) about 1" from the HAZ of each weld. A comparison of the DEI calculations and experimental measurements shows that:

Content Deleted -
EPRI Proprietary Information

Through-Thickness Stresses

A third series of measurements was carried out on a shroud of the River Bend design. Results include the axial stress distributions for the H5, H6a, and H6b welds along a through-thickness path which is substantially parallel to the radius of the shroud. (This path is nearly the same as that used in the analyses.) The measurements were carried out on segments cut from the shroud. These cuts relieved some of the residual stresses in the shroud which were present prior to the cuts.

Figure H-15 includes a comparison between the experimental through-thickness measurements and the finite element predictions for the axial stress component for these three welds. For welds H5, H6a, and H6b, one experimental curve and two or three analytical curves are included. The analytical curves fall into two categories:

1. The case of differing material yield strengths: 40 ksi for the base metal and 67 ksi for the weld metal. This is the same assumption that is reflected in Figures H-10 through H-13. This curve is labeled "*DEI* FEA (67/40)" on Figure H-15. (Welds H6a and H6b include two curves in this category; they reflect different sequencing of the fillet weld on H6b.)

2. The case of identical yield strengths (67 ksi for all materials). This curve is labeled "*DEI* FEA (67/67)" on Figure H-15.

Content Deleted -
EPRI Proprietary Information

Figure H-15 also includes the axial stress distributions for the River Bend H3 and H4 welds. No through-thickness measurements are available to compare with these curves.

For the TEPCO welds, only one DEI analytical curve is included (Case 2 above – identical 67 ksi yield strengths for both the weld metal and the base metal). On the H3 plot, the corresponding TEPCO FEA is also included for comparative purposes.

* For all of the River Bend welds and the TEPCO H2 weld, the path is located in the base metal below the weld. For the TEPCO H3 weld, the path is located in the base metal above the weld (i.e., in the ring).

H.5 References

1. ANSYS Finite Element Program, Revision 5.1, Swanson Analysis Systems, Inc., 1994.

2. High Temperature Property Data: Ferrous Alloys, Rothman, M.F., consulting ed., ASM International, Metals Park, OH, 1988.

3. "Shroud for River Bend II," Volume I (Material Acceptance), Section IV (Weld Material Certifications), General Electric Co., MPL No. B13-D070, P.O. No. 205-AG572.

4. "Automatic Submerged Arc Welding of P#8 Stainless Steels in Accordance with the ASME Code, Section IX, 1974 Edition," Specification No. WP 75, Sun Shipbuilding & Dry Dock Co., Revision 4, 1976.

5. Fax transmittal from Stan Rosinski (Sandia National Labs) to Steve Hunt (DEI), July 26, 1995.

6. "Analysis Guidelines for Backfill Modification of RPV Water Level Instrumentation," General Electric Company Report No. GENE-637-019-893, Rev. 0, August 1993.

7. "Review of Shroud Cracking Investigation and Repair Program – Brunswick Unit 1," transmitted by Dominion Engineering letter to W.R. Campbell, Carolina Power & Light, October 13, 1993.

8. General Electric Drawing No. 107E5313H, Rev. 0, Sheets 1-2 [marked "Preliminary Print"], August 19, 1994.

9. "Full-Scale Mockup Test Results for H2/H3 Weldments of Core Shroud," Tokyo Electric Power Co., provided for internal use of the BWRVIP, 1994.

10. Fax transmittal from Raj Pathania (EPRI) to Steve Hunt and Marc Kreider (DEI), dated August 4, 1995.

11. ASME Boiler and Pressure Vessel Code, Section II, Part D, American Society of Mechanical Engineers, 1992.

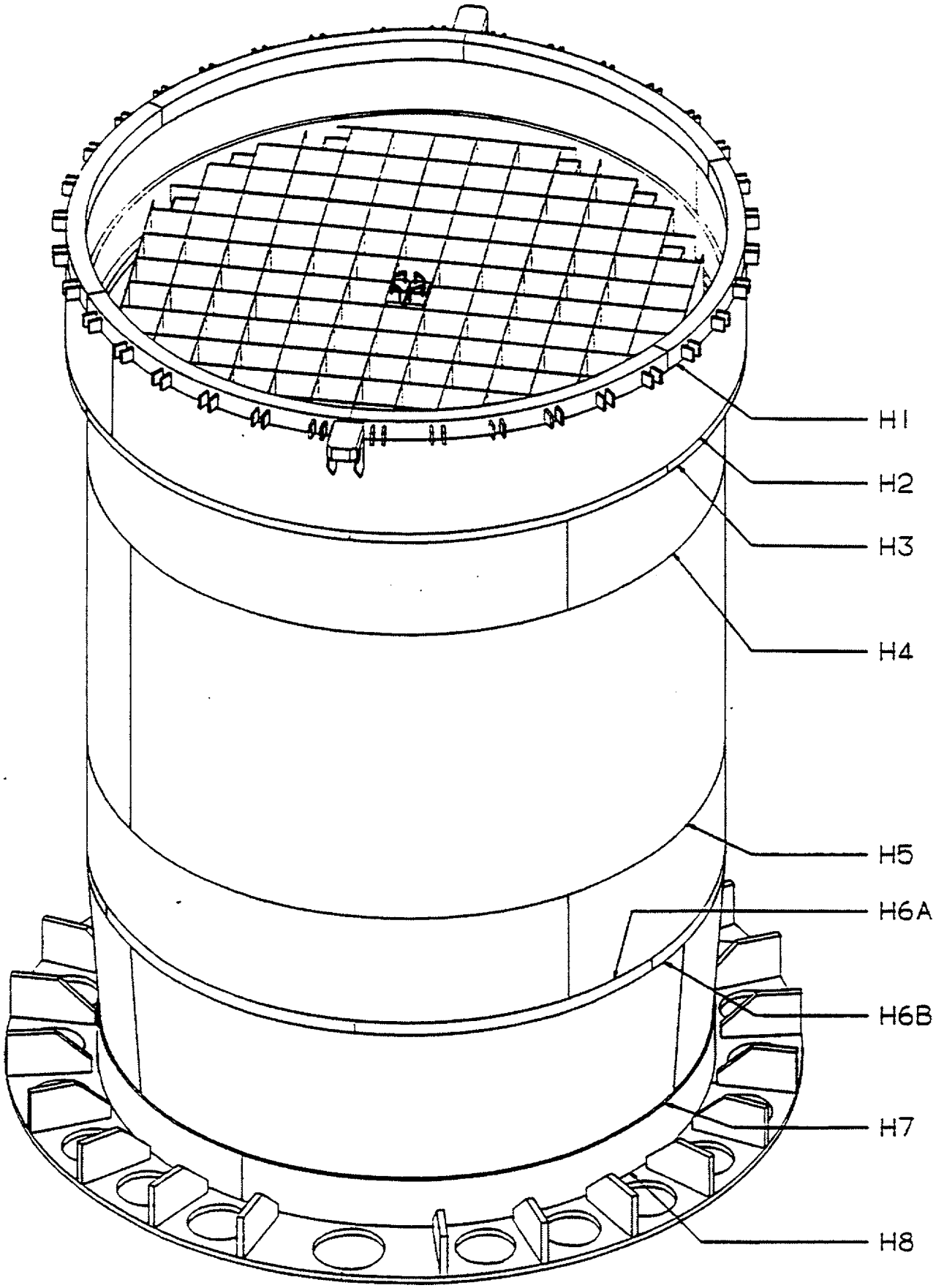

Figure H-1. Typical BWR Core Shroud (Circumferential Welds Labeled)

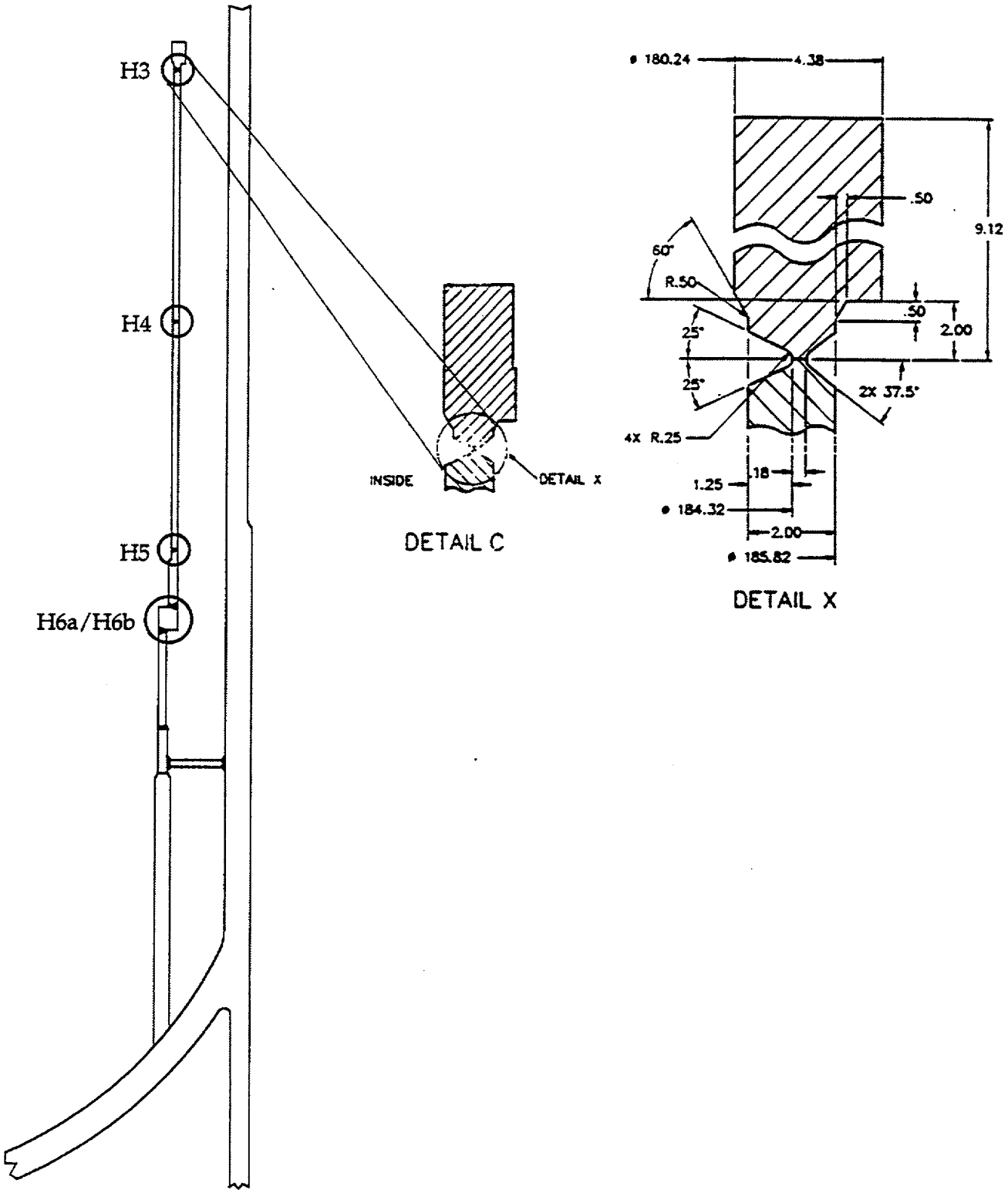

River Bend Shroud

Figure H-2a. Location of River Bend H3 Shroud Weld

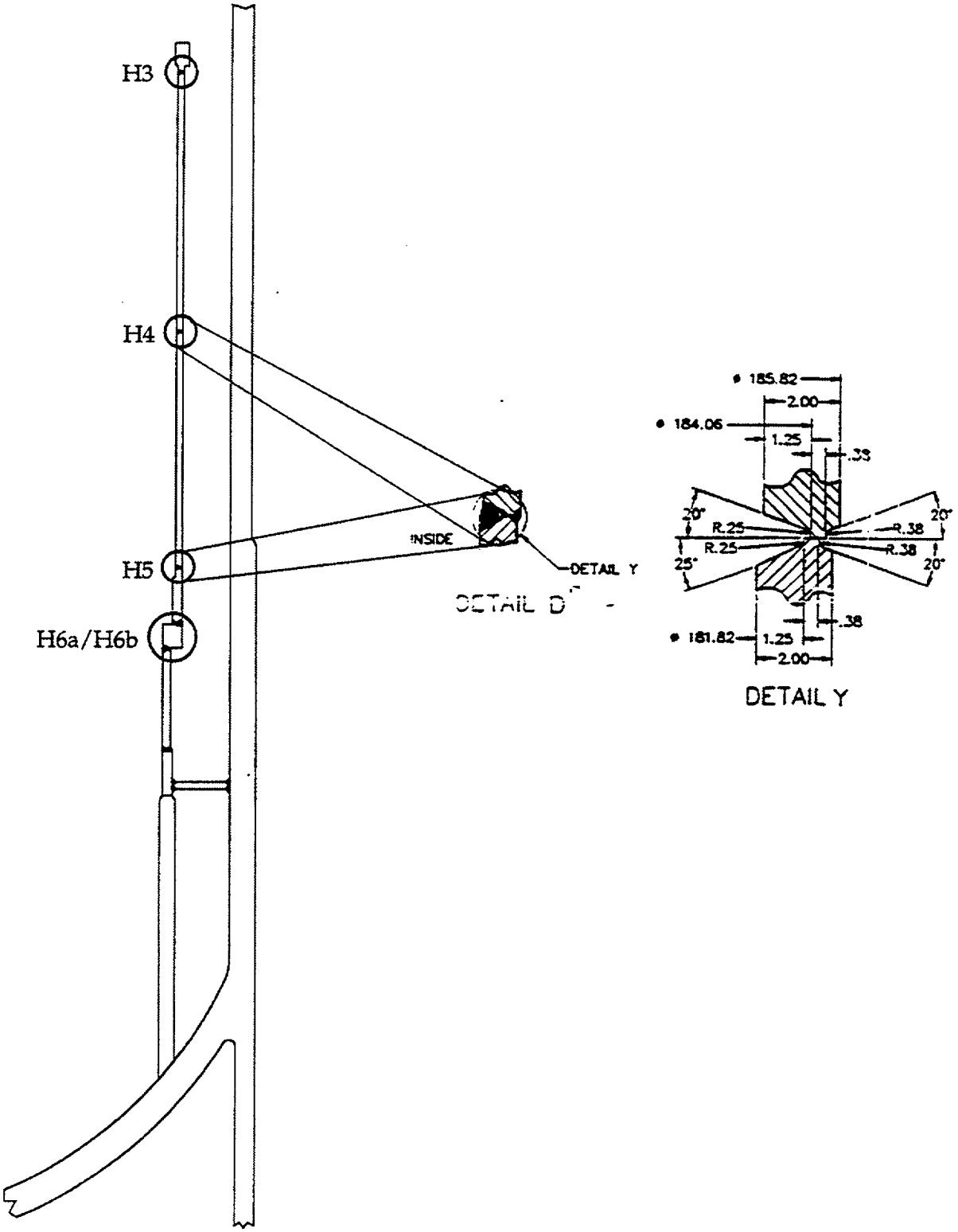

River Bend Shroud

Figure H-2b. Location of River Bend H4 and H5 Shroud Welds

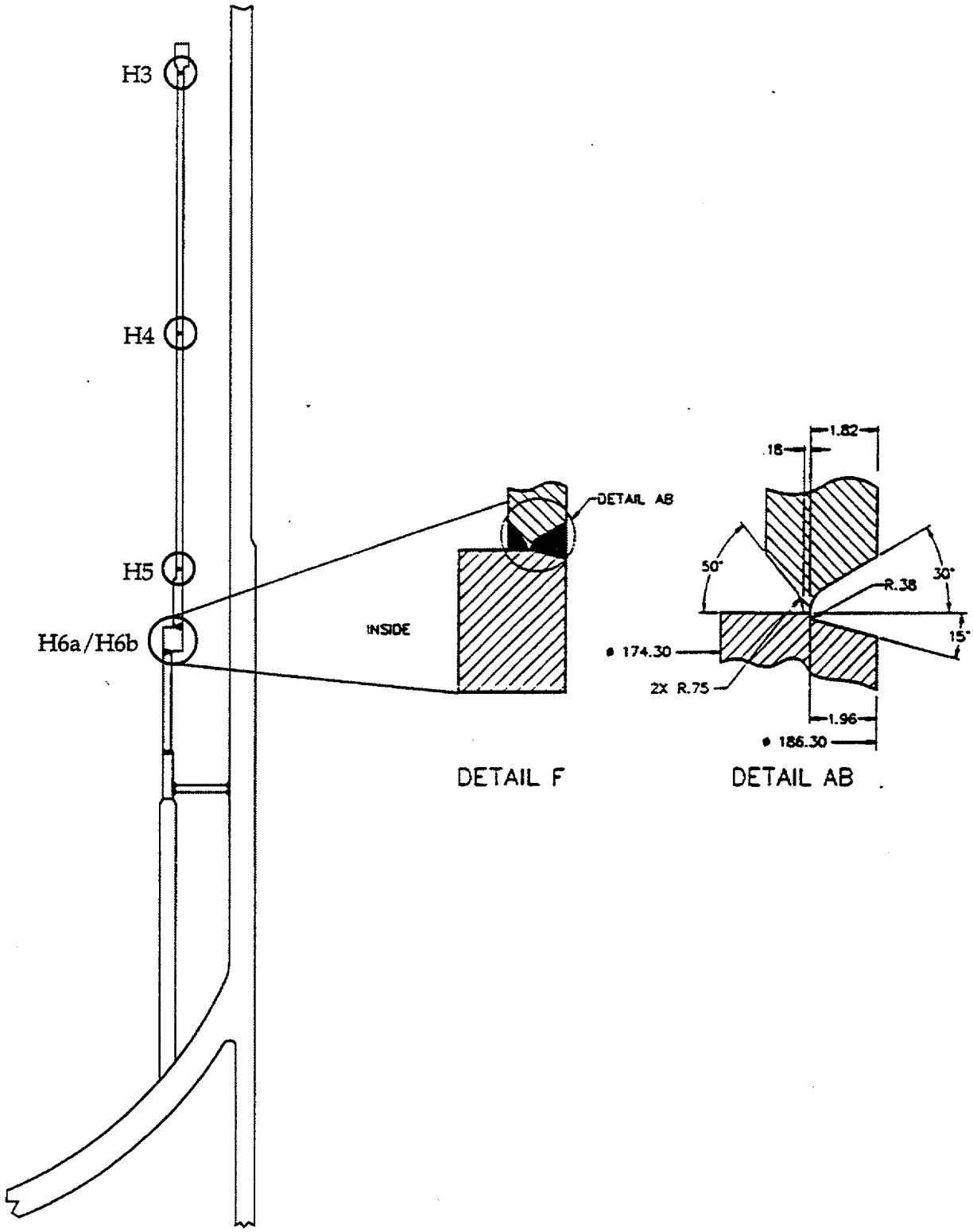

River Bend Shroud

Figure H-2c. Location of River Bend H6a Shroud Weld

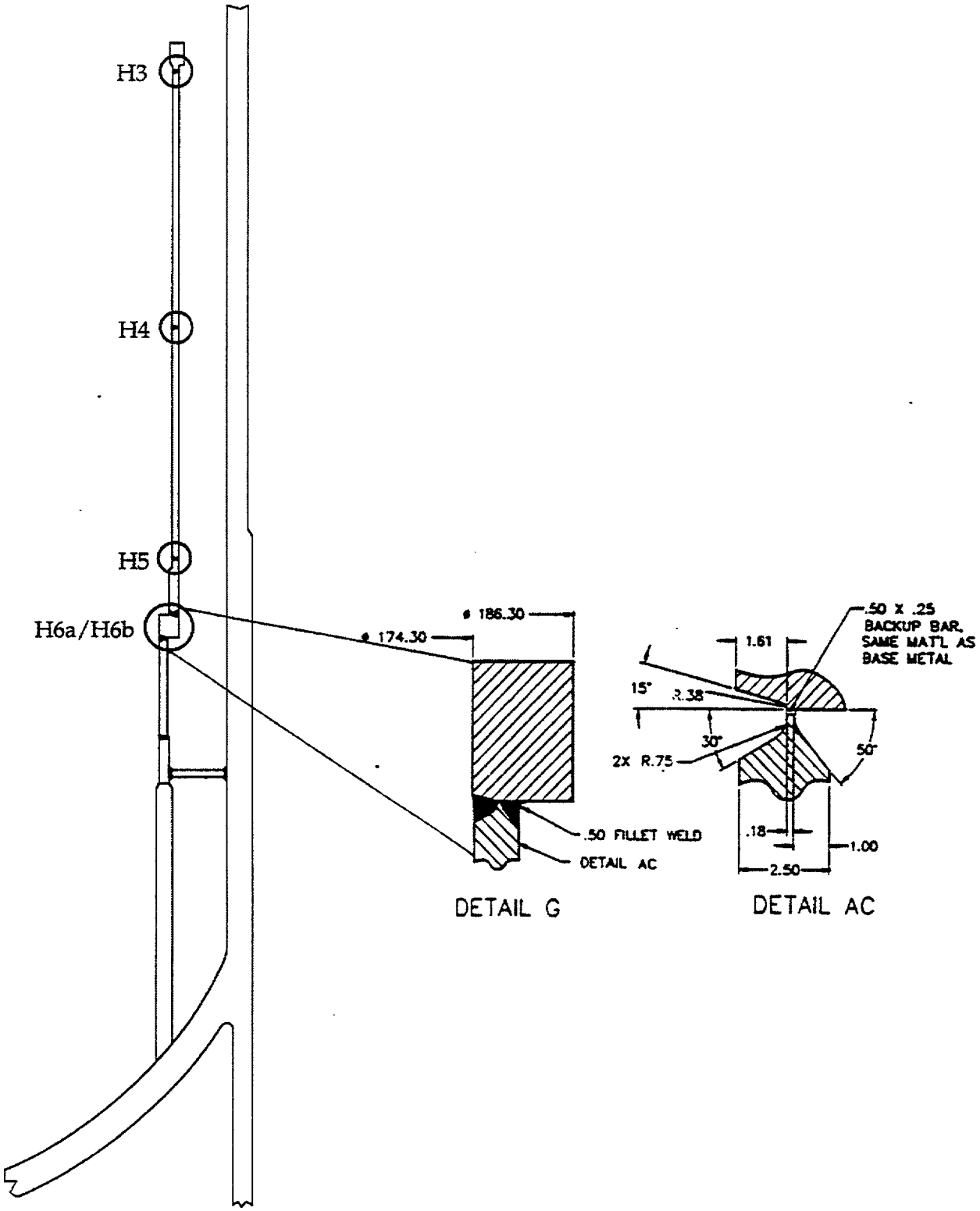

River Bend Shroud

Figure H-2d. Location of River Bend H6b Shroud Weld

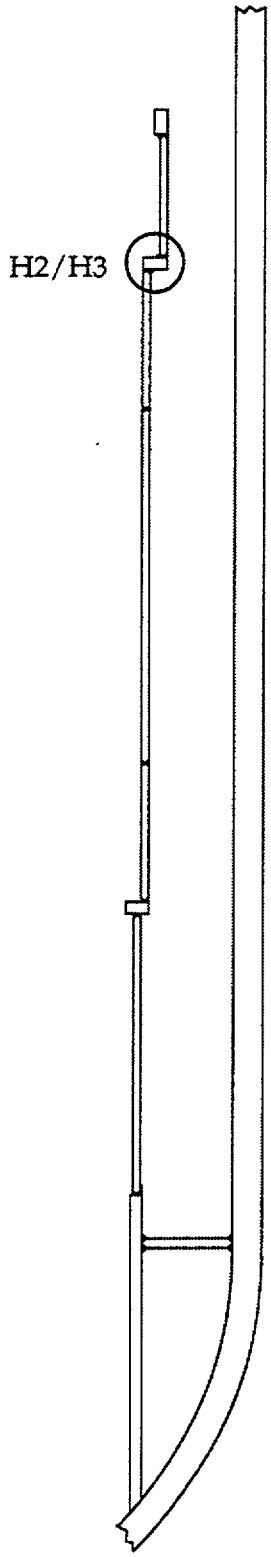

TEPCO Shroud

Figure H-2e. Locations of TEPCO Shroud Welds Analyzed

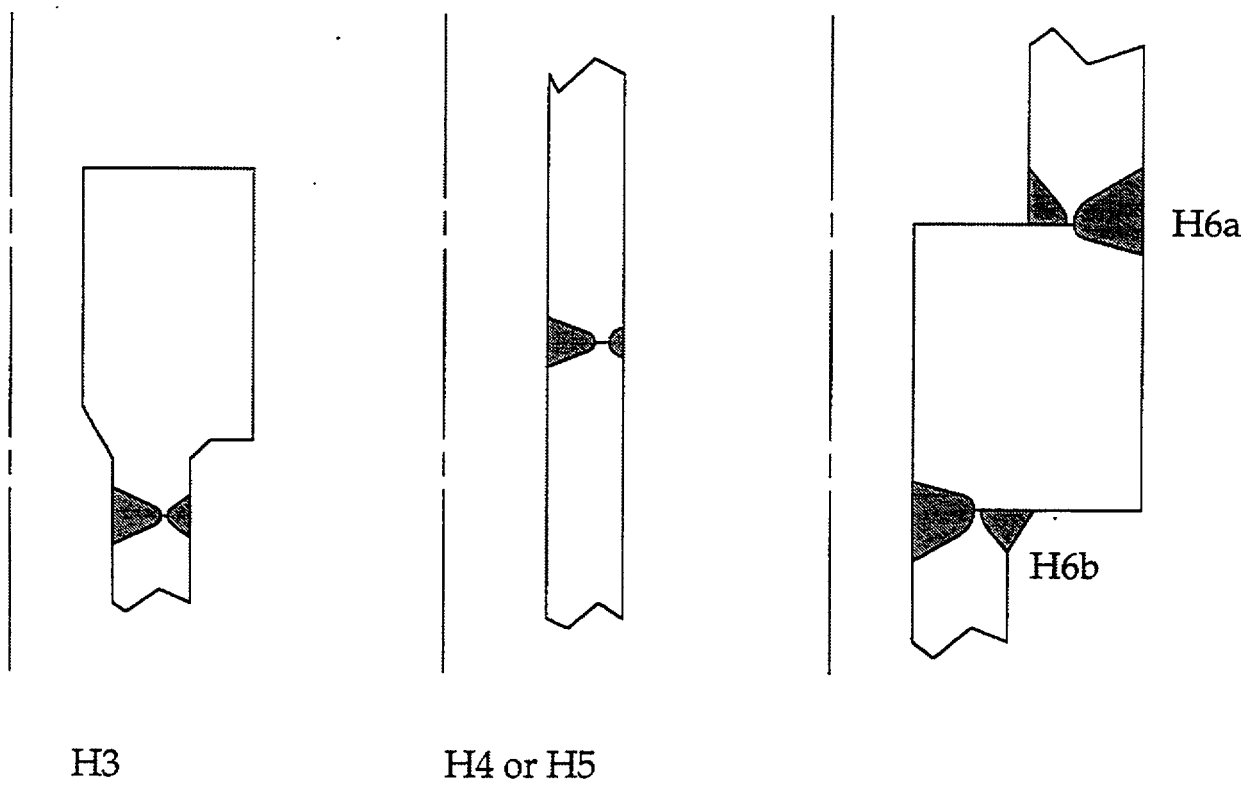

Figure H-3. River Bend Welds Analyzed

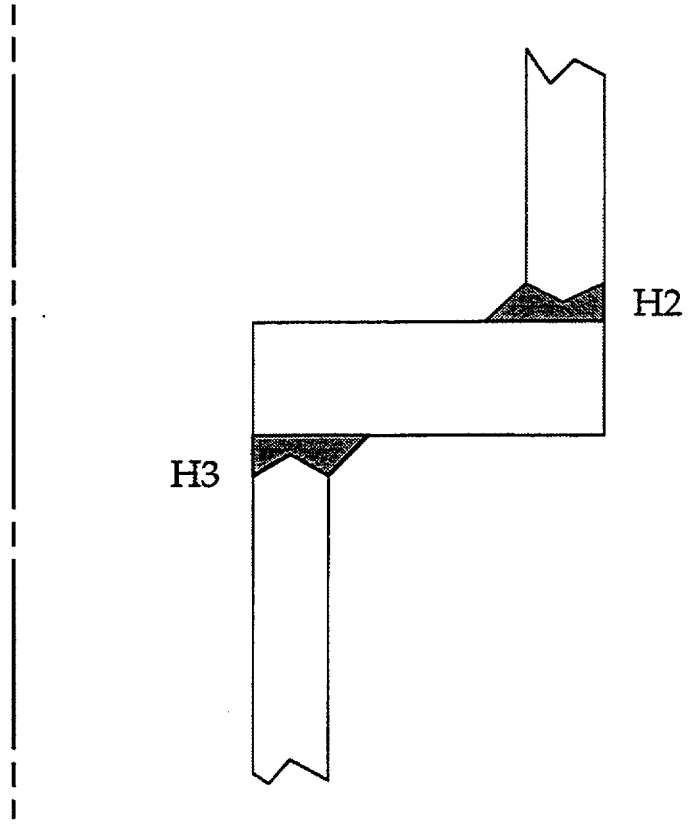

Figure H-4. TEPCO Welds Analyzed

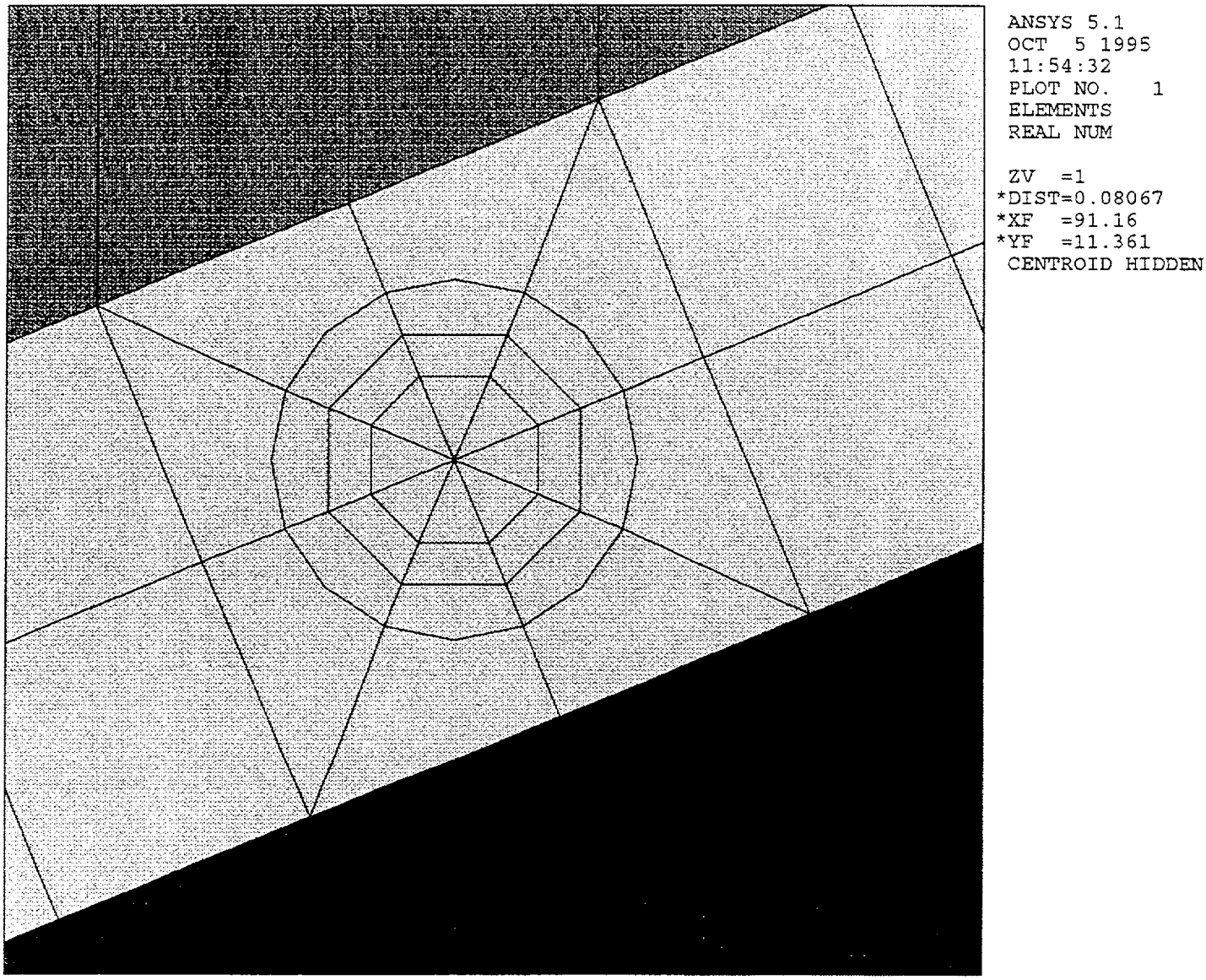

Figure H-5. Mesh Geometry Near a Crack-Tip Location

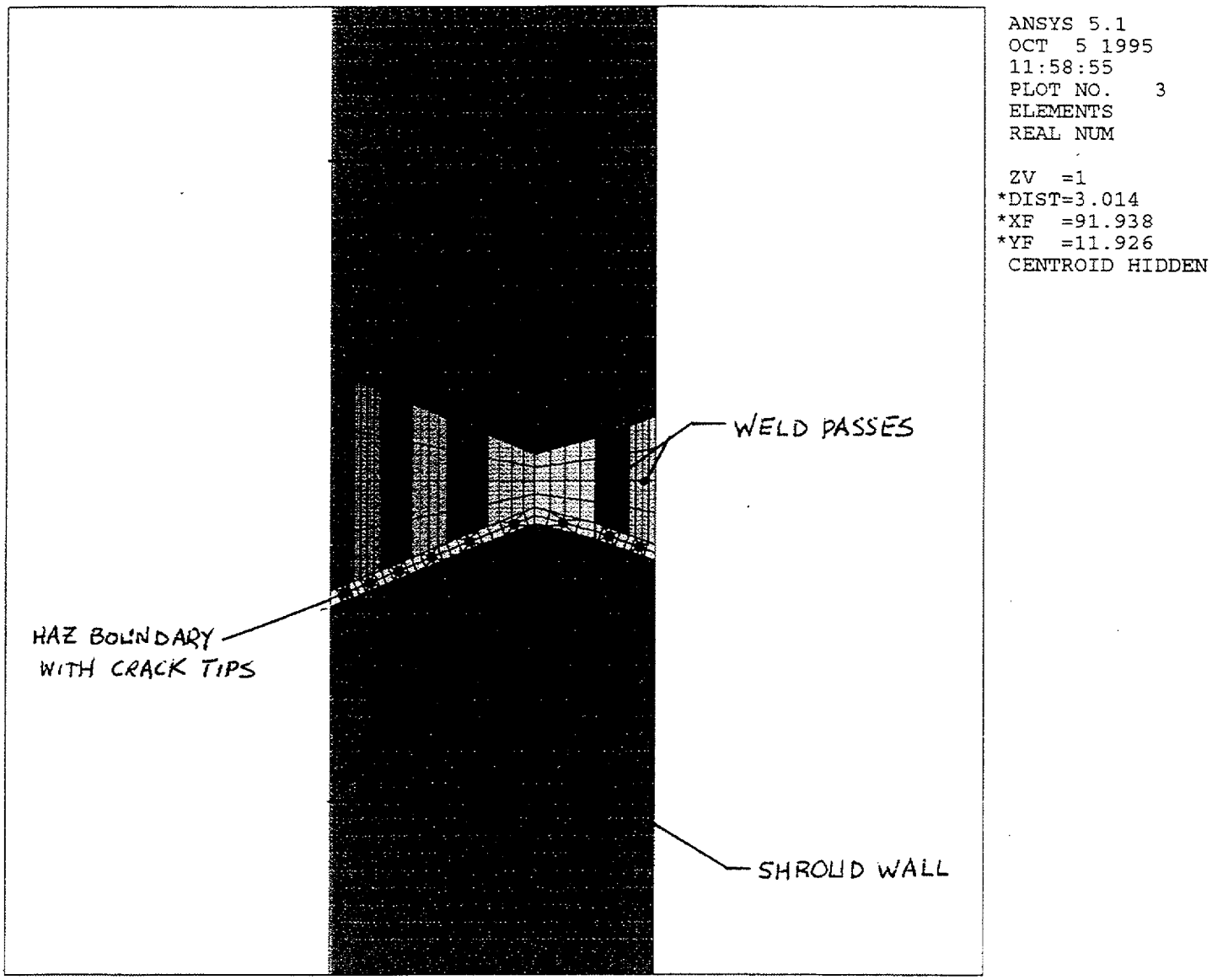

Figure H-6. General Features of Shroud Weld FEA Mesh

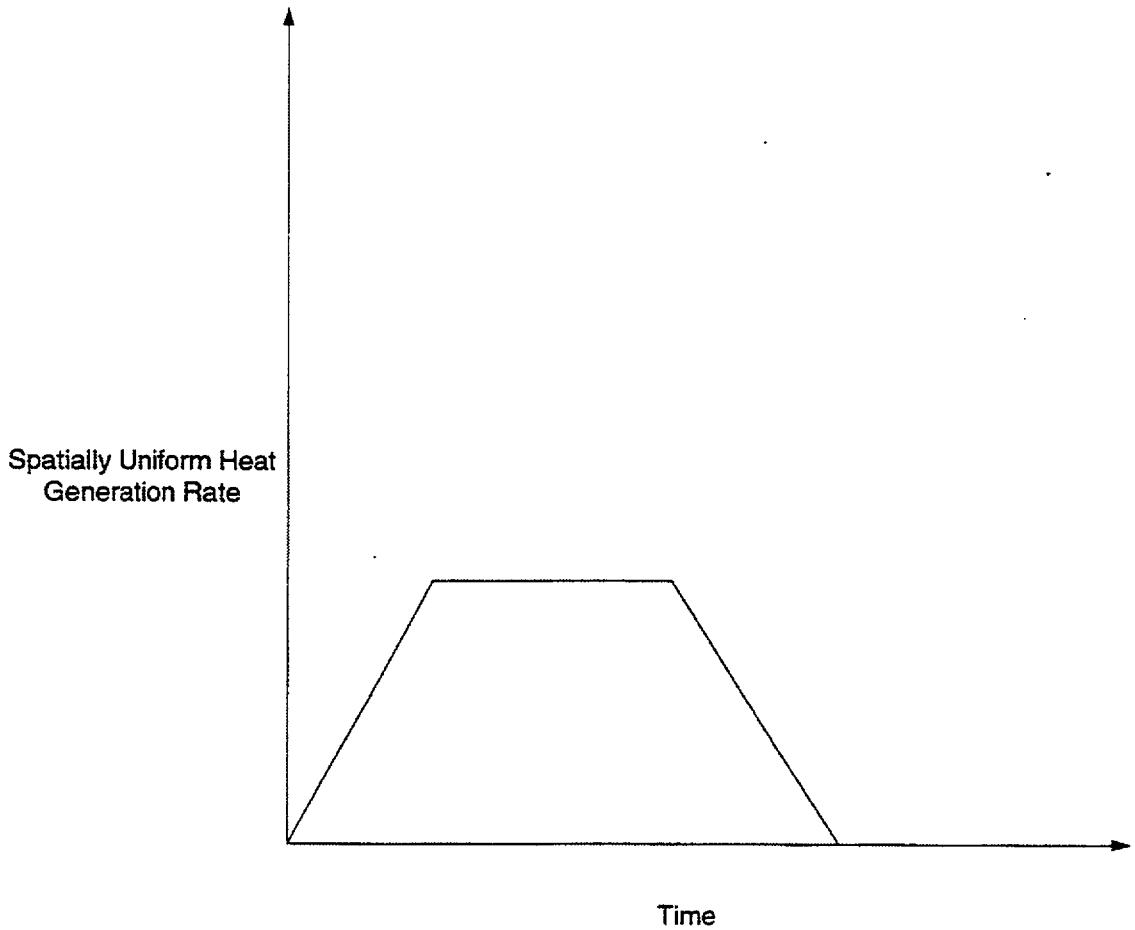

Figure H-7. Heat Generation Rate vs. Time

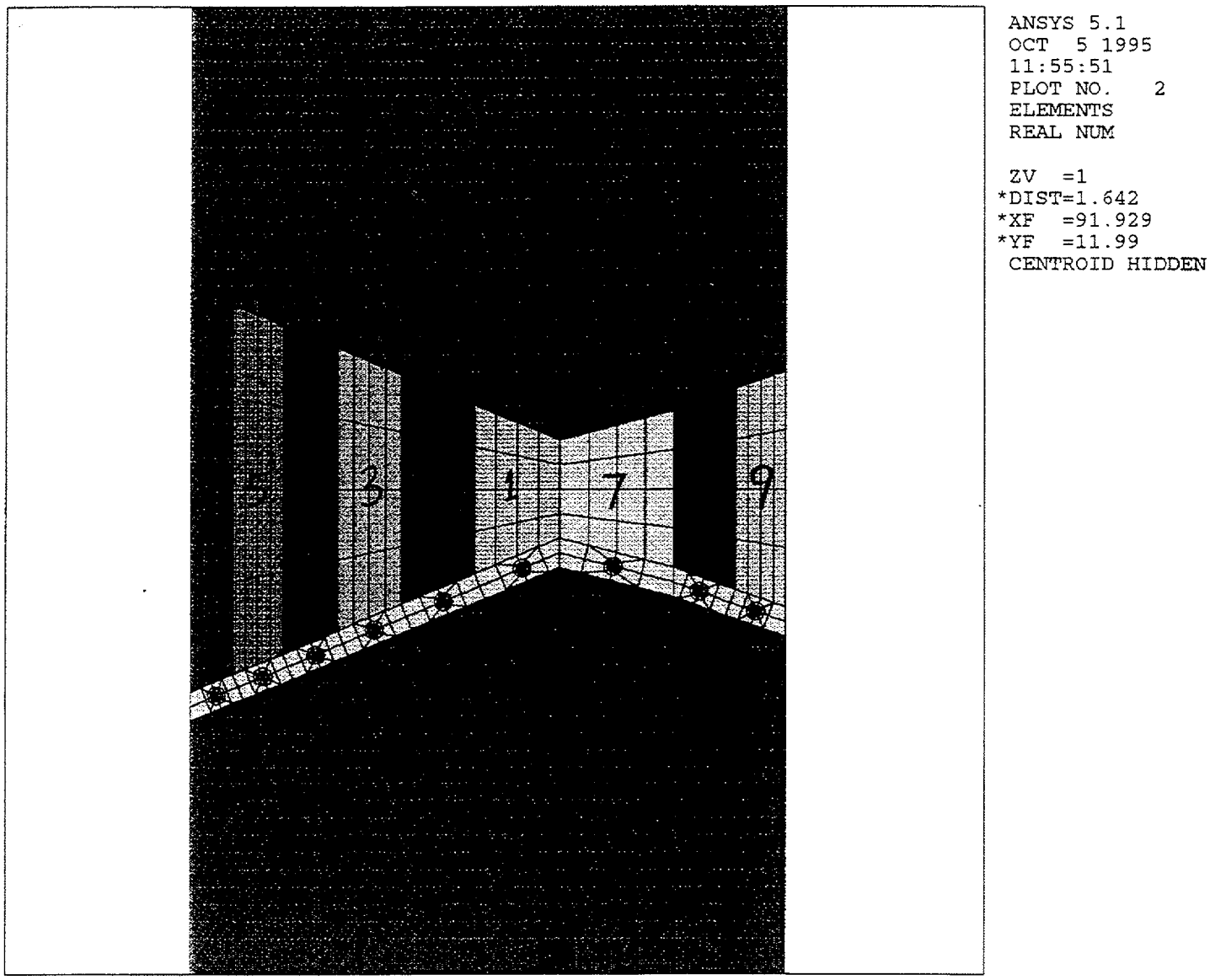

Figure H-8. Weld Pass Numbers (Typical)

APPENDIX I

In-Plant Crack Extension Determination from Successive UT Examinations

Prepared by:

D. E. Delwiche
R. M. Horn
General Electric Nuclear Division

Appendix I

In-Plant Crack Extension Determination From Successive UT Examinations

November 7, 1995

Prepared for the BWRVIP Crack Growth Rate Committee

Prepared by: _____ for
D. E. Delwiche

Prepared by: _____
R. M. Horn

Abstract

This Appendix contains a summary of the crack growth data that was derived from two different UT reinspections of shroud welds from actual operating BWRs. Specifically, the data covers the inspections from two different overseas plants. The data that was reviewed for KKM covers the period from 1990 through 1995. The welds which have IGSCC indications and in turn were re-inspected are welds #4, the #3 shroud location and #11, the #4 shroud location. The usable data for the purposes of the crack deepening assessment were taken in the last two inspections, 1994 and 1995.

The second plant that was inspected was Chinshan, Unit 2. The inspections available were the 1994 and 1995 inspections of the #3 shell weld heat affected zone. This information was also used to determine crack deepening estimates for the crack growth modeling efforts.

The following Appendix contains background information on the data used in the crack growth assessment , the methodology used to determine the crack growth rates for the established cracks on the welds that were inspected, and the data summaries. It should be recognized that the data is customer sensitive and that the crack growth data is based on an engineering assessment of reported the UT data.

1

Crack Growth Rate Determination Methodology

To calculate rates for crack deepening, a methodology needed to be applied to the UT inspection data. It must be recognized that the UT estimates of the crack depth have uncertainty. It must also be recognized that there is a finite detection limit of UT for shallow, newly initiated crack indications. Finally, for IASCC, cracking can be branched and there can be parallel segments of cracking. These features complicate the ability to directly compare the entire UT information from one cycle to a subsequent cycle. The best approach for comparison is to assess crack growth in the regions that had UT reported depths in both the initial and the subsequent inspection. Any azimuthal location where there was no previous UT recorded flaw was disregarded in the crack growth deepening assessment.

The crack growth in depth was viewed two ways for the KKM data. This was possible because the discrete UT depths were available (and are included) as a function of azimuthal position. First, an average crack growth over the cycle was calculated. This estimate included the net changes in UT derived depth. Secondly, an average of the crack deepening was evaluated for only the active segments of the crack, those segments that displayed positive growth. This second measurement approach reinforced the average calculations and as such were not included.

For the Chinshan data, there were several indications that were evaluated with UT. The average growth was derived from the average of all the segments. In that some of the indications displayed active growth, these crack growth amounts are also tabularized. However, this estimate did not make use of all the individual UT measurements in the way they were used for the KKM data.

2

KKM Re-inspection Data

The data in the following sections was measured for two welds, #4 at the H3 location, and #11 at the H4 location. The H4 weld in is the beltline region and subjected to high fluence. It should be noted that a boat sample from the #11 weld established that the weld heat-affected zone was not sensitized due to the moderate carbon content and as such the weld cracking could be attributed, in part, to IASCC. A history of the inspection results follows.

2.1 1990-1992 Results

Two types of inspections were performed; visual (VT) and ultrasonic (UT). Visual inspections were performed in 1990, 1991, and 1992. Ultrasonic inspections were performed in 1990 and 1992. None of the inspections performed included direct measurements of crack length. Direct measurements were not within the capability of the processes and/or tooling that were utilized.

Content Deleted -
EPRI Proprietary Information

Content Deleted -
EPRI Proprietary Information

2.2 UT Examination in 1993 and 1994

Weld 11, at the H4 beltline region was inspected ultrasonically in 1993. In 1994, Weld 4, at the H3, was inspected and the Weld 11 was re-inspected. In 1994, Weld No. 4 was inspected for 81% of the weld length and visually inspected for the limited areas, thereby confirming the presence of cracking detected by UT.

Content Deleted -
EPRI Proprietary Information

2.3 1995 Re-inspection of Welds 4 and 11 (H3 and H4)

Content Deleted -
EPRI Proprietary Information

Figure 2-2 displays the locations of the cracks on #4 and #11, along with the indications on other welds, first inspected in 1995.

Figures 2-3 and 2-4 display the cross sections of the indications on Weld 4. Figures 2-5 and 2-6 display the same cross-sections with overlays of the 1994 UT results. Table 2-1 gives the azimuthal data associated with the 1994 and 1995 depth data.

Figures 2-7, 2-8, and 2-9 display the indications on Weld 11. Figures 2-10 through 2-12 display the comparisons with 1994 for the same indications. Table 2-2 gives the 1995 UT depth data as a function of azimuth.

Table 2-1. KKM Shroud Weld #4 - 1995 Examination (1994 to 1995 Comparison)

Content Deleted -
EPRI Proprietary Information

Table 2-2. KKM Shroud Weld #11 - 1994 and 1995 UT Examinations (Indication Position and Thru-wall Measurements)

Content Deleted -
EPRI Proprietary Information

Table 2-2. KKM Shroud Weld #11 - 1994 and 1995 UT Examination (Indication Position and Thru-wall Measurements) (Continued)

Content Deleted -
EPRI Proprietary Information

Content Deleted -
EPRI Proprietary Information

Figure 2-2 KKM Shroud - 1995 Examination

Figure 2-3 KKM - Shroud Weld #4 - Area 1 - Indication 1

Content Deleted -
EPRI Proprietary Information

Figure 2-4. KKM Shroud Weld #4 - Area 2 - Indication 2

Content Deleted -
EPRI Proprietary Information

Figure 2-5. KKM Shroud Weld #4 - Area 1 - Indication #1

1994 to 1995 Data Comparison

Content Deleted -
EPRI Proprietary Information

Figure 2-6. KKM Shroud Weld #4 - Area 1 - Indication #2

1994 to 1995 Data Comparison

Content Deleted -
EPRI Proprietary Information

Figure 2-7. KKM Shroud Weld #11 - Area 1 - Indications #1, 2 & 3

Thru-wall Rollout Map - 1995 Examination
60° RL & 45° Shear Data
Most Conservative Length & Thru-wall

Content Deleted -
EPRI Proprietary Information

Figure 2-8. KKM Shroud Weld #11 - Area 2 - Indications #4 & 5

Thru-wall Rollout Map - 1995 Examination

60° RL & 45° Shear Data

Most Conservative Length & Thru-wall

Content Deleted -
EPRI Proprietary Information

Figure 2-9. KKM Shroud Weld #11 - Area 3 - Indication #6

Thru-wall Rollout Map - 1995 Examination

60° RL & 45° Shear Data

Most Conservative Length & Thru-wall

Content Deleted -
EPRI Proprietary Information

Figure 2-10. KKM Shroud Weld #11 - Area 1 - Indications #1, 2 & 3

1994 to 1995 Data Comparison

Content Deleted -
EPRI Proprietary Information

Figure 2-11. KKM Shroud Weld #11 - Area 2 - Indications #4 & 5

1994 to 1995 Data Comparison

Content Deleted -
EPRI Proprietary Information

Figure 2-12. KKM Shroud Weld #11 - Area 3 - Indication #6

1994 to 1995 Data Comparison

Content Deleted -
EPRI Proprietary Information

3

Chinshan Unit 2 Re-inspection Data

The shroud material for Chinshan Unit 2 was manufactured using Type-304L stainless steel. The inspection information and associated growth rates are given in the next sections.

3.1 1994 UT Inspection Data

In 1994, examinations were performed on the Chinshan Unit 2 reactor core shroud using an OD suction cup automated scanner. The examination areas requested for inspection were the H3 weld from 215° to 360° and three areas on the 180° side (15°, 105° and 160°). Twenty-two individual scans were performed on the H3 weld (Table 3-1).

Content Deleted -
EPRI Proprietary Information

3.2 1995 UT Re-inspection

During February and March 1995, the shroud was inspected again. This was a more comprehensive exam, with Welds H1 through H7 being inspected. The H3 weld was re-inspected, allowing comparison with the 1994 results. Table 3-3 displays the location of the indications and the length and depth associated with each of them. The Figures 3-1 through 3-3 overlays the 1994 and 1995 UT depth information for the 210°-240° segment, the 245° to 270° segment, and the 270° to 300° segment of H3 of the shro

Content Deleted -
EPRI Proprietary Information

Table 3-1. H3 Weld Volumetric Inspection

Content Deleted -
EPRI Proprietary Information

Table 3-2. Chinshan-2 EOC 13 Shroud Weld H3 Indication Data

Content Deleted -
EPRI Proprietary Information

Table 3-3. Comparison of H3 Indications Between EOC-12 and EOC-13

Content Deleted -
EPRI Proprietary Information

Figure 3-1. Chinshan Unit 2 - Shroud Weld H3 ID Crack Map

Content Deleted -
EPRI Proprietary Information

Figure 3-2. Chinshan Unit 2 - Shroud Weld H3 ID Crack Map

Content Deleted -
EPRI Proprietary Information

Figure 3-3. Chinshan Unit 2 - Shroud Weld H3 ID Crack Map

Content Deleted -
EPRI Proprietary Information

4

Crack Growth Rates

4.1 KKM: 1994 to 1995

Based on the data presented, the following average crack growths were calculated for each of the indications on welds #4 and #11. The results are summarized below. The average conductivity was 0.106 μS/cm.

Content Deleted -
EPRI Proprietary Information

4.2 Chinshan, Unit 2: 1994 to 1995

For Chinshan, the azimuth data is more limited. Therefore, the average rate represents the average of all the indications. The other 4 values represent the active indications based on the inspection report. One active indication is not listed in that it was not present in the 1994 inspection, indication 9. For this unit, a review of the conductivity data led to the following general information. The average cycle conductivity was ~ 0.129 μS/cm with the first month ~0.18, the second month ~0.14, months and the subsequent months ~0.13 μS/cm.

Chinshan, H3 location: Cumulative Average Growth (excluding Indication 9) :

Content Deleted -
EPRI Proprietary Information

4.3 Interpretations: KKM Data

The UT-determined crack growth data can also be viewed to support the methodology and crack growth approaches that have been presented in this report. Specifically, the limited data on Weld 4 (H3) location and Weld 11 (H4) location can be used to determine if the IGSCC exhibited reduced crack growth rate with increased depth during the cycle of operation. To perform this evaluation, the data was viewed in an alternate form. The UT-determined minimum 1994 depth and the 1995 maximum depth were used as a range for sorting the UT-determined 0.1 degree segments in three initial depth regions from which the crack grew radially through the shroud HAZ. This was done with the recognition that there are definite uncertainties associated with the derived depths. The evaluation also did not make any distinction between welds, even though the H4 weld is at a significantly higher fluence.

Content Deleted -
EPRI Proprietary Information

CRACK GROWTH vs. DEPTH

Content Deleted -
EPRI Proprietary Information

Figure 4-1

APPENDIX J

Plant-Specific Crack Extension Calculations - Comparison with the Empirical Model

Prepared by:

M. L. Pytel
N. G. Cofie
A. J. Giannuzzi
Structural Integrity Associates, Inc.

APPENDIX J
Plant-Specific Crack Extension Calculations -
Comparison with the Empirical Model

INTRODUCTION

There are limited consecutive outage UT inspection data available from operating BWRs to compare against crack growth model predictions. Three plants that have made available their successive cycle UT data are Brunswick, Chinshan, and Muehleberg (KKM). The latter two are operating under an NWC environment, and Brunswick is operating with HWC. Specific water chemistry data in the form of daily conductivity and hydrogen injection rates are available only for Brunswick. Weld residual stress as related to the crack driving stress intensity factor has been generalized for the six cracking configurations presented in Section 4 of the main body of this report. The crack growth rate correlation assumes that both the Type 304 and 304L materials are weld-sensitized. In the data set used to develop the crack growth rate correlation, changes in EPR did not have a significant effect on the crack growth rate (Section 3 of main body).

Crack extension calculations contain the assumptions associated with crack length and depth changes which have been used in this evaluation, and are compared to the UT determined crack growth changes reported at these three operating plants. The operating plant results and comparison to the crack growth model are presented in the paragraphs below.

Brunswick

The Unit 1 core shroud at the Brunswick Steam Electric Plant was inspected ultrasonically during refueling outages 9 and 10 [J-1]. The results for both inspections are presented in Table J-1. The two inspections were performed by different UT organizations. Consequently, some differences in results could be expected.

Content Deleted -
EPRI Proprietary Information

Conductivity data between RFO 9 and 10 was provided by CP&L on an almost daily interval. The concentrations of chloride and sulfate were also measured during this time period. The purpose of their data collection was to assemble the information required to evaluate conductivity changes which might contribute to accelerated crack growth. These changes are particularly noteworthy since

HWC was utilized during cycle 10. In evaluating the crack growth rate changes, it was conservatively assumed that all conductivity increases are due to sulfate.

The electrochemical potential has never been measured at a core shroud weld in an operating BWR. Models which predict the concentrations of oxidizing species at various locations around a BWR primary coolant loop have been bench-marked against locations where measurements have been made. The GE/Harwell radiolysis model [J-2] is one such code and its prediction has been used in this project to estimate the ECP for shroud OD and ID welds. This type of modeling provides a means for estimating the effect of hydrogen injection on ECP, as well.

Feedwater hydrogen injection rates were provided by CP&L.. This information can be used to indicate the level of ECP suppression due to the hydrogen. Review of HWC mini test data [J-3, J-4, J-5, and J-6] revealed that approximately 0.3 ppm hydrogen in the feedwater corresponds to an injection rate of 6-10 SCFM used by most plants. The GE/Harwell model provides ECP results for regions around the coolant loop as a function of feedwater hydrogen concentration providing the ultimate conversion from ppm hydrogen to mV(SHE).

Two locations in the Brunswick Unit 1 shroud were chosen for modeling of crack extension, H1 OD and H5 ID. ECP results as a function or feedwater hydrogen concentration for these two locations taken from Reference J-7 are plotted on Figure J-1. A curve-fit provides a continuous function for ECP as related to feedwater hydrogen concentration. Equation coefficients for each of the two locations are presented in Table J-2. The maximum and minimum potential experienced at the H1 OD are +131 and -155 mV(SHE), respectively. These values for H5 ID are +107 and -445 mV(SHE), respectively.

Residual stress for these two locations can be determined from the normalized values presented in Section 4 of this report. The Brunswick core shroud barrel is 1.5" thick from H1 to H7 [J-8]. Figure J-2 shows the stress intensity as a function of crack depth for this shroud thickness.

Content Deleted -
EPRI Proprietary Information

Utilizing this data, discrete integration points for crack growth were established. The integration was maximized by merging the time points where conductivity and hydrogen injection rates were measured. Values or time points, where one, but not the other, measurement was available, were produced by interpolation, or by use of the previous value. The previous value approach was also used for ECP and conductivity when determined by interpolation.

Approximately 1370 integration time points resulted from this evaluation and the CGR at each of these points was calculated. Figures J-3 through J-5 present the stress intensity, conductivity, and ECP during the time where cracks were growing for the H1 shroud OD weld. Superimposed on each

of these plots is the crack depth. These same plots presented for the H5 shroud ID weld are in Figures J-6 through J-8. Table J-3 summarizes the crack extension modeling results and the comparative values of extension reported by successive UT measurements.

Chinshan

General Electric evaluated successive UT measurements taken at Chinshan resulting from an 11-month cycle. Appendix I documents the analysis performed to estimate crack growth for thirteen observed indications. The initial depth and crack extension associated with these indications are listed on page I-30. These results average the growth of indications 7, 8, 10-19, and 23.

All of the indications reported by GE were ID surface connected and associated with the H3 core shroud weld. The configuration for this weld is a shell-to-ring ID connected configuration. Section 6 contains a description of the fracture mechanics approach used to develop the generic stress intensity versus crack depth which was utilized for this configuration. The thickness on the Chinshan core shroud below the H2 weld is 1.5" [J-9]. Figure J-2 presents the stress intensity for a 1.5" thick core shroud that was used to grow the Chinshan indications in the modeling effort.

The average reported conductivity during this operating interval (11 months) was 0.129 μS/cm. For the crack growth calculation presented here, the conductivity for the first three months varied as 0.18, 0.14 and 0.13 μS/cm, respectively. Subsequent months were reported using the average reported conductivity.

The ECP was estimated from the GE/Harwell model [J-7]. Figures J-9 and J-10 present the ECP for the shroud ID and OD. The outer core bypass region ECP results presented in Figure J-9 demonstrate that the ECP varies along the length of shroud, starting from the bottom of active fuel to the top of active fuel. The downcomer region represents the shroud OD environment. The fraction lengths represented by zero and one correspond to top of shroud head dome and top of jet pump/wall shroud support plate. The ECP variation along the shroud OD between these two points are shown in Figure J-10. For the purpose of this analysis, the ID ECP will be assumed to be 105 mV(SHE), and the OD will be considered to have an ECP of 150 mV(SHE) based upon the data presented.

A monthly integration interval was arbitrarily chosen for this analysis because of the lack of detailed water chemistry data. There is a need to integrate over time to account for the changes in stress intensity associated with a crack growing in a residual stress field. Sensitivity studies have shown that the percentage difference in using a monthly integration period as compared to a daily integration is 1.8%. This percentage difference increases to 25% when the time integration period is set to a full cycle. This disparity illustrates the conservative nature of simplistic crack extension calculations that extrapolate a single CGR over long time periods.

KKM

General Electric documented an analysis performed on UT data taken from the core shroud welds at KKM to estimate the crack extension during one operating interval as presented in Appendix I of this report. The results of that analysis for seven indications are presented on page I-29. Two of the indications are associated with the H3 weld and five are for H4.

Stress intensity values to be used in modeling the crack growth were determined from the generalized residual stress and fracture mechanics calculations as documented in Sections 5 and 6. Figures J-11 presents the assumed stress intensity for this 1.22" thick shroud being considered here [J-10].

A single value for conductivity is provided in Appendix I for KKM. This average value is 0.106 μS/cm. The single value was used throughout the 11-month cycle during the time when crack extension was measured. The ECP was not well characterized for the KKM shroud. Therefore, the same ECP described above for Chinshan was used for KKM. This value is 200 mV(SHE) for the ID shroud weld locations.

Summary of Results for the Three Plants

The cracking, characterized by UT for the Brunswick Unit 1 core shroud horizontal welds, is summarized in Table J-1 for two sequential inspections.

Content Deleted -
EPRI Proprietary Information

The results of the crack extension calculations for both Chinshan and KKM are listed in Table J-3 along with a summary of the UT estimates provided by GE in Appendix I. Table J-4 provides an example of the supporting crack growth data used in the empirical modeling of both Chinshan and KKM. Specific data for each indication outlined in Table J-3 was used for their respective calculations.

Discussion

There are several factors which should be considered when comparing the calculated crack extension results from this empirical model with the UT estimated results. The first conservatism is the 95th

percentile placed on the calculated mean crack velocity for a given flaw using the model. This shift produces an estimated crack growth rate which is 10.3 times greater than the best-fit model predicts. The results are therefore the conservative, accelerated estimates of crack extension. Another conservatism is that conductivity changes are caused by anions less aggressive than sulfate, which is included prominently in the model database.

In addition, the UT crack length change estimates vary in their level of conservatism from plant to plant and location to location. The most realistic value is that provided for the H1 OD connected indication. The most conservative values are those calculated by GE in Appendix I.

Content Deleted -
EPRI Proprietary Information

It is also noteworthy that cracks tend to grow erratically from an existing crack front. Crack branching and arresting complicate the characterization of depth changes.

Content Deleted -
EPRI Proprietary Information

Content Deleted -
EPRI Proprietary Information

Conclusions

Crack extension calculations specific to three operating BWRs were performed to evaluate and compare the crack extension predicted by the empirically based stainless steel crack growth rate correlation developed in Appendix C with successive UT measurements made at those plants. Several conclusions can be made from the work presented in this Appendix.

Content Deleted -
EPRI Proprietary Information

References

J-1 R. Steckel, Unit 1 Core Shroud Evaluation Based on B110R1 Inspection Results, ESR 95-00765 Evaluation-Revision 2.

J-2 C. P. Ruiz, C. C. Lin, R. N. Robinson W. G. Burns, and A. R. Curtis, "Model Calculations of Water Radiolysis in BWR Primary Coolant," Paper No. 33, Water Chemistry of Nuclear Reactor Systems 5. BNES, London, 1989.

J-3 "BWR In-Vessel Chemistry and SCC Data for Hatch", Task A, Progress Report, February 1995.

J-4 G. Contreras, R. Head, M. Indig, "In-Core Response to Hydrogen Water Chemistry at J. A. FitzPatrick Plant", ESEERCO Report EP89-32, Final Report, January 1992.

J-5 W. Miller, R. Head, M. Indig, "Measurements of In-Core Recirculation System Response to Hydrogen Water Chemistry at the Duane Arnold Energy Center", EPRI TR-102310, Final Report, April 1993.

J-6 "Quad Cities 2 In-Reactor Stress Corrosion Monitoring Test Results", Task A, Presentation to CRIEPI and Japanese BWR Utilities, by GE Nuclear Energy, December 16, 1993.

J-7 K. Ramp, Memo Documenting GE/Harwell ECP Results for Brunswick HWC and Chinshan NWC, EPRI, September 1995.

J-8 Sun Ship Building & Dry Dock Company., "Brunswick Unit 1 Reactor Assembly", Drawing No. 730E854.

J-9 M. L. Herrera, S. Ranganath, "Evaluation and Screening Criteria for the Chinshan Units 1 & 2 Shrouds", Figure 2-2, GENE-523-13A-394, March 1994

J-10 Private conversation with R. M. Horn, GENE.

Table J-1

Core Shroud UT Inspection Results for Brunswick Unit 1 Refueling Outage 9 and 10

Content Deleted -
EPRI Proprietary Information

Table J-2

ECP Versus Feedwater H2 Concentration Curve Fit Equation Coefficients for H1 Shroud OD Weld and H5 Shroud ID Weld

Content Deleted -
EPRI Proprietary Information

Table J-3

Crack Extension Results for H1 and H5 Indications at BNP Unit 1

Content Deleted -
EPRI Proprietary Information

Content Deleted -
EPRI Proprietary Information

Figure J-1. GE/Harwell ECP Versus Feedwater H2 Concentration Predictions for H1 Shroud OD Weld and H5 Shroud ID Weld

Content Deleted -
EPRI Proprietary Information

Figure J-2. Stress Intensity for a 1.5" Thick Core Shroud Determined by Generic Residual Stress

Content Deleted -
EPRI Proprietary Information

Figure J-3. Estimated ECP Observed at H1 Shroud OD Weld Between RFO 9 and 10 with Estimated H1 Crack Extension Overlayed

Content Deleted -
EPRI Proprietary Information

Figure J-4. Conductivity Measured at Brunswick Unit 1 Between RFO 9 and 10 with Estimated H1 Crack Extension Overlayed

Content Deleted -
EPRI Proprietary Information

Figure J-5. Estimated Stress Intensity at H1 Shroud OD Weld Between RFO 9 and 10 with Estimated H1 Crack Extension Overlayed

Content Deleted -
EPRI Proprietary Information

Figure J-6. Estimated ECP Observed at H5 Shroud ID Weld Between RFO 9 and 10 with Estimated H5 Crack Extension Overlayed

Content Deleted -
EPRI Proprietary Information

Figure J-7. Conductivity Measured at Brunswick Unit 1 Between RFO 9 and 10 with Estimated H5 Crack Extension Overlayed

Content Deleted -
EPRI Proprietary Information

Figure J-8. Estimated Stress Intensity at H5 Shroud ID Weld Between RFO 9 and 10 with Estimated H5 Crack Extension Overlayed

Content Deleted -
EPRI Proprietary Information

Figure J-9. GE/Harwell Estimated of ECP for the Outer Core Bypass Region that is the Environment Associated with the Core Shroud ID

Content Deleted -
EPRI Proprietary Information

Figure J-10. GE/Harwell Estimated of ECP for the Downcomer Region that is the Environment Associated with the Core Shroud OD

Content Deleted -
EPRI Proprietary Information

Figure J-11. Stress Intensity for a 1.22" Thick Core Shroud Determined by Generic Residual Stress

Target:
Nuclear Power

About EPRI

EPRI creates science and technology solutions for the global energy and energy services industry. U.S. electric utilities established the Electric Power Research Institute in 1973 as a nonprofit research consortium for the benefit of utility members, their customers, and society. Now known simply as EPRI, the company provides a wide range of innovative products and services to more than 1000 energy-related organizations in 40 countries. EPRI's multidisciplinary team of scientists and engineers draws on a worldwide network of technical and business expertise to help solve today's toughest energy and environmental problems.

EPRI. Powering Progress

© 2000 Electric Power Research Institute (EPRI), Inc. All rights reserved. Electric Power Research Institute and EPRI are registered service marks of the Electric Power Research Institute, Inc. EPRI. POWERING PROGRESS is a service mark of the Electric Power Research Institute, Inc.

Printed on recycled paper in the United States of America

TR-105873NP

EPRI • 3412 Hillview Avenue, Palo Alto, California 94304 • PO Box 10412, Palo Alto, California 94303 • USA
800.313.3774 • 650.855.2121 • askepri@epri.com • www.epri.com